Karlsruhe Institute of Technology

Irradiation Studies at IBPT Accelerators

(Bestrahlungsstudien an IBPT-Beschleunigern)

Master's Thesis
of

Katharina Mayer

at the Department of Physics
Institute for Beam Physics and Technology (IBPT)

Reviewer:	Prof. Dr. Anke-Susanne Müller
Second Reviewer:	Prof. Dr. Joao Seco
Advisor:	Dr. Markus Schwarz
Second Advisor:	Dr. Alfredo Ferrari

July 2023

Erklärung zur Selbstständigkeit

Ich versichere, dass ich diese Arbeit selbstständig verfasst habe und keine anderen als die angegebenen Quellen und Hilfsmittel benutzt habe, die wörtlich oder inhaltlich übernommenen Stellen als solche kenntlich gemacht und die Satzung des KIT zur Sicherung guter wissenschaftlicher Praxis in der gültigen Fassung vom 30.09.2021 beachtet habe.

Karlsruhe, den 03.07.2023, _____

Katharina Mayer

Als Prüfungsexemplar genehmigt von

Karlsruhe, den 03.07.2023, _____

Prof. Dr. Anke-Susanne Müller

Contents

List of Figures

List of Tables

Abstract

An important oncological treatment method which more than half of all cancer patients receive is radiation therapy, in which the tumor is irradiated with ionizing radiation. This kind of therapy offers the advantage of a localized tumor treatment in contrast to chemotherapy which affects the whole system. In recent years, the study of short intense radiation pulses (FLASH effect) or spatially fractionated radiation (MicroBeam/MiniBeam) has become an important research field, as these methods show reduced damage to healthy tissue in addition to the same tumor control. Systematic studies of this type often require non-medical accelerators that are capable of generating the desired short intense pulses and, in general, possess a large and flexible parameter space for investigating a wide variety of irradiation methods. At KIT (Karlsruhe Institute of Technology), the accelerators of IBPT (Institute for Beam Physics and Technology) give access to complementary high-energy and time-resolved radiation sources. While the linear electron accelerator FLUTE (Ferninfrarot Linac- und Testexperiment) can generate ultrashort electron bunches, the electron storage ring KARA (Karlsruhe Research Accelerator) provides a source of pulsed X-rays.
Within the scope of this thesis, first proof-of-principle experiments of dose characterizations at FLUTE and KARA have been conducted, laying the foundation for further experiments of this type and more advanced experiments in the field of radiation therapy. This included the use and testing of an ionization chamber at FLUTE for absolute dose measurements. Moreover, radiochromic films were tested and used in dose measurements at KARA. For this purpose, the implementation and testing of a measurement and evaluation procedure for the quantitative determination of the obtained film dose took place. The dosimetry experiments were complemented by Monte Carlo simulations performed with the simulation program FLUKA (FLUktuierende KAskade). Here, an additional consideration of different exit windows with attention to dose optimization at FLUTE was performed and preparations for future window pressure tests were made. Similarly, biological compatibility tests were performed with H460 lung cancer cells in combination with hydrogels as an artificial extracellular matrix with respect to vertical sample assembly during irradiation at the accelerators. Furthermore, a 3D cell formation of that cell line was tested as well. These preparatory experiments lay the foundation for future research on radiation therapy at FLUTE and KARA.

Kurzfassung

Eine wichtige onkologische Behandlungsmethode, die mehr als die Hälfte aller Krebspatienten erhält, ist die Strahlentherapie, bei welcher eine Bestrahlung des Tumors mit ionisierender Strahlung stattfindet. Diese Art der Therapie bietet den Vorteil einer lokalen Tumorbehandlung im Gegensatz zur Chemotherapie, die sich auf den gesamten Körper auswirkt. In den letzten Jahren ist die Untersuchung kurzer intensiver Strahlungspulse (FLASH-Effekt) oder räumlich fraktionierter Strahlung (MicroBeam/MiniBeam) zu einem wichtigen Forschungsgebiet geworden, da diese Methoden neben der gleichen Tumorkontrolle eine geringere Schädigung des gesunden Gewebes aufweisen. Für systematische Studien dieser Art werden häufig nicht-medizinische Beschleuniger benötigt, die in der Lage sind, die gewünschten kurzen und intensiven Pulse zu erzeugen, und die im Allgemeinen einen großen und flexiblen Parameterraum für die Untersuchung verschiedenster Bestrahlungsmethoden bieten. Am KIT (Karlsruher Institut für Technologie) stehen mit den Beschleunigern des IBPTs (Institute for Beam Physics and Technology) komplementäre hochenergetische und zeitaufgelöste Strahlungsquellen zur Verfügung. Während der lineare Elektronenbeschleuniger FLUTE (Ferninfrarot Linac- und Testexperiment) ultrakurze Elektronenpakete erzeugen kann, stellt der Elektronenspeicherring KARA (Karlsruhe Research Accelerator) eine Quelle für gepulste Röntgenstrahlung dar.
Im Rahmen dieser Arbeit wurden erste Proof-of-Principle-Experimente zur Dosischarakterisierung an FLUTE und KARA durchgeführt, die den Grundstein für weitere Experimente dieser Art und weitergehende Experimente im Bereich der Strahlentherapie legen. Dazu gehörte der Einsatz und die Erprobung einer Ionisationskammer an FLUTE für absolute Dosismessungen. Darüber hinaus wurden an KARA radiochrome Filme getestet und für Dosismessungen eingesetzt. Hierzu erfolgte die Implementierung und Erprobung eines Mess- und Auswerteverfahrens zur quantitativen Bestimmung der erhaltenen Filmdosis.
Ergänzt wurden die Dosimetrieexperimente durch Monte-Carlo-Simulationen, die mit dem Simulationsprogramm FLUKA (FLUktuierende KAskade) durchgeführt wurden. Hier wurde eine zusätzliche Betrachtung verschiedener Austrittsfenster mit Blick auf die Dosisoptimierung bei FLUTE durchgeführt und Vorbereitungen für zukünftige Fensterdrucktests getroffen. Ebenso wurden biologische Kompatibilitätstests mit H460-Lungenkrebszellen in Kombination mit Hydrogelen als künstliche extrazelluläre Matrix im Hinblick auf die vertikale Probenanordnung während der Bestrahlung an den Beschleunigern durchgeführt. Des Weiteren wurde die 3D-Zellbildung jener Zelllinie erprobt. Diese vorbereitenden Experimente legen den Grundstein für zukünftige Forschung zur Strahlentherapie an FLUTE und KARA.

1. Introduction

Radiation therapy, also known as radiotherapy, is one of the central pillars of cancer treatment along with chemotherapy and surgery. It is used both as a standalone and as a complementary treatment method, which more than half of all cancer patients receive [1]. Radiotherapy encompasses a large area in which research is being conducted into increasingly efficient radiation methods that are spatially more precise and should be less damaging to healthy tissue.
Cancer has accompanied humanity for a long time and will become more and more present in the following years. According to prognoses and current trends, there will be an increase of nearly 13 % of all new cancer cases every five years [2, 3]. This is due to the increasing life expectancy of the population on the one hand and the increasing environmental pollution on the other, which significantly increases the risk of developing cancer [3, 4, 5]. For example, trachea, bronchus and lung cancer deaths have risen from 1.2 million to 1.8 million from 2000 to 2019, a 50 % increase, making it the sixth leading cause of death worldwide [6]. For this reason, numerous efforts are being made to constantly improve and further develop existing treatment methods, including radiotherapy.

The so-called FLASH effect was first reported by Dewey and Boag in 1959. In comparison to conventional radiotherapy, FLASH radiotherapy (FLASH-RT) is a quite novel radiotherapy technology, in which very high doses are required within a very short time (dose rate greater than 40 Gy/s) [7]. Because of this, there is an increasing interest in research accelerators in addition to conventional methods for radiotherapy research such as X-ray tubes, delivering homogeneous photon irradiation or proton therapy using particle accelerators [1]. Research accelerators usually have the advantage of a very large and flexible parameter range which can be variably operated. In general, due to their short pulsed radiation, they have a particularly high peak dose rate in the order of 10^{12} Gy [8]. Thus, they offer the possibility of systematic studies such as the FLASH effect or even new irradiation methods with regard to their efficiency and compatibility.
Another quite new form of radiotherapy which also qualifies for systematic studies is a spatially irradiation in stripes, a so-called MicroBeam/MiniBeam irradiation [9].

Precise and easy-to-use detectors for the characterization of the radiation sources are needed to enable systematic radiotherapy studies. But at the same time, the high-energy and pulsed radiation of research accelerators, in contrast to the homogeneous lower-energy radiation of medical accelerators, is also increasingly pushing the field of dosimetry to its limits.
In general, the conventional detectors for dose measurements are not designed for high-energy and pulsed radiation sources, so no established dosimetry methods are available. In addition to the air-filled ionization chambers used as standard in medical physics, radiochromic films [10] for spatial radiation dose detection and semiconductor detectors are increasingly coming to the fore, depending on the application, radiation source and further research in the dose measurement of pulsed, high-energy sources [11, 12].

One example of such a research accelerator is the linear short-pulse electron accelerator FLUTE (Ferninfrarot Linac- und Test-Experiment), which serves as an accelerator test facility [13] to generate and study ultra-short and intense THz-radiation. Another example is the electron synchrotron storage ring KARA (Karlsruhe Research Accelerator), which is used as an accelerator test facility and synchrotron light source in various fields of physics, materials science and biological sciences [14].

FLUTE offers the possibility to perform irradiation studies with *pulsed electron beams* instead of photon beams. At the same time, various beam parameters such as beam energy, bunch charge, bunch length, pulse rate and beam shape can be variably adjusted. This would enable systematic irradiation studies of samples with electrons. FLUTE is currently undergoing a major upgrade, after which it will initially continue to operate in the low-energy range with an electron energy of up to 7 MeV. After the upgrade, bunch charges of up to 1 nC with a repetition rate of 10 Hz are foreseen. When using the LINAC and the bunch compressor in a later phase of the project, final energies of about 90 MeV can eventually be achieved and the electron bunch length after the bunch compressor can be reduced to the femtosecond range. This opens additional doors for possible irradiation methods [15].

In the case of KARA, there is the possibility to perform irradiation experiments with *pulsed photon beams* in the X-ray range. The synchrotron radiation is generated by the deflected electrons with an energy of 0.5 GeV to 2.5 GeV in the storage ring by dipole magnets of the storage ring or so-called insertion devices (undulators, wigglers). The spectrum available for experiments in the beamline is strongly related to the setup of the special beamline. In general, synchrotron radiation is characterized by its high brilliance and a spectrum from infrared to hard X-rays. In order to perform first irradiation experiments and with the idea of later cell experiments, the IMAGE beamline, one of 23 beamlines, is chosen due to its high achievable photon energy and cell compatible space conditions. IMAGE is connected to a CLIC wiggler which generates strong synchrotron radiation. Using a monochromator, the generation of a maximum 40 keV photon beam is achievable and corresponds to the highest photon energy at KARA [14, 16].

The accelerators of the Institute for Beam Physics and Technology (IBPT), FLUTE and KARA offer a unique opportunity to study for example the previous mentioned radiotherapeutic effects and the possible biological impact of high peak dose rates due to the short pulsed radiation. Both machines are well suited for these studies because both electrons and X-rays can be used in one place.

In radiotherapy, the ionizing radiation must reach a tumor with a certain dose and often inside healthy tissue. To simulate this surrounding healthy tissue consisting mostly of water, so-called phantoms are usually used in medical physics. These phantoms are mostly made of plastics with water-like properties. For a later successful performance of irradiation experiments with cells, characterizations of both accelerators regarding their potential dose distributions are necessary. To properly design and optimize the experiments, corresponding dose simulations in addition to experimental measurements of the dose distributions are performed. This is done by means of the simulation program FLUKA (FLUktuierende KAskade) [17, 18, 19]. FLUKA, a multipurpose multi-particle code based on the Monte Carlo method, has its origins in the 1960s and has been continuously optimized over the decades according to its intended use. Today, it is a powerful simulation program to compute particle transport and interaction with matter. The application range of FLUKA extends from calculations for accelerator shielding to calculations in neutrino physics and to dosimetric and medical physics calculations. In the context of this work, simulations serve to estimate the doses of FLUTE and KARA as well as a validation of the experiments carried out there.

For later cell irradiation experiments with cancer cells, a suitable setup is required. In general, cells are cultured in aqueous solutions and therefore can only be irradiated vertically. One part of the thesis focuses on how to prepare for irradiation experiments at IBPT accelerators. The challenge with these research machines is the horizontal beam guidance, which is why cell samples have to be irradiated while mounted vertically. To solve this, cells can be prepared in so-called hydrogels, which allow a temporary vertical mounting of the cells for the horizontal irradiation. Hydrogels are hydrophilic polymeric materials with a high water content and good mechanical stability. Their original use is to serve as bioinks for 3D printing and to act as artificial extracellular matrix (ECM). Due to their gel-like consistency and biocompatibility, they can serve as a suitable nutrient medium substitute for cells during irradiation [20]. At the same time, it would be possible to grow 3D cell structures, for example so-called spheroids, and place them in the gels for irradiation experiments. In this way, possible spatial effects of the cell arrangement on the success of the irradiation can be studied.

Overall, it can be said that the field of radiotherapy is an interdisciplinary research area of increasing importance in relation to the increasing number of new cancer cases. The success and development of new promising radiotherapeutic treatment methods in cancer therapy thus depends to a large extent on the cooperation of and exchange between various scientific fields. The present work provides first proof-of-principle experiments and is a first step towards establishing medical radiotherapy at IBPT. It is carried out in cooperation with the institutes of KIT, IBPT and IFG (Institut für Funktionelle Grenzflächen) as well as the group E041 (Biomedical Physics in Radiation Oncology) of the DKFZ (Deutsches Krebsforschungszentrum). While IBPT provides the physical knowledge and access to accelerators, the latter two provide the biological know-how and resources.

This thesis is structured into five sections. After the introduction of the physical and medical-physical basics in Chapter 2, the used simulation program FLUKA is introduced in Chapter 3. Moreover, first simple test simulations and estimations regarding the expected dose based on the later experiments are discussed.
In Chapter 4 and Chapter 5, the two accelerators of IBPT are shortly presented. While Chapter 4 deals with FLUTE and the depth dose curve measurement performed there, Chapter 5 presents first Gafchromic film dose measurements at the beamlines LIGA I and IMAGE at KARA. In addition, simulations comparable to the experiments are analyzed and discussed for both accelerators.
Chapter 6 concludes by presenting various biological methods such as the use of hydrogels to facilitate horizontal irradiation and an attempt to generate human lung cancer cell (H460) spheroids.
Finally, a short summary and an outlook on planned and possible future experiments in the field of radiotherapy is given.

2. Theoretical Background

This chapter provides an overview of relevant physical and biological basics related to this thesis. First of all, the interaction of ionizing particles with matter is considered. Moreover, this chapter gives a brief insight into the related dosimetry and current cancer treatment methods as well as research in the field of radiation therapy.

2.1. Particle Interaction with Matter

When particles like photons, electrons, protons and ions penetrate matter, usually different interactions take place between them and the target material. These interaction mechanisms will lead to an energy loss $\mathrm{d}E$, scattering of the initial particles and to an increase in the material temperature. These interactions can have different effects depending on the particle and matter properties [21].
In the following, a distinction is made between charged (directly ionizing radiation) and neutral particles (indirectly ionizing radiation) with focus on the particle types relevant for this thesis: electrons and photons [22].

2.1.1. Charged Particles - Electrons

In the case of charged particle such as electrons, protons and ions, one can distinguish between four principal types of interaction mechanisms [22]:

- inelastic collisions with atomic electrons, which lead to excitation or ionization of an atom,
- inelastic collision with a nucleus which enables the generation of bremsstrahlung due to Coulomb interaction of the charged particle and the nucleus,
- elastic scattering with a nucleus,
- elastic collision with atomic electrons.

In addition, the phenomenon known as Cherenkov radiation occurs when charged particles pass through a medium at a speed greater than the phase velocity of light in that medium. This effect is mentioned here to include all relevant aspects but will not be further discussed.

The largest contribution to the specific energy loss $^{\mathrm{d}E}/_{\mathrm{d}x}$ per differential path length, which relates to the number of generated ions per cm path length, is made by inelastic collisions, ionization and bremsstrahlung.
How large the respective contributions are and if other interactions make a significant contribution depends strongly on the ionizing particle type and the initial particle energy E_{ini} as well as on the absorber material, absorber type and density ρ [23].
The relativistic energy E of a particle is given by

$$E^2 = (mc^2)^2 + (cp)^2, \tag{2.1}$$

where m corresponds to the particle rest mass, c is the speed of light and p the particle momentum. It can also be expressed by the sum of the rest energy E_0 and the kinetic energy E_{kin}, i.e.

$$E = E_0 + E_{\mathrm{kin}} \tag{2.2}$$

and is often expressed in the unit eV instead of J whereby $1\,\mathrm{eV} \approx 1.6 \cdot 10^{-19}\,\mathrm{J}$.

The specific energy loss is also known as the linear stopping power $S = -\mathrm{d}E/\mathrm{d}x$. To get the total stopping power, the stopping powers of all interaction mechanisms have to be added [22], where the usual unit MeV/cm is used. Here, only the two main responsible contributions, which were mentioned before, are taken into account, namely the stopping power for inelastic collisions S_{col} and the radiative stopping power S_{rad}:

$$S_{\mathrm{tot}} = S_{\mathrm{col}} + S_{\mathrm{rad}} = -\frac{\mathrm{d}E}{\mathrm{d}x}. \tag{2.3}$$

An expression for the stopping power that is often found in the literature is the mass stopping power S_{mass}, which is defined as

$$S_{\mathrm{mass}} = \frac{1}{\rho} \cdot S = -\frac{1}{\rho} \cdot \frac{\mathrm{d}E}{\mathrm{d}x}. \tag{2.4}$$

The mass stopping power with the dimension $(\mathrm{MeV\,cm^2})/\mathrm{g}$ depends only slightly on the density ρ of the absorber material in the case of the collision stopping power.
If the stopping power is known for the material of interest, the corresponding energy loss ΔE of a particle over a distance Δx through the material can be calculated according to

$$\Delta E = \int_{x_{\mathrm{start}}}^{x_{\mathrm{end}}} S\,\mathrm{d}x \sim S \cdot \Delta x. \tag{2.5}$$

This energy is absorbed by the target material. Correspondingly, the average range of a particle in matter Δx can be determined by the integration of the reciprocal stopping power over energy according to

$$\Delta x = \int_0^{E_{\mathrm{ini}}} \frac{1}{S(E)}\,\mathrm{d}E. \tag{2.6}$$

Bethe, Bloch et al. first performed a correct quantum-mechanical calculation to determine the stopping power of heavy charged particles (protons, ions, etc.). In the case of heavy particles, there is hardly any deflection in relation to their trajectory, which is why energy losses through radiation are negligible. The final equation is commonly known as the Bethe-Bloch formula and is the basic expression used for energy loss calculations [24]

$$-\frac{\mathrm{d}E}{\mathrm{d}x} = \frac{1}{2} K \rho z^2 \frac{Z}{A} \frac{1}{\beta^2} \left[\ln \frac{2 m_{\mathrm{e}} c^2 \beta^2 \gamma^2 \cdot W_{\mathrm{max}}}{I^2} - 2\beta^2 \right] \tag{2.7}$$

with the coefficient

$$K = \frac{N_{\mathrm{A}} \cdot e^4}{4\pi\epsilon_0^2 m_{\mathrm{e}} c^2}. \tag{2.8}$$

Avogadro's number is denoted by N_{A}, m_{e} corresponds to the electron mass, e to the elementary charge, ϵ_0 stands for the vacuum permittivity and $\gamma = \sqrt{1-\beta^2}^{-1}$ is the relativistic Lorentz factor.
It should be noted that in practice, small corrections are necessary for an exact description. Usually, the density effect correction δ and the shell correction C are added to Equation (2.7).

Equation (2.7) shows that there is an impact on the stopping power by the material density ρ, the mean excitation potential I, the atomic number Z and the atomic mass A, while the charge number of the incident particles with speed ratio $\beta = v/c$ is represented by z.

The mean excitation potential I is an important parameter in the Bethe-Bloch equation, but it is generally very difficult to calculate for many materials. Values for I of various materials can be approximated using semi-empirically derived formulas, for example, through

$$\frac{I}{Z} = \begin{cases} \left(12 + \frac{7}{Z}\right) \text{ eV}, & Z < 13 \\ \left(9.76 + 58.8 \cdot Z^{-1.19}\right) \text{ eV}, & Z \geq 13. \end{cases} \tag{2.9}$$

The maximal possible energy transfer to a shell electron in a single collision $W_{\max}$ is given by

$$W_{\max} = \frac{2m_{\mathrm{e}}c^2\beta^2\gamma^2}{1 + \frac{2\gamma m_{\mathrm{e}}}{M} + \left(\frac{m_{\mathrm{e}}}{M}\right)^2}. \tag{2.10}$$

Here, M denotes the incident particle mass. The Bethe equation (Equation (2.7)) is valid for relativistic particles in the region $0.1 < \beta\gamma < 1000$ [25].

In the case of lighter particles like electrons, which are significantly lighter than protons ($m_{\mathrm{p}}/m_{\mathrm{e}} \approx 2000$), we have to take into account the angular deflection in case of collisions with the atom and that the collisions occur between identical particles as well as the energy loss due to bremsstrahlung. Losses due to bremsstrahlung could be neglected for low energies, but become the dominant process for rising particle energy. The energy at which the energy loss due to bremsstrahlung equals the energy loss due to ionization is usually referred to as the critical energy E_{c}. Radiation losses become dominant for energies $E > E_{\mathrm{c}} = 610\,\mathrm{MeV}/(Z + 1.24)$ in case of solids and for $E > E_{\mathrm{c}} = 710\,\mathrm{MeV}/(Z + 0.92)$ in case of gases using Rossi's definition for the electron critical energy. The critical energy after Rossi is defined as the energy at which the ionization loss per radiation length X_0 is equal to the electron energy. The radiation length defines the mean distance over which a high-energy electron loses all but $1/e$ of its energy due to bremsstrahlung. In the case of light elements critical energies result from $E_{\mathrm{c}} > 100\,\mathrm{MeV}$ [25]. The total stopping power of electrons will be the sum of collision losses S_{col} and radiation losses S_{rad}.
A graphical representation of both stopping power progressions is shown in Figure 2.1. The energy transfer to atomic electrons due to collision losses is described by the Møller cross section [25]. With the above adjustments for the calculation of the collision stopping power, the Bethe-Bloch formula for electrons is given by

$$\left(-\frac{\mathrm{d}E}{\mathrm{d}x}\right)_{\mathrm{col}} = \frac{K\rho}{2}\frac{Z}{A}\frac{1}{\beta^2}\cdot\left[\ln\frac{m_{\mathrm{e}}c^2\beta^2\gamma^2\cdot W_{\max}}{I^2} + (1-\beta^2) - \frac{2\gamma-1}{\gamma^2}\cdot\ln 2 + \frac{1}{8}\left(\frac{\gamma-1}{\gamma}\right)^2\right], \tag{2.11}$$

where the maximum energy transfer via Equation (2.10) results in

$$W_{\max} = \frac{1}{2}m_{\mathrm{e}}c^2(\gamma - 1). \tag{2.12}$$

The factor $1/2$ is needed as mentioned above because the colliding particles are indistinguishable. Furthermore, the linear specific energy loss through the emission of bremsstrahlung because of the deflection of the electron with the elementary charge e in the electric field of the nucleus can be approximated as

$$\left(-\frac{\mathrm{d}E}{\mathrm{d}x}\right)_{\mathrm{rad}} = \rho\frac{N_{\mathrm{A}}}{M}\frac{1}{(4\pi\epsilon_0)^2}\frac{E}{137m_{\mathrm{e}}^2c^4}\cdot Z(Z+1)\cdot e^4\cdot\left(4\ln\frac{2E}{m_{\mathrm{e}}c^2} - \frac{4}{3}\right). \tag{2.13}$$

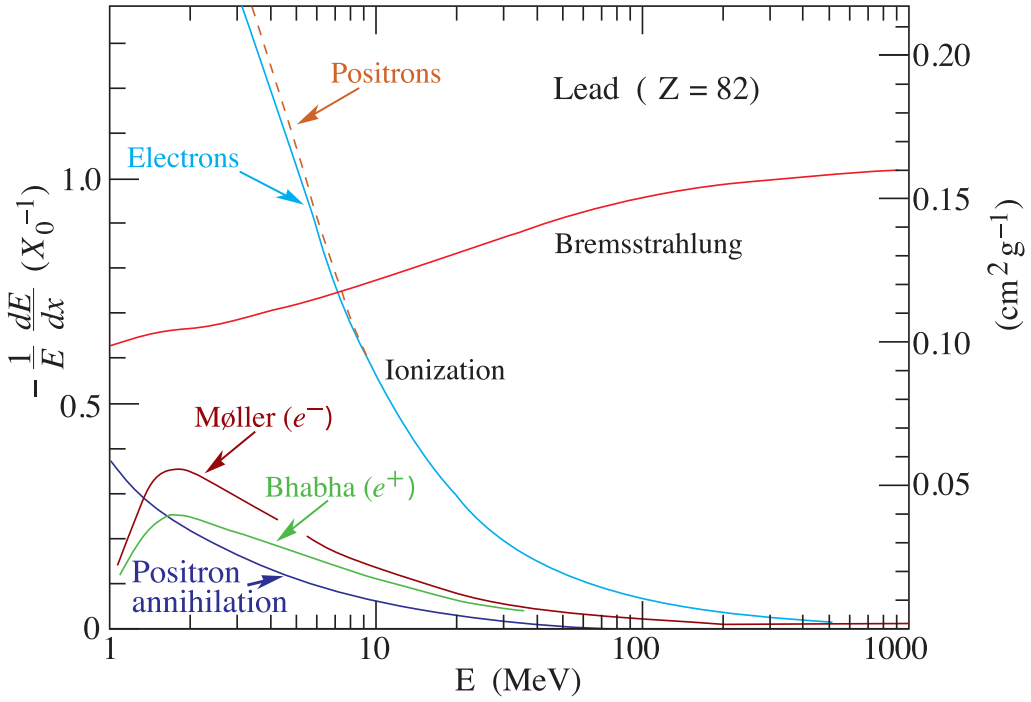

Figure 2.1.: Ionization and radiation energy losses per radiation length X_0 in lead ($Z = 82$) as a function of electron or positron energy with $X_0(\mathrm{Pb}) = 6.37\,\mathrm{g/cm^2}$ [25].

Here M denotes the molar mass of the absorber material. The energy loss due to radiation can also be approximately expressed by the ratio of both stopping powers via

$$\left(-\frac{\mathrm{d}E}{\mathrm{d}x}\right)_{\mathrm{rad}} = \frac{E \cdot Z}{700} \cdot \left(\frac{\mathrm{d}E}{\mathrm{d}x}\right)_{\mathrm{col}}, \tag{2.14}$$

where E is in unit of MeV. For typical particle energies less than a few MeV, radiative losses are just a small fraction in comparison to the energy losses due to ionization and excitation. Radiative losses become significant in absorber materials of high atomic number or for high incident electron energies [26].

A more detailed consideration can be found in [25], [22] or [24].

2.1.2. Neutral Particles - Photons

In the case of photons, the major interaction mechanisms are

- the photoelectric effect,
- Compton scattering and
- pair production.

Some less common interactions will be neglected in this discussion [24]. Within all interactions, the absorber material is ionized and the generated secondary electrons deposit their energy through the interaction processes mentioned in Section 2.1.1. The penetration depth of photons in matter is much further than that of charged particles and a photon beam is attenuated in intensity, but is not degraded in energy while penetrating the absorber material, with the exception of the energy degrading Compton effect. For this reason, the attenuation of a photon beam $I(x)$ can be described using the Beer–Lambert law

$$I(x) = I_0 \cdot e^{-\mu x}, \tag{2.15}$$

where I_0 is the incident beam intensity, x is the penetration depth and μ denotes the total absorption coefficient, which is related to the total interaction cross-section σ_{tot} [24] according to

$$\mu = \rho \frac{N_{\text{A}}}{A} \cdot \sigma_{\text{tot}} = \rho \cdot \frac{N_{\text{A}}}{A} \cdot (\sigma_{\text{ph}} + Z\sigma_{\text{c}} + \sigma_{\text{pair}}). \tag{2.16}$$

It should be noted that Beer-Lambert law is only valid for narrow photon beams that are well collimated [22].

Photoelectric Effect

For photons in the energy range $E_{\text{b}} < E = h \cdot \nu < 100\,\text{keV}$, the photoelectric effect will be the dominating interaction process. Here E_{b} is the binding energy of the atomic electron measured in eV and ν is the frequency of the incident photon. Penetrating photons will be absorbed completely by the atomic electrons of the material in case of a collision and a so-called photo electron with kinetic energy $E_{\text{kin}} = h\nu - E_{\text{b}}$ is generated. Accordingly, secondary electrons are generated via the photoelectric effect, which then depose their energy subsequently in the material.
The photoelectric cross section can be described approximately by

$$\sigma_{\text{ph}} \sim \begin{cases} \sigma_0 \cdot Z^5 \cdot \left(\frac{m_{\text{e}}c^2}{E}\right)^{7/2}, & E > E_{\text{b}} \\ \frac{Z^5}{E}, & E \gg E_{\text{b}}. \end{cases} \tag{2.17}$$

Figure 2.2 shows the photon total cross sections as a function of the photon energy. It can be seen that the photoelectric cross section is characterized by discontinuities. These discontinuities correspond to the absorption edges that occur, which are characterized by reaching the thresholds for photoionization of the various atomic levels.

Compton Effect

At higher photon energies in the range $E_{\text{b}} \ll E$, the inelastic scattering known as the Compton effect becomes important. The cross section for Compton scattering can be calculated using the Klein-Nishina formula [24], which results in

$$\sigma_{\text{c}} \sim \frac{Z}{E}. \tag{2.18}$$

A part of the photon energy is transferred to a shell electron so that the atom can be excited or even ionized. The incoming photon is not absorbed and is therefore red-shifted since it gives up part of its energy.

Pair Production

For high energies, i.e. for energies higher than two times the electron rest energy ($E > 2 \cdot E_{0,\text{e}} \approx 1.022\,\text{MeV}$), pair production can occur. The pair production cross section scales approximately with the formula

$$\sigma_{\text{pair}} \sim \begin{cases} Z^2 \ln E, & E > 2 \cdot E_{0,\,\text{e}} \\ Z^2, & E \gg 2 \cdot E_{0,\,\text{e}}. \end{cases} \tag{2.19}$$

In this new absorption canal, a photon transforms within the Coulomb field of the nucleus into an electron (e^-) and positron (e^+) pair. The cross section depends on the atomic number Z of the target material and on the initial photon energy E. The energy dependence of the cross sections is shown graphically in Figure 2.2. A closer look to the different photon cross sections [23] and interaction mechanisms can be found in [22], [23], [24] and [11].

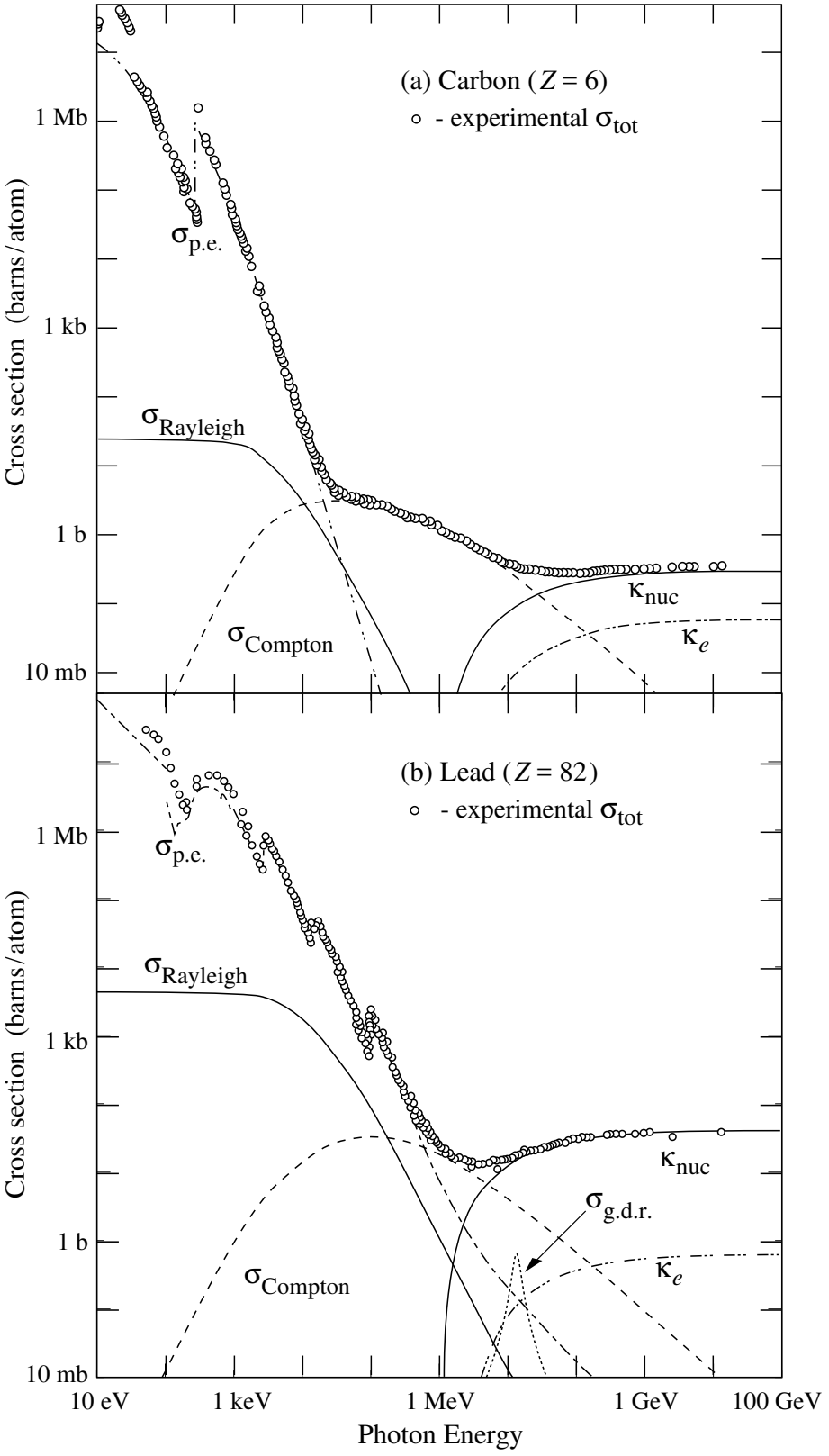

Figure 2.2.: Photon total cross sections as a function of energy in carbon ($Z = 6$) and lead ($Z = 82$). The contributions of different interaction processes are shown here: $\sigma_{\mathrm{p.e.}}$ = atomic photoelectric effect (electron ejection, photon absorption), $\sigma_{\mathrm{Rayleigh}}$ = Rayleigh (coherent) scattering–atom neither ionized nor excited, $\sigma_{\mathrm{Compton}}$ = incoherent scattering (Compton scattering off an electron), κ_{nuc} = pair production, nuclear field, κ_{e} = pair production, electron field, $\sigma_{\mathrm{g.d.r.}}$ = photonuclear interactions, target nucleus is usually broken up [25].

2.2. Dosimetry

When ionizing particles penetrate matter, they will experience a loss of energy due to the mentioned interaction processes and this will have an influence on the absorbing material. This is often used in radiation therapy and radiation protection alike. Therefore, a procedure to quantify the effects of the ionizing particles is needed. The field of dosimetry generally deals with this task. Dosimetry is the measurement and evaluation of radiation doses, i.e. the amount of energy that is transferred to an absorbing material by ionizing particles. Different measurement methods and quantities are used to record and quantify the radiation dose. A distinction between fundamental dosimetry methods in which the dose is measured due to its definition and relative methods in which the dose is calculated out of measured data and calibration factors has to be made.
Important areas of application are the clinical dosimetry as part of radiotherapy and radiation protection [12]. In the following, some basic definitions of the physical dose definitions and some detectors for dose measurements used in the thesis will be discussed. It should be noted that all the following dose definitions refer to expectation values and mean values.

2.2.1. Dose Concept

The quantification of the effect of ionizing particles is expressed in several different units, which are either a measure of the amount of energy deposition $\mathrm{d}E$ or the amount of ionization, i.e. the generation of secondary charged particles $\mathrm{d}Q$ in a material with unit mass $\mathrm{d}m$ [24].

A relevant physical quantity for the discussion of irradiation effects on matter and within the scope of this thesis is the absorbed dose D since it is proportional to the biological effects [12]. It is defined as the total absorbed energy $\mathrm{d}E$ per mass element $\mathrm{d}m$ of the absorbing material with density ρ and volume $\mathrm{d}V$, namely

$$D = \frac{\mathrm{d}E}{\mathrm{d}m} = \frac{\mathrm{d}E}{\rho \cdot \mathrm{d}V}. \tag{2.20}$$

The SI-unit of the absorbed dose is Gray and is defined as the absorption of the energy of 1 J per 1 kg of matter, i.e.

$$[D] = 1\,\mathrm{Gy} = 1\,\frac{\mathrm{J}}{\mathrm{kg}}. \tag{2.21}$$

Due to the fact that the energy transfer to matter is generated by the interactions of the electrons, regardless of whether they are primary or secondary electrons, the absorbed dose can be calculated using the relation

$$D = \int_0^{E_{\max}} \frac{S_{\mathrm{col}}(E)}{\rho}\,\Phi_{\mathrm{E}}\,\mathrm{d}E \tag{2.22}$$

in which $\Phi_{\mathrm{E}}\,\mathrm{d}E$ stands for the electron fluence in the energy interval E to $E + \mathrm{d}E$. Fluence $\Phi = {}^{\mathrm{d}N}/_{\mathrm{d}A_\perp}$ in general means the particle number $\mathrm{d}N$ per area perpendicular to the particle movement $\mathrm{d}A_\perp$ [11].

Since the absorbed dose cannot be measured directly, the ion dose J must be measured. The ion dose is a quantity for the amount of charges generated with equal sign $\mathrm{d}Q$ as a sequence of ionization per mass $\mathrm{d}m$ [23], accordingly

$$J = \frac{\mathrm{d}Q}{\mathrm{d}m}. \tag{2.23}$$

The SI-unit of the ion dose is given by

$$[J] = 1\,\frac{\mathrm{C}}{\mathrm{kg}}. \tag{2.24}$$

Absorbed dose and ion dose are connected via the proportional relationship

$$D = k \cdot J, \tag{2.25}$$

whereby k is a material specific correction factor. The correction factor in case of water is $k = 35\,\mathrm{Gy/C/kg}$, for biological tissue a bit higher with $k = 37\,\mathrm{Gy/C/kg}$ and for air, we have $k = 33.97\,\mathrm{Gy/C/kg}$ [27]. The factor k describes the ability of the material to absorb the energy of ionizing particles [23]. In other words, it describes the average energy required to generate an ion pair. If the irradiated detection volume is air, the ion dose is often called standard ion dose.

The term "kerma" (kinetic energy released per unit mass) is relevant in the case of indirectly ionizing radiation such as photons. Kerma refers to the transferred energy from indirectly ionizing radiation into kinetic energy $\mathrm{d}E_{\mathrm{kin}}$ of secondary particles, generally electrons which release their energy subsequently to the irradiated object with the mass $\mathrm{d}m$, therefore it holds:

$$K = \frac{\mathrm{d}E_{\mathrm{kin}}}{\mathrm{d}m}. \tag{2.26}$$

As well as for the other dose quantities, the unit is Gray

$$[K] = 1\,\mathrm{Gy}. \tag{2.27}$$

An important parameter in determining kerma is the energy-transfer coefficient μ_{tr}, through which the kerma can be calculated similar to Equation (2.22) by using the photon fluence $\Phi_{\mathrm{E}}\,\mathrm{d}E$ in the energy interval E to $E + \mathrm{d}E$ and can be calculated by

$$K = \int_0^{E_{\max}} \frac{\mu_{\mathrm{tr}}(E)}{\rho} \cdot E \cdot \Phi_{\mathrm{E}}\,\mathrm{d}E. \tag{2.28}$$

For low-energy photons, the kerma is essentially equivalent to the absorbed dose as there is a secondary electron equilibrium. However, for very high-energy photons, it is possible that the transferred kinetic energy is very high and that the secondary particles may escape the medium resulting in the kerma overestimating the absorbed dose [28, 11].

Another important and often used quantity in radiotherapy is the dose rate

$$\dot{D} = \frac{\mathrm{d}D}{\mathrm{d}t}, \tag{2.29}$$

which describes the time evolution of the dose. The unit of the dose rate in general is

$$\left[\dot{D}\right] = 1\,\frac{\mathrm{Gy}}{\mathrm{s}}. \tag{2.30}$$

Further commonly used dose quantities are the equivalent dose, which takes into account the biological effectiveness of the absorbed dose, and the effective dose, which considers the tissue sensitivity to different types of radiation.
To differentiate between the absorbed dose and the equivalent dose, the unit of the equivalent dose is given in Sievert (Sv), where one Sievert, in SI units, is equivalent to one Joule per kilogram and has therefore the same unit as the absorbed dose. A more detailed explanation can be looked up in the DIN (Deutsches Institut für Normung) standards for dosimetry, cf. DIN 6814-3 or 6800-2, [11], [29] and [21].

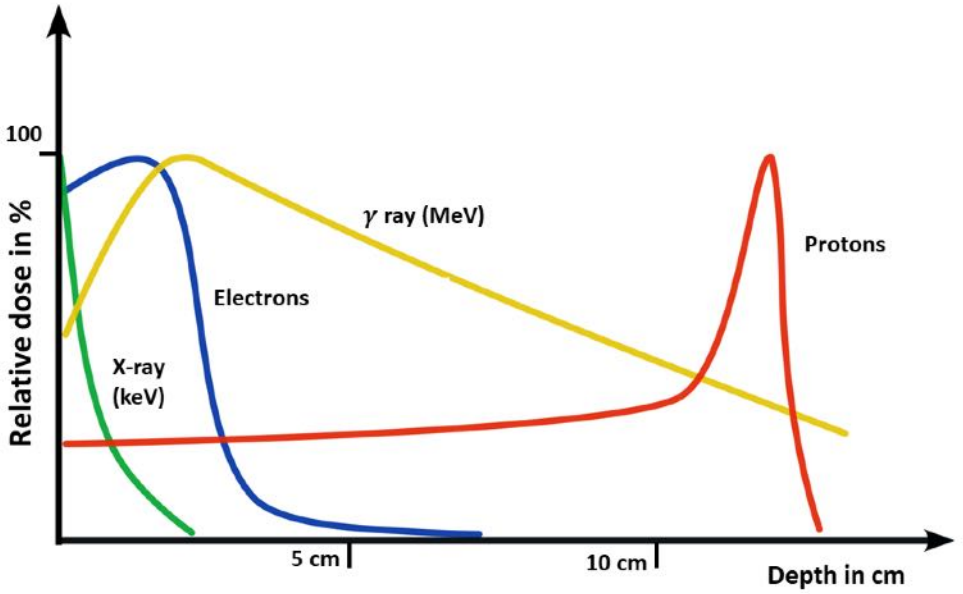

Figure 2.3.: Relative depth dose curves of typical ionizing particles, protons (red) with characteristic Bragg peak, electrons (blue), X-rays (green) and gamma radiation (yellow). Redrawn illustration based on [27].

Depth Dose Curves

Dose distributions are the spatial distribution of the absorbed dose in the absorbing material and play a major role in the radiation planning of patients in radiotherapy. In addition to the physical properties of the absorber, the particle type and energy also have an influence on the generated dose distribution. In most cases, a one-dimensional graphical representation, that of a dose curve along a line, is chosen to illustrate a dose distribution or a so-called dose profile. A special dose profile is the depth dose distribution, a distribution which reflects the dose distribution on a straight line in the radiation field axis within the irradiated body. The associated graphical representation is known as the depth dose curve [29, 12]. Typical depth dose curves of common ionizing particles are shown in Figure 2.3. The curves show different progressions of the relative absorbed dose on the ordinate with progressive penetration depth on the abscissa that is usually measured in cm for the respective kind of ionizing particles and initial energy. Maximal dose values are reached at different penetration depths due to diverse interaction mechanisms which dominate depending on the particle type and energy range, see Section 2.1.

The depth dose curve of protons (red) shows the characteristic progression with a slowly rising dose and a sharp high dose maximum at the end, the so-called Bragg Peak. The same characteristic exists for ions. For X-rays (green) in the range of keV, the dose maximum is right on the surface and then a exponential decay according to Equation (2.15) follows. In the case of high energetic photons (gamma radiation) in the range of MeV (yellow) and electrons (blue) the dose maximum occurs not directly on the surface, but below and is deeper the higher the initial energy of the particles is. This phenomenon can be explained by the build-up effect.

The build-up effect can be explained by the fact that secondary electrons are generated by the primary electrons or photons via various interaction mechanisms and scatter in the medium. They will release their energy to the medium until all energy has been released and the electrons have arrived at the end of their path. At that point, the electron fluence will decrease and the dose will decrease as well.

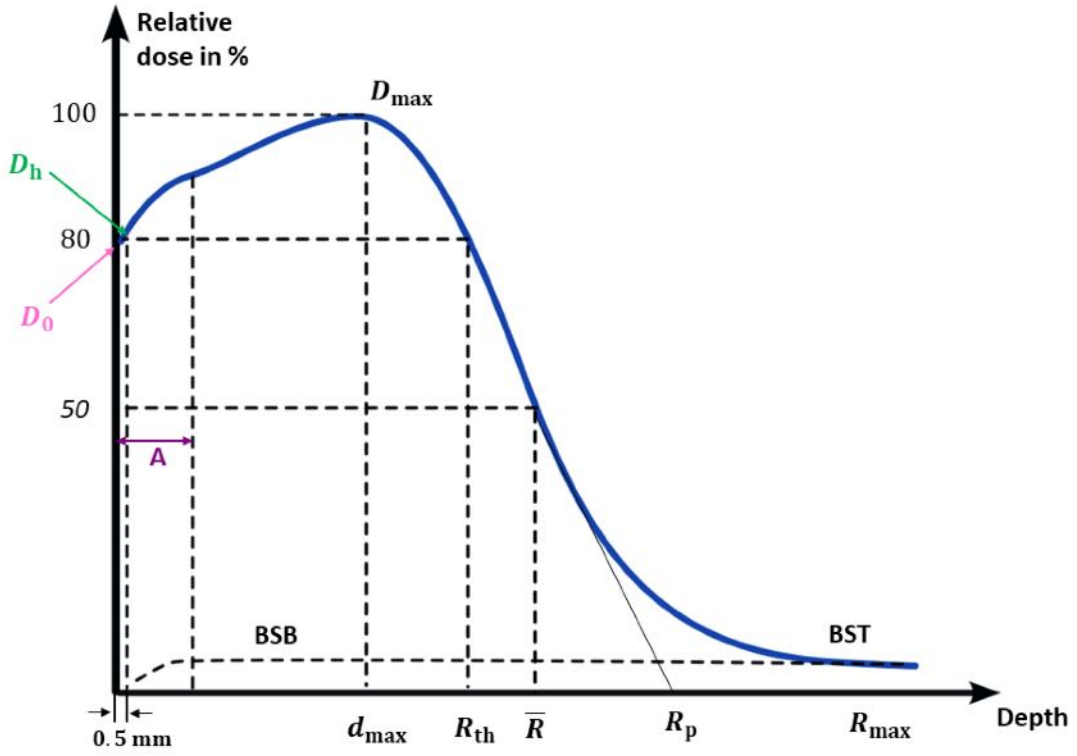

Figure 2.4.: Relative electron depth dose curve, relative dose over depth, with characteristic ranges and doses for description. $\overline{R}$: mean range, R_p: practical range, R_{max}: maximal range, R_{th}: therapeutic range, d_{max}: maximal dose depth, D_0: surface dose, D_h: skin dose, D_{max}: maximal dose, A: build-up zone, BSB: BremsStrahlung Background, BST: BremsStrahlung Tail. Redrawn illustration based on [12].

For photons, electrons are released in proportion to the number of them. This explains why the number of released electrons decreases with penetration depth and as a result, the absorbed dose falls. The dose drop is not that steep as for primary electrons, due to the weaker interaction of photons with matter and new, but less, electrons with equal initial energies are continuously generated. The depth of the maximum of photons corresponds to the reach of the generated electrons and with rising photon energy, it lies deeper because of the more energetic generated secondary electrons.
In the case of electrons, the dose maximum can be explained by the scattering and fanning out of primary and secondary electrons. If the electrons reach a state with complete diffusion, the maximal energy transfer follows. Approximately, electrons have a continuous energy loss, but due to the projection on the central movement axis, the energy transfer density rises on the central axis until the mentioned complete diffusion. Additionally, the stopping power, so the energy loss, will rise with lower electron energies which also increases an increase in dose. After that, the dose decreases rapidly because less and less electrons are left and because of the finite range of electrons in matter. Figure 2.4 illustrates some general terms for the characterisation of electron depth dose curves. This includes different ranges like the depth of the dose maximum d_{max} and the therapeutic range R_{th} where 80 % to 85 % of the maximal dose is reached. The mean range $\overline{R}$, also known as half depth, is the depth where the dose dropped about 50 %. The practical range R_p is defined as the intersection of the x-axis and the tangent at the half-value dose point and the maximal range R_{max} where the curve fits the underground of the bremsstrahlung.

Some of the ranges (in cm) can be estimated using different rules of thumb

$$\overline{R}\,[\mathrm{cm}] = \frac{E_0\,[\mathrm{MeV}]}{2.33}, \tag{2.31}$$

$$R_\mathrm{p}\,[\mathrm{cm}] = \frac{E_0\,[\mathrm{MeV}]}{2}, \tag{2.32}$$

$$R_\mathrm{th}\,[\mathrm{cm}] = \frac{E_0\,[\mathrm{MeV}]}{3}. \tag{2.33}$$

Similarly, the average electron entry energy can be determined by graphically determining the mean range $\overline{R}$ in cm and using

$$E_0\left(\overline{R}\right) = 2.33\,\frac{\mathrm{MeV}}{\mathrm{cm}} \cdot \overline{R} + 7 \cdot 10^{-5}\,\frac{\mathrm{MeV}}{\mathrm{cm}^4} \cdot \overline{R}^4. \tag{2.34}$$

Due to the particle-dependent profiles of the dose curves and the dose maxima reached at different depths, it is obvious that different ionizing particles with different energies are used depending on the application [29, 12, 27].

2.2.2. Detectors

To determine the dose and the dose distributions as well as the resulting dose curves such as the depth dose curve, suitable detectors are required. Common dose measurement methods and the detectors used for them, also known as dosimeters, are described in this section. There are many different methods available today for the measurement of dose including both physical and chemical methods. In case of radiology and radiation therapy, commonly used detector types are gas detectors and film dosimeters, but also semiconductors and other kinds of detectors can be used. Here, a focus is placed on the first two detector types. For a more detailed insight see [11] and [12], [29].

2.2.2.1. Ionization Chamber

Ionization chambers are gas detectors based on the principle of charge separation and collection of the produced electrons and ions by passing ionizing particles using electrical fields in gas-filled detectors with the sensitive volume $\mathrm{d}V$.
A general setup of an ionization chamber is shown in Figure 2.5. Different forms are used for different application fields as well as different gas compositions and applied voltages for charge collection. For very high electrode voltages, the primary charge generated by ionizing particles will lead to a gas discharge. This kind of gas detectors are known as Geiger-Müller counter tubes and are normally used for radiation protection. In the case of ionization chambers, the electrode voltage is chosen high enough so that all generated ions are collected, but low enough so that there will be no charge multiplication due to gas amplification. Under these conditions, the collected charge is proportional to the averaged dose deposited in the gas, the size of the sensitive measure volume and the gas density. For this reason, the collected charges are usually measured and displayed directly in electrical units using an electrometer, for example in nanocoulombs (nC). The sensitivity of ionization chambers depends primarily on the measuring volume and the type and pressure of the filling gas. Dosimetry with air filled ionization chambers is the most important method of dose measurement in radiology and radiation therapy. Common types are cylindrical chambers or flat chambers (see Figure 2.6). To obtain the absorbed dose D in Gray from the measured value M of the ionization chamber, a calibration factor N is needed so that

$$D = N \cdot M. \tag{2.35}$$

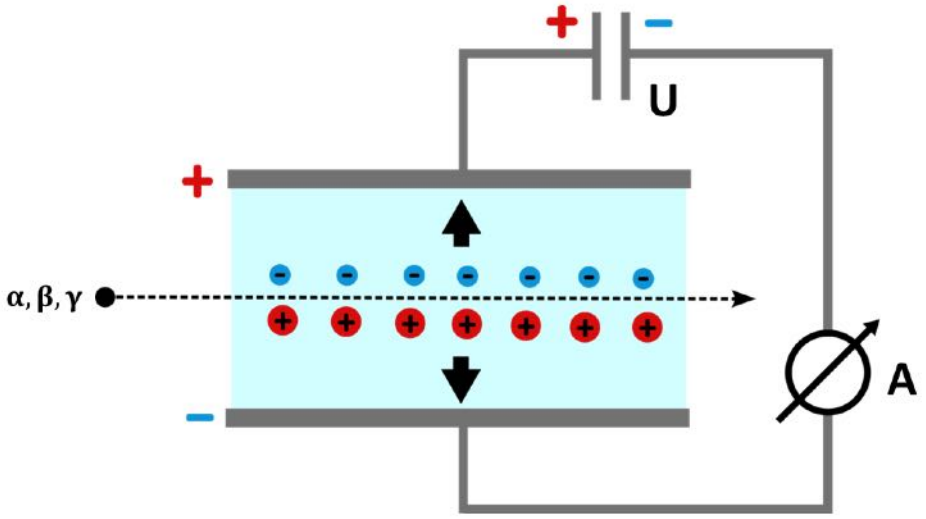

Figure 2.5.: Schematic setup of an ionization chamber. Ionizing radiation generates positive and negative charges in the detector volume. Due to the electrical field present, these diffuse to the metal electrodes of opposite polarity, which are connected to DC voltage. The resulting ionization current is detected using a charge measuring device (A). Redrawn illustration based on [12].

In general, N is determined via a ^{60}Co-γ-emitter (in Germany) in a water phantom under defined calibration conditions [11] that include temperature ($T_0 = 293.15\,\mathrm{K}$), pressure ($p_0 = 101.325\,\mathrm{kPa}$), distance detector to source, chamber voltage, surrounding material etc. For real measurements, there are normally no standard conditions like in the calibration case and the dose generating particles are not from a ^{60}Co-γ-emitter. Because of this, some correction factors must be taken into account that turn Equation (2.35) into

$$D = \prod_{\mathrm{i}=1}^{\mathrm{m}} k_{\mathrm{i}} \cdot N \cdot (M - M_0)\,, \tag{2.36}$$

where M_0 is the measured value of the dosimeter without radiation, k_i (i =T, p, s, etc.) are the different correction factors, for example k_{T} for temperature, air density k_ρ or recombination losses k_{s}. The correction k_ρ results for example from

$$k_\rho = \frac{T}{T_0} \cdot \frac{p_0}{p}. \tag{2.37}$$

2.2.2.2. Film Dosimeter

Film dosimetry is used as a dosimetry method in radiation therapy since the 1960s [29]. Films have a very high spatial resolution but in general a relative high dose measurement uncertainty [29].
Radiographic and radiochromic films have a special importance [11]. Irradiation of both film types leads to a color change of the films. In the first case a irradiation leads to a blackening because of the reduction of silver bromide compounds to free silver and in the second case to a bluing because of a polymerisation process. A typical structure of radiochromic films from Gafchromic$^{\mathrm{TM}}$ is shown in Figure 2.7. These films consist of an active layer ($\approx 25\,\mu\mathrm{m}$), consisting of an active component, a marker dye, stabilizers and other components, which is sandwiched between two matte-polyester substrates ($\approx 125\,\mu\mathrm{m}$) [10]. The color change

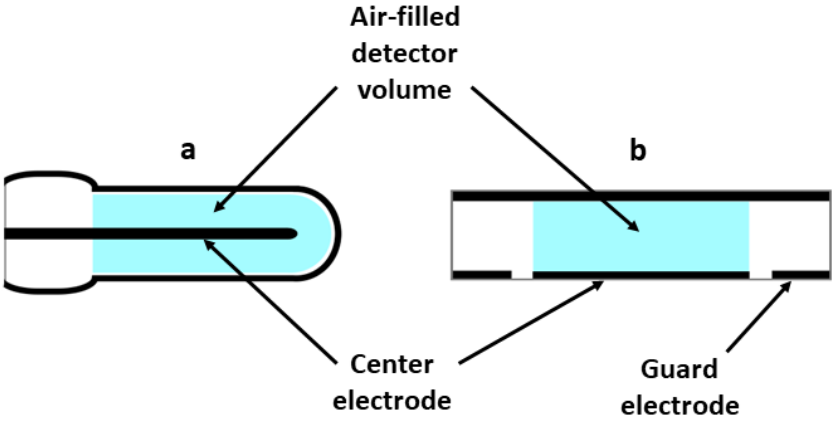

Figure 2.6.: Schematic representation of the two most important construction types of ionization chambers: **a** cylindrical chamber, **b** flat chamber. The light blue volume represents the air filled detection volume, the sensitive volume. Redrawn illustration based on [11].

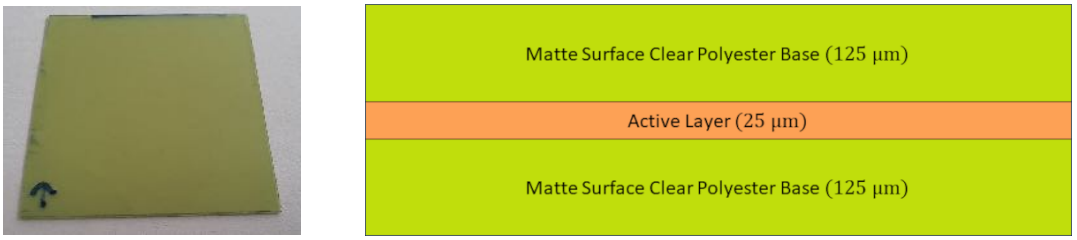

Figure 2.7.: EBT-XD film top view (left) and side view of the schematic film structure of GAFChromic EBT-XD dosimetry film (right) with the active layer sandwiched between two matte-polyester substrates. The active layer contains the active component, a marker dye, stabilizers and other components and has it best performance in the dose range from 0.4 Gy to 40 Gy. Redrawn illustration based on [10].

of the films can be determined quantitatively via the optical density OD which depends on the initial light intensity I_0 and the transmitted light intensity I according to

$$OD = \log_{10}\left(\frac{I_0}{I}\right). \tag{2.38}$$

It is a common method to show the optical density as a function of the absorbed dose in a so-called optical density curve. Therefore, a calibration measurement with defined dose values for every film type and batch has to be done because the films sensitivity may vary between film types and batches [29, 12].

2.3. Cancer and Treatment

Cancer in general refers to a malignant formation of new tissue, a tumor or a so-called neoplasia or malignancy. Cancer cells grow uncontrollably and could destroy healthy tissue, in most cases they form daughter ulcers, so-called metastases which can spread through the bloodstream or the lymphatic system to other organs. [5]. It takes several steps for cancer to develop, the reasons are usually not trivial to identify. Possible risk factors are for example smoking, alcohol, pathogens, exposure to chemicals, UV radiation and other ionizing radiation, but in many cases cancer arises spontaneously during cell division in

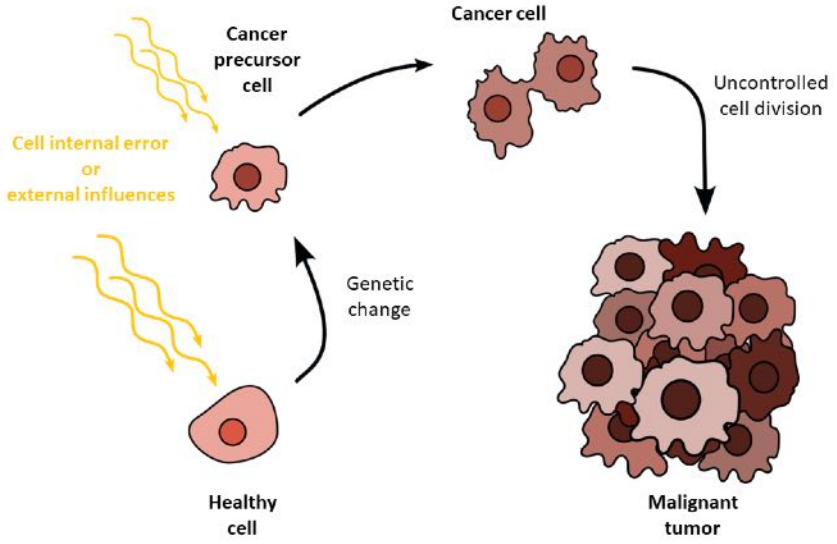

Figure 2.8.: Schematic development of cancer out of healthy tissue in several steps. Internal or external influences (yellow arrows) that contribute to the development of cancer include hereditary factors, coincidence, but also various environmental factors, the personal lifestyle or pathogens. Redrawn illustration based on [4].

which errors can occur and, therefore, it is also referred to as a disease of the genes [5, 4]. A simplified graphical representation of cancer development can be seen in Figure 2.8. Without proper treatment methods, cancer will lead to death in most of the cases. Therefore, there is a multitude of treatment methods that are constantly being improved and further researched in order to discover new and more effective methods. The most common cancer treatment methods are a surgical removal of the tumor, chemotherapy or radiation therapy, but in many cases, the treatment is a combination of these three methods, but are used individually as well. Radiation therapy will be described in more detail below as the central point of application of this thesis.

2.3.1. Radiotherapy

Radiotherapy or radiation therapy is an often used method in cancer treatment. More than every second patient receives radiation therapy, which, in contrast to chemotherapy, enables local treatment of cancer. In the case of radiotherapy, the cancer cells are destroyed basically via ionizing radiation [1, 3].

As explained in the previous sections, ionizing particles will deposit energy in the matter they penetrate. This will in general lead to the ionization of the object and, in the case of living cells, could lead to a damage of them. Exactly this mechanism is used by radiation therapy to prevent tumor cells from growing or even destroy them completely.
On the one hand, cells can be damaged directly through ionizing particles by breaking the chemical bound of molecules, especially DNA (DeoxyriboNucleic Acid) by damaging the double helix structure, or indirectly through the generation of chemical radicals from water molecules in the cells which will attack the molecules chemically [3], see Figure 2.9. If the cell's repair mechanisms are not sufficient because the damage caused is too great, cells die. This is often the case for cancer cells since the repair mechanisms only work to a limited extent. Because of this, malignant tumors are often very sensitive to ionizing radiation which leads to the desired reduction in size of the tumor or even to a complete destruction [31].

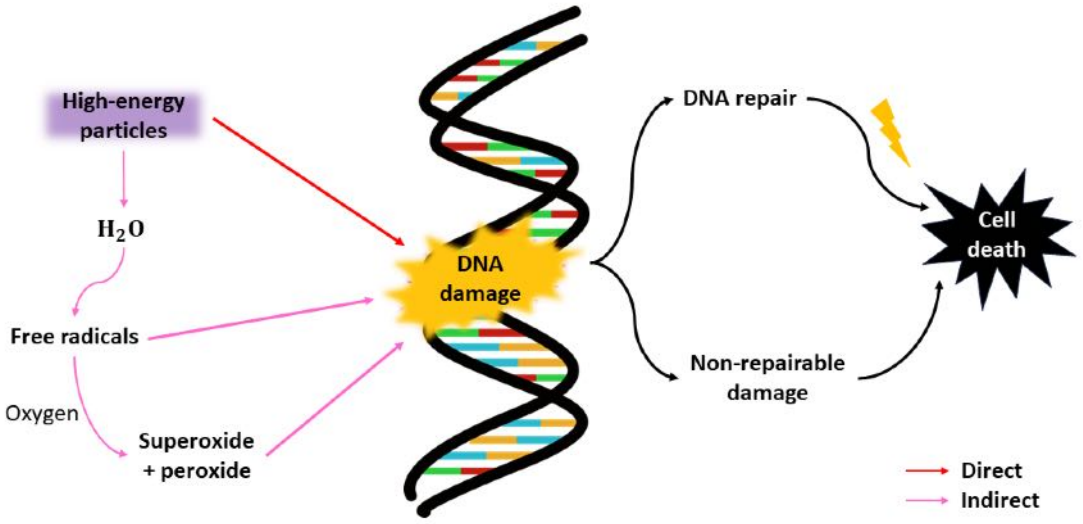

Figure 2.9.: Radiation damage to DNA. High-energy particles can affect the cell DNA either by direct pathway (red) or indirect pathway (pink). In the latter case, DNA is damaged by free radicals and harmful by-products generated through the process of water radiolysis, which increase oxidative stress in the cell. Cell survival depends on the damage inflicted and the effectiveness of repair mechanisms. Redrawn illustration based on [30].

Of course, not just cancer cells will be affected by the ionizing radiation, as desired, but healthy cells as well. If the damage of the ionizing radiation is too high and the healthy cell's own repair mechanisms are not enough, they can suffer a permanent damage in DNA and this can lead to observable biological effects. One possible response to the damage could be the mentioned cell death of course, another effect could be a permanent alteration of the cell which does not lead to their death or illness but maybe to a genetic effect that affects even later generations. Other effects could also be that the irradiation of healthy cells is leading to impairments of the cell functionality that could cause different somatic effects such as sterility or also cancer [24].

In radiotherapy, the radiation dose is chosen by the doctor due to the sensitivity of the tumor. In case of a conventional treatment, a homogeneous irradiation with total doses ranging from 40 Gy to 70 Gy divided into fractions of 1.8 Gy to 2 Gy over a period of weeks is chosen. In comparison to that, the annual radiation exposure in Germany just amounts to 2.1 mSv/year on average [31].
Depending on the type and position of the tumor, different particle types and particle energies can be used for a good tumor control and protection of healthy tissue. In the case of tumors close to the skin, irradiation with photons or electrons is an option because of their dose maximum near the surface while protons or heavy ions are suitable for deeper tumors taking advantage of the Bragg Peak (see Figure 2.3).

Cancer diseases will continue to increase in the years to come, which is partly due to the overall increase in life expectancy and increasing environmental pollution [2, 4]. Because of this, active research is carried out into even more effective treatment methods that enable both good tumor control and protection of healthy tissue. Instead of using conventional radiation, the current focus of research is to investigate unconventional irradiation methods like the effects of extremely high doses (FLASH effect) in a short time or the influence of special radiation patterns (MicroBeam/MiniBeam).

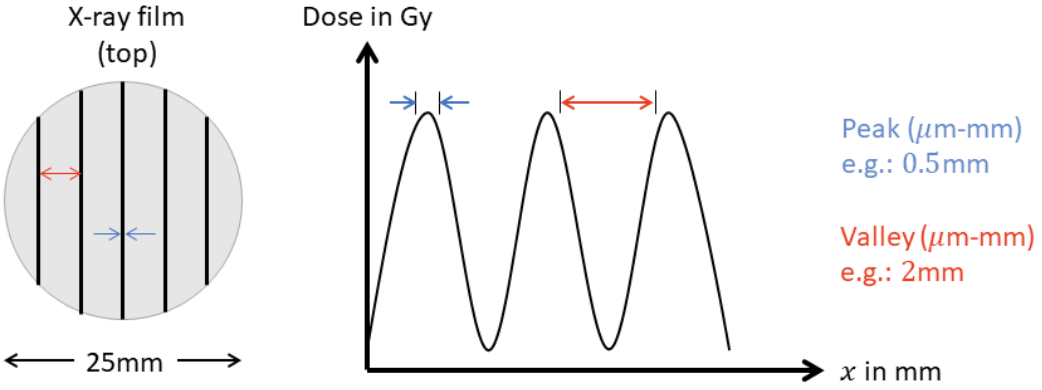

Figure 2.10.: Schematic representation of a MicroBeam/MiniBeam film dosimeter irradiation with characteristic irradiation pattern (left) and an exemplary spatial dose plot with recognizable peak and valley dose (right).

FLASH Effect

One unconventional promising radiation therapy method is the ultra-high dose radiotherapy, abbreviated as FLASH. As the name would suggest, this type of radiation therapy delivers a very high dose in a short amount of time $\dot{D} > 40\,\mathrm{Gy/s}$ in contrast to conventional fractionated radiotherapy. The extremely high and short dose pulses in FLASH radiotherapy also pose a challenge to previous dosimetry and beam control. It is suspected that FLASH leads to fewer late side effects in healthy tissue while preserving tumor control in comparison to conventional dose rate irradiation. The biological effects, which are still largely unexplained, and the influence of oxygen on the FLASH effect according to the treatment success are part of the current state of research in radiotherapy [7, 32].

MicroBeam/MiniBeam

Another promising irradiation method is the so-called MicroBeam or MiniBeam method. This method does not use homogeneous irradiation over a large area, but irradiation in the form of strips, see Figure 2.10. The irradiation area therefore consists of strips with a high dose, called the peak dose, and the areas in between with a very low dose, called valley dose. Depending on the width of the strips, the irradiation method is referred to as MicroBeam (width $\approx$ µm) or MiniBeam (width $\approx$ mm). As with FLASH therapy, it is assumed that tumor control can be achieved just as well while damage to healthy tissue is reduced at the same time. Film dosimeters (see Section 2.2.2.2) are often used here for dosimetry since they can be used to verify the spatial dose profile very precisely [9].

3. Simulation Software: FLUKA

FLUKA (FLUktuierende KAskade), based on the Monte Carlo method, is a simulation program which has been developed in the 1960s by Johannes Ranft. The first FLUKA code was used to evaluate the performances of sodium iodide (NaI) crystals used as hadron calorimeters. Over time, the program has been improved and revised by many scientists. It was restructured, so that the code evolved in a multi-purpose and multi-particle code applicable to a wide range of subjects and energies. The modern FLUKA has been developed starting from 1989 by A. Fassò, A. Ferrari, J. Ranft and R.R. Sala.
Today it can be used for calculations of particle transport and interactions with matter for a variety of applications like proton and electron accelerator shielding, dosimetry, detector design, neutrino physics, medical physics or radiotherapy. With the help of today's FLUKA code, the interaction and propagation of about 60 different particle types in matter can be simulated, like for example electrons, photons, neutrinos, muons, antiparticles, neutrons and heavy ions. The simulation covers a wide range of particle energies, for example electrons and photons can be simulated in an energy interval from 100 keV up to a thousand TeV and hadrons up to energies of 20 TeV. Very complex geometries can be handled with FLUKA via an an improved version of the Combinatorial Geometry (CG) package that is predominantly necessary in medical physics and radiotherapy. With this package, it is also possible to track charged particles correctly in magnetic or electric fields if necessary.

A variety of physical models were implemented for a precise simulation of particle interactions. Some of the most important particle matter interactions in the context of this thesis are the interaction mechanisms of electrons and photons which have already been introduced in Chapter 2. These interaction mechanisms and many others, some of which are less dominant, are implemented with FLUKA to enable a precise description of the physical processes. This includes, in the case of electrons, the stopping power, an original transport algorithm for charged particles that includes a complete multiple Coulomb scattering treatment. In addition, differences between electrons and positrons are taken into account, bremsstrahlung differential cross sections of Seltzer and Berger and Delta-ray production via Bhabha and Møller scattering are considered. To simulate the photon interaction with matter, the most important interactions mechanisms like the Compton effect, photoelectric effect, pair production, Rayleigh scattering and photon polarisation are implemented in FLUKA as well.

A more detailed overview can be found in the FLUKA manual and a more precise description of the physical models can be found in several journal and conference papers which are referenced in the FLUKA manual [17] or [18].

3.1. Monte Carlo Method

The Monte Carlo method (MCM) is a class of computational algorithms that uses (pseudo-)random numbers and their repeated random sampling for the numerical solution of various physical and mathematical problems that are analytical difficult or impossible to solve.

The MCM has its origins in probability theory [33]. A first reference to MCM was by Comte de Buffon in 1777. He proposed a method similar to the MCM to determine the probability of a needle tossed randomly onto a ruled sheet, whether the needle with length L lied across a line with distance $d > L$. Modern MCM, as well as the name "Monte Carlo", arose in connection with the development of the first nuclear weapons. The scientists Neumann and Ulam drove the development of MCM and its implementation initially analogue and later digital on computers.

Today, with the use of digital computers, the MCM is used in many fields like social science, mathematics, physics and chemistry. Classic applications can be found in finances, traffic flow calculations, radiotherapy and radiation dosimetry. It can be used to simulate random processes with many coupled degrees of freedom (fluids, strongly coupled solids, cellular structures, particle matter interaction) and thus to predict the behavior of certain systems and variables.

The foundation of the MCM is the law of large numbers. The latter states that the sample mean of the random experiment results X_i repeated in the same way converges to the theoretical expected value $\overline{X}$ with increasing repetition number N, i.e.

$$\lim_{N\to\infty} \sum_{i=1}^{N} \frac{X_i}{N} = \overline{X} \tag{3.1}$$

According to the central limit theorem, the mean $\overline{X}$ or in general the result of a Monte Carlo integration is a Gaussian random quantity and follows therefore a Gaussian distribution. The uncertainty of the mean $\sigma(\overline{X})$ in that case is given through the standard deviation of $\overline{X}$ and measures the accuracy of the computed $\overline{X}$ with a certain confidence level. The uncertainty of the mean decreases with increasing sampling size N and satisfies

$$\sigma(\overline{X}) \sim \frac{1}{\sqrt{N}}. \tag{3.2}$$

In order to obtain reliable results, a correspondingly large but finite sample size N must be chosen. Based on a Monte Carlo simulation of the interactions of ionizing particles with matter, this means that a corresponding number of primary particles, also known as primaries, must be simulated, to reach a certain confidence level. This correlates strongly with the required calculation time via the law time $\sim 1/\text{error}^2$ [33].

The trajectory of a particle when passing through matter is random and is determined by the microscopic particle-matter interactions. The probability distributions of the interactions are given by the cross sections of the respective interaction process. In a Monte Carlo simulation for particle-matter interactions, random numbers are applied to determine the random trajectories by taking the probability distributions into account. This is done for each single primary particle which can result in many particles of higher order like secondary electrons forming a so called "history" or "shower". With a sufficiently large number of primary particles N, the average macroscopic distribution of quantities such as the dose can be determined [34, 33, 28].

3.2. FLAIR - A FLUKA Graphical User Interface

In many cases, FLUKA is used in combination with FLAIR (FLUKA Advanced Interface), a graphical user interface for easier handling and editing of FLUKA input files, debugging, execution and the subsequent visualization of the output files containing the simulation results. In addition, the FLAIR geometry editor is used for the geometry visualization, which uses 2D cross-sections of the geometry, for interactive error correction and editing. FLAIR also includes a material database of nuclides and their known isotopic compositions. In a reference database, approximately 300 predefined materials can be found and used for simulations [35, 17].

3.3. Validation through Simple Dose Simulations

To get familiar with the FLUKA program code and to validate the settings for the subsequent simulations, simplified dose rate simulations for the case of an electron beam and a photon beam are presented below and compared to analytical estimations.

The corresponding mass stopping powers for electrons in water $S_{\mathrm{H_2O}}(E_{\mathrm{kin}})$, the mass attenuation coefficients $\mu_{\mathrm{H_2O}}(E)$ and the mass energy absorption coefficients of photons in water $\mu_{\mathrm{en,\,H_2O}}(E)$ were taken from the NIST (National Institute of Standards and Technology) Standard Reference Databases 124 [36] and 126 [37]. For simplicity, the properties of the pulsed beam, such as the bunch length, are not examined in detail. Only the time averages for both the electron and photon beams are considered.

3.3.1. Electron Beam - Absorbed Dose

For the absorbed dose estimation in water, a volume of size $\mathrm{d}V = 0.5\,\mathrm{mm}^3$ ($1\,\mathrm{mm} \times 1\,\mathrm{mm} \times 0.5\,\mathrm{mm}$) is struck by an electron beam. For a pulsed electron beam with kinetic energy of $E_{\mathrm{kin}} = 4.5\,\mathrm{MeV}$, a bunch charge $Q_0 = 100\,\mathrm{pC}$ and a repetition rate $f_0 = 10\,\mathrm{Hz}$ are chosen.

To estimate the absorbed dose, the dose generated by a single electron $D_{1\mathrm{e}}$ is first determined and then scaled to the dose of one bunch $D_{100\,\mathrm{pC}}$ for the final calculation of the average dose rate $\dot{D}_{\mathrm{e,\,est}}$. This means, that a single electron with energy $E_{\mathrm{kin}} = 4.5\,\mathrm{MeV}$ which penetrated a water target of $x_{\mathrm{H_2O}} = 500\,\mu\mathrm{m}$ thickness and density $\rho_{\mathrm{H_2O}} = 1\,\mathrm{g/cm}^3$ will approximately lose an energy of

$$\begin{aligned}
\Delta E &= S_{\mathrm{H_2O}}(E = 4.5\,\mathrm{MeV}) \cdot x_{\mathrm{H_2O}} && (3.3)\\
&= S_{\mathrm{mass,\,H_2O}}(E = 4.5\,\mathrm{MeV}) \cdot \rho_{\mathrm{H_2O}} \cdot x_{\mathrm{H_2O}} && (3.4)\\
&= 1.951\,\frac{\mathrm{MeV\,cm^2}}{\mathrm{g}} \cdot 1\,\frac{\mathrm{g}}{\mathrm{cm^3}} \cdot 0.05\,\mathrm{cm} && (3.5)\\
&\approx 0.097\,\mathrm{MeV}, && (3.6)
\end{aligned}$$

according to Equation (2.5). The deposited dose in the water target with volume $\mathrm{d}V$ that corresponds to a mass of $\mathrm{d}m = \rho_{\mathrm{H_2O}} \cdot \mathrm{d}V = 5 \cdot 10^{-4}\,\mathrm{g}$ can be calculated using Equation (2.20):

$$D_{1\mathrm{e}} = \frac{\mathrm{d}E}{\mathrm{d}m} = \frac{0.097 \cdot 10^6 \cdot 1.6 \cdot 10^{-19}}{5 \cdot 10^{-7}}\,\frac{\mathrm{J}}{\mathrm{kg}} = 3.1 \cdot 10^{-8}\,\mathrm{Gy} \tag{3.7}$$

For an electron beam with bunch charge Q_0, which corresponds to approximately $N_{\mathrm{e}} = 6.2 \cdot 10^8$ electrons, and repetition rate f_0, this results in a dose of

$$D_{100\,\mathrm{pC}} = D_{1\mathrm{e}} \cdot N_{\mathrm{e}} \approx 19.344\,\mathrm{Gy}, \tag{3.8}$$

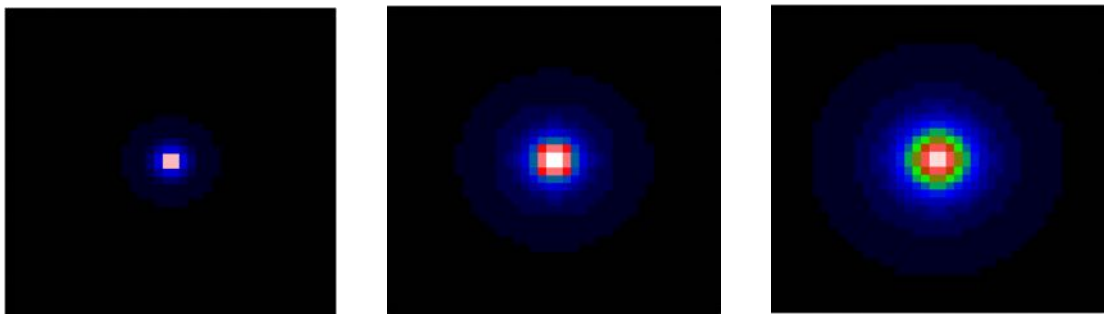

(a) Point beam **(b)** Rectangular beam **(c)** Gaussian beam

Figure 3.1.: Beam profiles of the FLUKA simulations, plotted with FLAIR. Projection onto the x-y plane. Figure dimension: 1 cm × 1 cm.

which yields a dose rate of

$$\dot{D}_{\mathrm{e,\ est}} = D_{100\,\mathrm{pC}} \cdot f_0 = 193.44\,\frac{\mathrm{Gy}}{\mathrm{s}}. \tag{3.9}$$

To validate the simulation settings, the analytically estimated dose rates are compared to the dose rates simulated with FLUKA for three different beam types:

- **Point-like beam (PB)**: point like shape, mono-energetic beam with $E_{\mathrm{kin}} = 4.5\,\mathrm{MeV}$ (Figure 3.1a),
- **Rectangular beam (RB)**: rectangular shape, spatial expansion $\mathrm{d}x = \mathrm{d}y = 0.1\,\mathrm{cm}$, mono-energetic beam with $E_{\mathrm{kin}} = 4.5\,\mathrm{MeV}$ (Figure 3.1b),
- **Gaussian beam (GB)**: Gaussian shape, spatial sigmas $\sigma_{\mathrm{x}} = \sigma_{\mathrm{y}} = 0.05\,\mathrm{cm}$ (FWHM $= 0.1177\,\mathrm{cm}$), mono-energetic beam with $E_{\mathrm{kin}} = 4.5\,\mathrm{MeV}$ (Figure 3.1c).

The beams hit a water target of dimension $V_0 = 4\,\mathrm{cm} \times 4\,\mathrm{cm} \times 4\,\mathrm{cm}$ to take possible backscatter effects into account.

Likewise, three slightly different setups are analyzed

- **Setup 1**: The electron beam hits the water target directly (Figure 3.2a),
- **Setup 2**: The electron beam hits the water target after passing 1 cm of air (Figure 3.2b).
- **Setup 3**: The electron beam hits the water target after passing 1 cm vacuum and a 500 µm thick aluminium window (Figure 3.2c).
- **Setup 4**: The electron beam hits the water target after passing 1 cm air and a 500 µm thick aluminium window (Figure 3.2d).

The simulated dose $D_{\mathrm{e,\,sim}}$ is calculated by averaging the bin dose values of the sensitive volume V_0, which have the dimension GeV/g per single particle (electron) or equivalently the dimension Gy/pC per charge. Finally, to obtain the simulated average dose rate $\dot{D}_{\mathrm{e,\,sim}}$, the simulated dose must be multiplied by the bunch charge $Q = Q_0$ and repetition rate $f = f_0$ according to

$$\dot{D}_{\mathrm{e,\ sim}} = D_{\mathrm{sim}} \cdot Q \cdot f. \tag{3.10}$$

The results are shown in Table 3.1.

It can be seen that the simulated dose values are in the same order of magnitude as the analytically estimated value, which validates the simulation settings. As assumed, the absorbed dose in the test volume decreases from setup 1 to 4 in relation to the materials

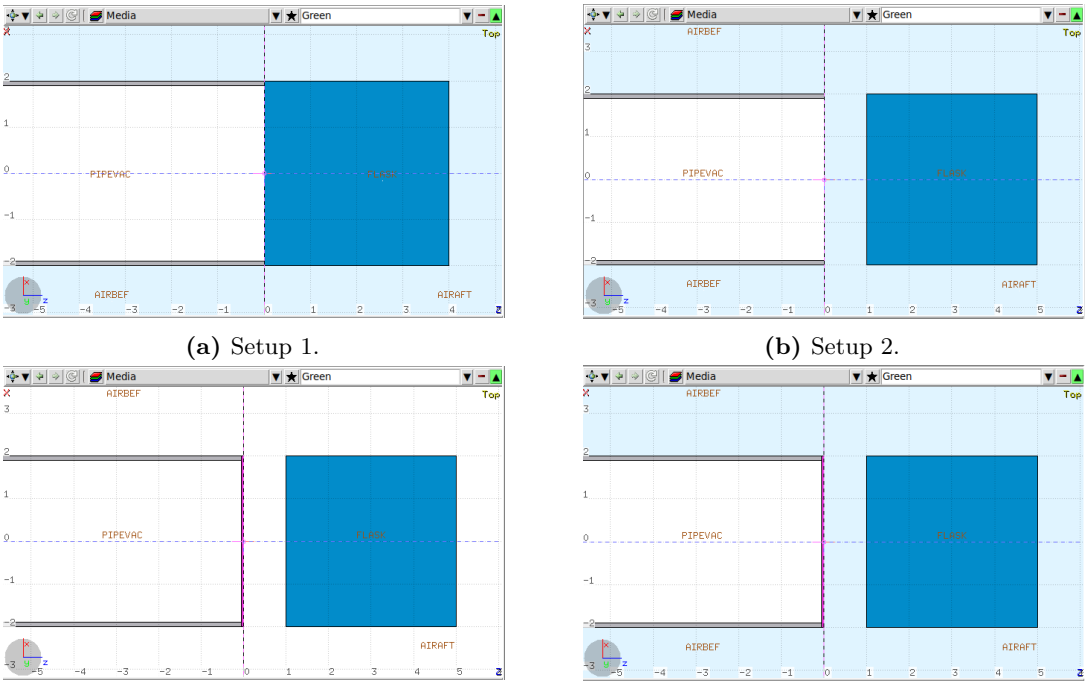

(a) Setup 1. **(b)** Setup 2.

(c) Setup 3. **(d)** Setup 4.

Figure 3.2.: FLUKA simulation geometries. Represented via the FLAIR geometry editor. Vacuum is represented in white, water in blue and air in light blue.

Table 3.1.: Simulated dose rates of the test setups 1 to 4 and beam types.

Setup	$\dot{D}_{\mathrm{e,\,sim}}$ in Gy/s			
	1	2	3	4
Point-like beam	170.25	170.07	8.63	8.67
Rectangular beam	165.61	161.06	8.38	8.38
Gaussian beam	79.38	79.05	7.94	7.91

and their thicknesses the beam has to penetrate before reaching the water target. The explanation for this is partly the energy loss and mostly the angular spreading of the beam. However, it is noticeable that depending on the simulated spatial beam shape in the xy-plane, the dose decreases strongly, more than 50 % in setup 1 and 2. A possible explanation for this is that in the case of a Gaussian beam, not all electrons hit the water target due to the spatial beam profile, but their trajectory, which is additionally modified by scattering, passes it. Thus, dose deposition by each electron does not occur in the volume used for the calculation of the average dose. At the same time, electrons reaching the water target at its edges can be scattered out of the considered volume, so the dose deposition again does not take place within the considered volume and is not taken into account. In the case of the point beam, each electron centrally hits the target (according to the estimation) and penetrates it almost in a straight line which is why the highest dose is also achieved here. In the case of the rectangular beam, although every electron hits the target at the beginning, some of them, for example the electrons hitting the target at its edge, are scattered from the considered volume, thus reducing the dose in the target volume. The fanning of the beam by the water target can be seen in Figure 3.1 which shows the deposited dose as projection on the xy-plane in arbitrary units. This fanning of the beam as it enters the water phantom leads to a significant dose reduction. Here, the broadening of the Gaussian beam and also of the rectangular beam is clearly visible, whereas the point beam fans out

Table 3.2.: Analytical dose rate estimates $\dot{D}_{\gamma,\,\mathrm{est}}$ for two monoenergetic square photon beams of the size 1 mm × 1 mm.

E in keV	μ_{en} in cm^2/g	Φ in $1/(\mathrm{s\,cm}^2)$	$\dot{D}_{\gamma,\,\mathrm{est}}$ in Gy/s
16	1.21	$3 \cdot 10^{10}$	0.093
40	0.069 47	$1.5 \cdot 10^{12}$	0.667

Table 3.3.: Simulated dose rates $\dot{D}_{\gamma,\mathrm{sim}}$ for two monoenergetic square photon beams of the size 1 mm × 1 mm.

E in keV	Φ_{sim} in $1/\mathrm{cm}^2$	$D_{\gamma,\,\mathrm{sim}}$ in GeV/g	$\dot{D}_{\gamma,\,\mathrm{sim}}$ in Gy/s
16	93.27	$1.7 \cdot 10^{-3}$	0.087
40	98.67	$2.7 \cdot 10^{-4}$	0.667

only slightly. As suspected, the electron beam is hardly influenced by the air, which can be seen by just the small dose drop in the second setup and the dose comparison from setup 3 and 4, where the presence of air makes virtually no noticeable difference to the dose generated. In contrast, the exit window represents a decisive barrier for the beam, which, in addition to a loss of energy, leads above all to scattering and fanning of the beam and thus to a significant dose drop. Overall, the achieved doses also equalize here, since the beam shape is already changed by the window.

3.3.2. Photon Beam - Absorbed Dose

A simple dose estimate for a mono energetic rectangular photon beam (1 mm × 1 mm) hitting a water target (4 cm × 4 cm × 4 cm) is shown in Table 3.2 for two energies $E = h \cdot \nu$, where ν is the frequency of the photons and h is the Planck constant.
In addition to the energy E, the mass-energy absorption coefficient $\mu_{\mathrm{en}}(E)$ and the photon flux density Φ are used to analytically estimate the dose rate $\dot{D}_{\gamma,\,\mathrm{est}}$ via

$$\dot{D}_{\gamma,\,\mathrm{est}} = \Phi \cdot \mu_{\mathrm{en}}(E) \cdot E. \tag{3.11}$$

The photon flux densities, measured in $1/(\mathrm{s\,cm}^2)$, used for the dose estimates correspond to the measured flux densities of the IMAGE beamline of the Karlsruher synchrotron KARA, see Chapter 5).

To determine the simulated absorbed dose $D_{\gamma,\,\mathrm{sim}}$, which is given in GeV/g per single particle, and compare them to the analytical estimated dose rate, the simulated initial photon fluence Φ_{sim} with the dimension $1/\mathrm{cm}^2$ is needed. To obtain the simulated dose in Gy, the simulated dose value in GeV/g has to be multiplied with the dimensionless factor $d = 1.6 \cdot 10^{-7}$ which results from a unit conversion. This enables the scaling of the photon flux density and thus the scaling of the simulated absorbed dose

$$\dot{D}_{\gamma,\,\mathrm{sim}} = \frac{\Phi}{\Phi_{\mathrm{sim}}} \cdot D_{\gamma,\,\mathrm{sim}} \cdot d. \tag{3.12}$$

The results of the analytical dose estimates, using Equation (3.11), and the simulated doses, using Equation (3.12), are shown in Table 3.2 and Table 3.3.

The simulated dose differs only very slightly from the analytically calculated dose. While the simulated and estimated dose rates match exactly in the case of 40 keV photons, the simulated dose rate of 16 keV is about 6.5 % smaller than the estimated dose rate. This can be explained by the larger mass-energy absorption coefficient μ_{en} for 16 keV photons, see

Table 3.2. Therefore, the energy deposition decreases when entering the water phantom about 12 % from the beginning over the depth of 1 mm. The energy deposition in reality is not constant as assumed in the estimation. Due to this, the simulated averaged dose over a depth of 1 mm in the volume 1 cm^3 should be about 6 % smaller than the estimated absorbed dose, which agrees well with the simulated dose reduced by about 6.5 %. The 6 % derivation corresponds approximately to the average of the initial energy deposition (0 % reduced) at the phantom surface and the 12 % reduced energy deposition at the depth of 1 mm. In the case of 40 keV photons, the energy deposition does not decrease noticeably due to the small mass energy absorption coefficient and can be assumed to be constant, so the simulated averaged dose is equal to the estimated dose.

The simulation and the settings for photon matter interactions in this case should meet the desired requirements and a more complex setup could be simulated. Further simulations with a slightly different setup, an air gap of 4 cm or an air gap of 4 cm and a beryllium window, yield almost identical dose rates, which applies to the less strong photon interactions and corresponds to the theoretic expectations.

The respective particle-matter interactions can therefore be simulated in almost any detail with the help of the FLUKA code, which enables a prediction of certain physical quantities. With the quantities obtained from the simulation, it is possible to compare the simulated ones to the corresponding data obtained from experiments.

4. Electron Irradiation Studies at FLUTE

This chapter first gives a brief overview of the linear electron accelerator FLUTE at IBPT and then presents initial dose measurements in collaboration with the DKFZ as well as estimates and dose simulations with FLUKA for FLUTE. Furthermore, some estimations regarding the beam exit window for the vacuum-air transition are given.

4.1. The Linear Electron Accelerator FLUTE

FLUTE is a short-pulse linear accelerator and terahertz source at KIT, developed and operated by IBPT. It is used as accelerator test facility for various studies in the field of accelerator physics, for example for the development of new diagnostic methods [38], but also in other fields like the generation and investigation of ultra short and intensive THz-radiation that can be used in the field of biology or materials science. Other applications can be found in [15].
In addition to THz-radiation, direct electron radiation also offers a wide range of possible applications outside of accelerator physics such as in the field of biology and medicine. The future goal is therefore to investigate new radiation methods in cancer therapy.

The basic building blocks of FLUTE are a laser-driven photo-injector, corresponding to the low-energy section of FLUTE, a linear accelerator, also called LINAC, and an electron bunch compressor, with which ultra-short electron bunches can be formed [15]. All the components are located in a 15 m × 14.5 m experimental hall surrounded by a 2 m thick concrete wall. This wall ensures the safety of experimenters staying in the control room and guarantees to meet the radiation protection requirements [39]. An overview of the FLUTE floor plan is given in Figure 4.1. The section that is relevant for the medical irradiation experiments in this thesis is the the low-energy section of FLUTE. Samples could be irradiated with electrons up to an electron energy of $E \approx 7\,\mathrm{MeV}$. With the installation of the LINAC after the upgrade, there will be the possibility to accelerate the electrons up to $E \approx 90\,\mathrm{MeV}$. In the future, there will be the option to use the bunch compressor to manipulate and minimize the electron bunch length, which could be used for different irradiation studies with special beam properties.
At the time of this work, the low-energy section of FLUTE was in operation and available for experiments. A schematic structure of all the individual components of FLUTE can be seen in Figure 4.2, where the low-energy section relevant for the thesis is marked with a box. Key components of the upgrade include a new gun laser and photo-injector electron source to accelerate the electrons to the mentioned energy via RF-energy provided by two new klystrons. The upgrade significantly reduces the dark current of FLUTE and provides a higher laser-induced charge. Overall, the operation of FLUTE will gain stability, simultaneously increasing the accuracy of radiation experiments.
After the emission and initial acceleration of the electrons, the electron beam is focused using a solenoid. To characterize the beam, various diagnostic elements are implemented in the FLUTE setup. They include, for example, BPMs (Beam Position Monitors), which

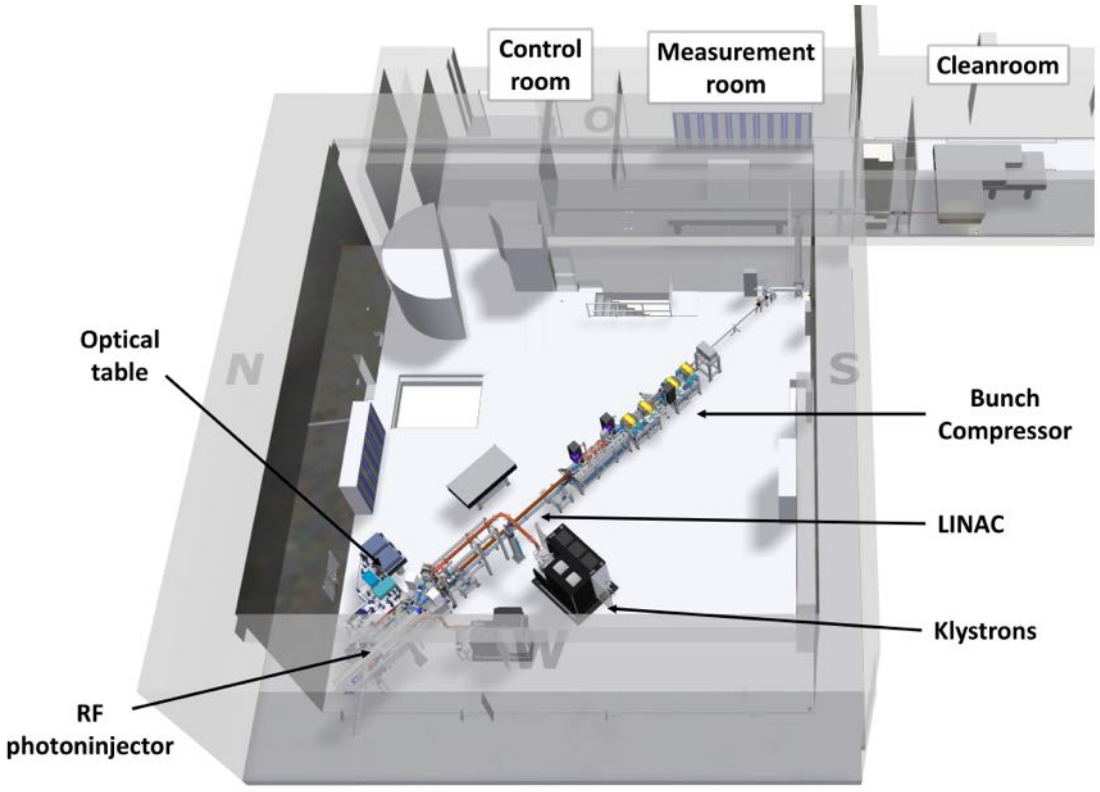

Figure 4.1.: FLUTE floor plan. Visible is the experimental hall with all scheduled components (low-energy section, LINAC and bunch compressor) of FLUTE, the control room, measurement room (e.g. for future THz-radiation experiments) and the cleanroom with the IR-Laser (800 nm).

measure the position of the beam, or a so-called ICT (Integrated Current Transformer), which determines the charge of the electron bunch via induction. After the diagnostic section, the beam then reaches the so called Split-Ring Resonator experiment, a new longitudinal diagnostics method, which will not be discussed further here. For a closer look, see [39]. Finally, the electron beam arrives at the low-energy spectrometer which is used to measure the energy of the electron bunch. For dosimetry and cell irradiation experiments, the Faraday cup following the spectrometer has to be replaced by an appropriate exit window. A Faraday cup, used for electron charge measurements, is normally installed there as a diagnostic device and beam dump.
A beam exit window is necessary to separate the vacuum inside the accelerator (typically 10^{-9}mbar) from the ambient air pressure in the experimental hall. To minimize undesirable

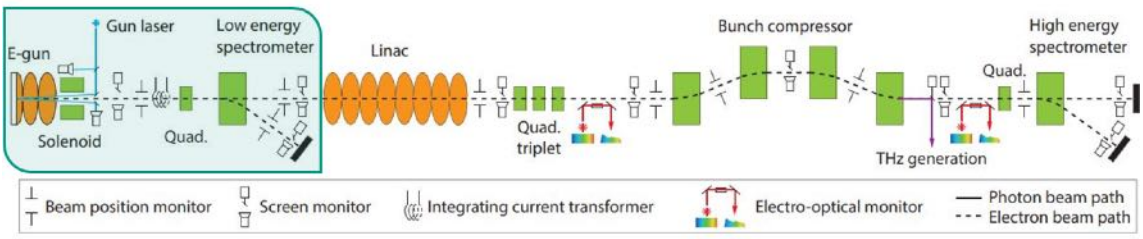

Figure 4.2.: Complete schematic setup of the accelerator FLUTE, including various diagnostic elements (not to scale). Magnets are marked in light green, RF components in orange. The low-energy section that is relevant for this thesis is highlighted with a box [40].

Table 4.1.: FLUTE parameters [15].

Parameter	Value
Electron energy	up to 90 MeV
Bunch charge	1 to 1000 pC
Pulse repetition rate	1 to 10 Hz
RMS bunch length after bunch compressor	1 to 300 fs

Table 4.2.: FLUTE settings during the depth dose measurement on May 6, 2022.

Accelerator operation setting	Value
Beam momentum[1]	4.84 MeV/c
Electron bunch charge[2]	348 pC
Electron bunch length (1σ)	1 ps
Pulse repetition rate	5 Hz
Solenoid current	75.7 A
RF power	5 MW
Phase setting: on crest	$-80°$
Beam size in vacuum (1σ)	0.8 mm
Beam size 10 mm after window (1σ)	2 mm

effects on the electron beam such as energy loss or broadening caused by the interactions of the electrons with the window material, it seems intuitive that the exit window should be made as thin as possible. The planned parameters of FLUTE at that construction stage are summarized in Table 4.1. Due to the energy and charge range as well as the bunch length, it is possible to create various beam irradiation settings to be tested and compare their effectiveness in future cell experiments. In general, for quantitative irradiation experiments, a wide quantitative dose determination process is needed in which the dose rate of FLUTE can be determined and then compared with literature and simulations.

4.2. First Dose Measurement at FLUTE

As part of the characterization of the dose rate of the linear accelerator FLUTE, a first dose rate determination was carried out in cooperation with the DKFZ by recording the electron depth dose curve of FLUTE. Setup, measurement and results are presented in the following sections.

4.2.1. Setup and Measurement

The measurement is carried out in the low-energy section of FLUTE, behind the low-energy spectrometer on the straight arm. The Faraday cup is replaced by a 150 µm thick exit window made of stainless steel.
In Figure 4.3, the schematic setup of the dose measurement is shown. The detector for dose measurement, a commercial ionization chamber (Roos Chamber) from the company PTW (Figure 4.4b), is located embedded in water-equivalent plates, a so-called solid water slab phantom (RW3), see Figure 4.4a. In general, they are just called phantoms and mimic the absorption behavior of tissue, which normally consists of approximately 80 % water, surrounding a tumor. The ionization chamber is placed at different depths by placing plates with various thicknesses in front of the plate with the ionization chamber in it. Between the exit window and the first plate, there is an air gap of approximately 10 mm. The settings of the electron beam during the measurement are noted in Table 4.2.

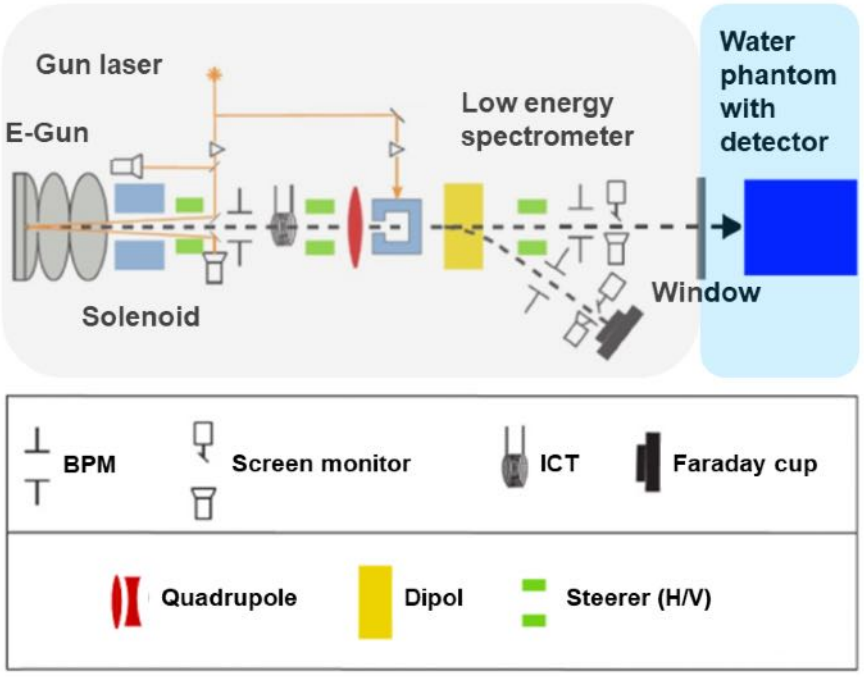

Figure 4.3.: Schematic low energy section setup of FLUTE for dose measurements. The accelerator section with ultra-high vacuum (10^{-9}mbar) is marked in light gray while the part outside the accelerator at ambient air is marked in light blue. Adapted from [41].

4.2.2. Results

Table 4.3 contains the measured accumulated mean charge over 40 s with the Roos chamber and the resulting dose values. Each single dose measurement for one depth is measured four times over a time period of $t = 40$ s. The measurement time t is taken manually. After the four identical dose measurements, the detector depth is adjusted to the new depth. Therefore, a different amount water equivalent RW3 plates is placed in front of the ionization chamber.
The electrometer connected to the Roos Chamber measures the electrons generated in the sensitive volume of the Roos Chamber by the incident ionizing electron beam during the irradiation time t. The measured charge in Coulomb is then converted into an absorbed dose using the calibration factor

$$k = 8.212 \cdot 10^7 \, \frac{\mathrm{Gy}}{\mathrm{C}}. \tag{4.1}$$

This factor is determined by the company PTW in advance for each detector.
Using the measured mean absorbed dose as a function of the phantom depth (Table 4.3), the depth dose curve shown in Figure 4.5 can be created. Here, the measured mean absorbed dose accumulated over 40 s is plotted against the depth of the detector in the phantom. The pattern of the depth dose curve corresponds to that of a typical electron depth dose curve shown in Figure 2.4 or 2.3. Due to the build-up effect, the maximal absorbed dose D_{max} is not reached at the phantom surface, but around a depth of 2 mm

[1] Corresponds to a total electron energy of about $E = \sqrt{E_0^2 + (pc)^2} = 4.87\,\mathrm{MeV}$.
[2] Correction of the bunch charge measured on May 6, 2022 by the ICT of $q_{\mathrm{meas}} = 175\,\mathrm{pC}$ with the determined correction function for the period from 2019 to May 20, 2022 [42]:
$q_{\mathrm{corr}} = 1.99 \cdot q_{\mathrm{meas}}[\mathrm{pC}] - 0.22\,\mathrm{pC} \approx 348\,\mathrm{pC}$

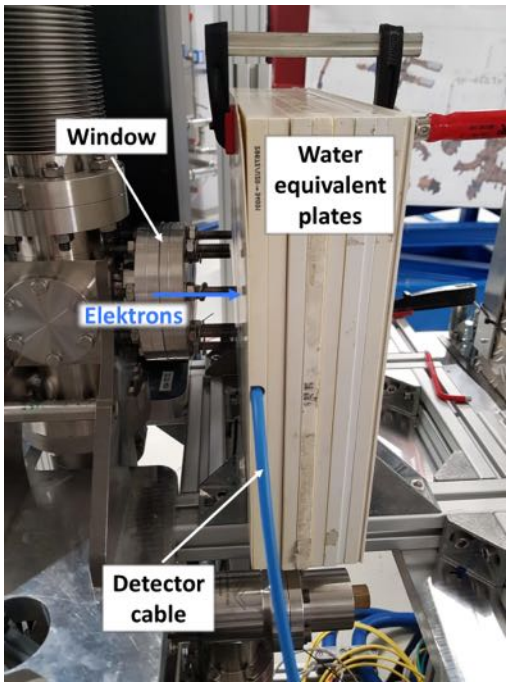

(a) Depth dose curve measurement setup at FLUTE. Courtesy: Christina Stengl (DKFZ).

(b) Ionization chamber: PTW Roos Chamber, air vented parallel plate ionization chamber. Courtesy: PTW Freiburg GmbH.

Figure 4.4.: Setup of the depth-dose curve measurement with phantom (RW3 Slab Phantom from PTW) and dose detector placed between. The measurement was conducted in cooperation with the DKFZ on May 6, 2022. Phantom positioning after the straight spectrometer arm of the low energy section.

with $\overline{D} = D_{\max} \approx 8.06\,\mathrm{Gy}$. This corresponds to a maximum dose rate of

$$\dot{D}_{\max} = \frac{D_{\max}}{t} \approx 0.2016\,\frac{\mathrm{Gy}}{\mathrm{s}}. \tag{4.2}$$

To estimate the kinetic entry energy of the electrons, the mean range $\overline{R}$ is needed according to Equation (2.34). It can graphically be extracted from Figure 4.5. With an estimated average range $\overline{R} \approx 15\,\mathrm{mm}$, the approximate kinetic entry energy is calculated to

$$E_0(\overline{R}) = 2.33 \cdot 1.5\,\mathrm{MeV} = 3.5\,\mathrm{MeV}. \tag{4.3}$$

Assuming an uncertainty of $\delta\overline{R} = 0.5\,\mathrm{mm}$, the uncertainty on the kinetic entry energy $\delta E_0(\overline{R})$ can thus be calculated using the uncertainty propagation law according to (Equation B.4). This yields

$$\delta E_0(\overline{R}, \delta\overline{R}) = \left|\frac{\partial E_0}{\partial \overline{R}}\right| \cdot \delta\overline{R} = \left(2.33 + 4 \cdot 7 \cdot 10^{-5} \cdot \overline{R}^3\right) \cdot \delta\overline{R} \tag{4.4}$$

And results in an uncertainty of $\delta E_0(\overline{R} = 1.5\,\mathrm{cm}, \delta\overline{R} = 0.05\,\mathrm{cm}) = 0.12\,\mathrm{MeV}$. Accordingly, the kinetic entry energy can be estimated as

$$E_0 = (3.50 \pm 0.12)\,\mathrm{MeV}. \tag{4.5}$$

See Section B for further explanations regarding the uncertainty consideration in this thesis.

The total energy E of the electrons is calculated to 4.87 MeV using Equation (2.1). Since the momentum measurement is subject to an uncertainty of approx. $\delta p = 0.001 \cdot p$, the uncertainty on the total energy of the electrons δE can also be calculated using the uncertainty propagation and Equation (2.1). The result reads

$$\delta E = \left|\frac{\partial E}{\partial p}\right| \cdot \delta p = \pm 0.005\,\mathrm{MeV}. \tag{4.6}$$

Table 4.3.: Measured average charge, mean absorbed dose $\overline{D}_{\text{meas}}$ and relative dose values of the depth dose measurement in cooperation with the DKFZ on May 6, 2022. Charge accumulation over $t = 40\,\text{s}$.

Depth in mm	Charge in nC	$\overline{D}_{\text{meas}}$ in Gy	Relative Dose in %
1	$96\ ^{+0.5}_{-0.7}$	$7.88^{+0.04}_{-0.06}$	97.8
2	$98.2\ ^{+1.5}_{-1.7}$	$8.06^{+0.12}_{-0.14}$	100.0
3	$97.5\ ^{+0.9}_{-1.1}$	$8.00^{+0.08}_{-0.09}$	99.3
5	$95.3\ ^{+0.9}_{-1.1}$	$7.83^{+0.07}_{-0.09}$	97.1
7	$93.3\ ^{+0.9}_{-0.7}$	$7.66^{+0.07}_{-0.05}$	95.8
10	$87.1\ ^{+1.5}_{-2.3}$	$7.15^{+0.12}_{-0.18}$	88.7
15	$50.3\ ^{+0.9}_{-0.9}$	$4.13^{+0.07}_{-0.07}$	51.2
20	$2.59^{+0.08}_{-0.07}$	$0.21^{+0.01}_{-0.01}$	2.6

The estimated entry energy from the measured depth dose curve is lower than the measured kinetic electron energy in vacuum with

$$E_{0,\,\text{kin},\,\text{meas}} = E_{\text{meas}} - E_0 \tag{4.7}$$
$$= (4.867 \pm 0.005)\,\text{MeV} - 0.511\,\text{MeV} \tag{4.8}$$
$$= (4.356 \pm 0.005)\,\text{MeV}. \tag{4.9}$$

The estimated entry energy differs from the kinetic energy of electrons in vacuum by about 19.7 %. The deviation of the estimated kinetic entry energy and the measured one can therefore most likely have no statistical cause. One probable explanation for this could be the angular spread which occurs when the beam passes through the exit window and the air gap, but due to the beam dimensions and the lager detector diameter, mostly all electrons should be detected nevertheless. Another explanation for the occurring energy deviation could be a kind of saturation of the detector. At the same time, it must be noted that this form of entry energy determination is only an approximation.

To compare and verify the measured dose values and to gain confidence in the detector used or find out whether saturation is present, an analytical estimation of the absorbed dose in water is carried out. The chosen water volume is equivalent to the sensitive volume of the Roos Chamber. In a further step, a more accurate analysis using FLUKA simulations with a replica of the measurement is performed.

4.3. Dose Estimation for the Roos Chamber

The approximate dose that the Roos Chamber should measure with its sensitive volume $V_0 = h \cdot \pi \cdot r^2 = 0.2 \cdot \pi \cdot 0.78^2\,\text{cm}^3 = 0.382\,\text{cm}^3$ can be determined in the same way as the dose estimation for electrons in Chapter 3.
The sensitive mass is estimated to $\Delta m = V_0 \cdot \rho_{H_2O} \approx 0.382\,\text{g}$ using the density of water as a basis for this calculation since the calibration factor specified by the PTW company already refers to the absorbed dose in water and not to the absorbed dose in air as the Roos chamber is a air vented parallel plate ionization chamber. A kinetic energy of 4.5 MeV is assumed for the electrons while neglecting the energy loss due to the stainless steel window and the air gap. The electrons will reach the water phantom with an energy of 4.5 MeV and penetrate 2 mm into the phantom until they reach the detector. By the time they

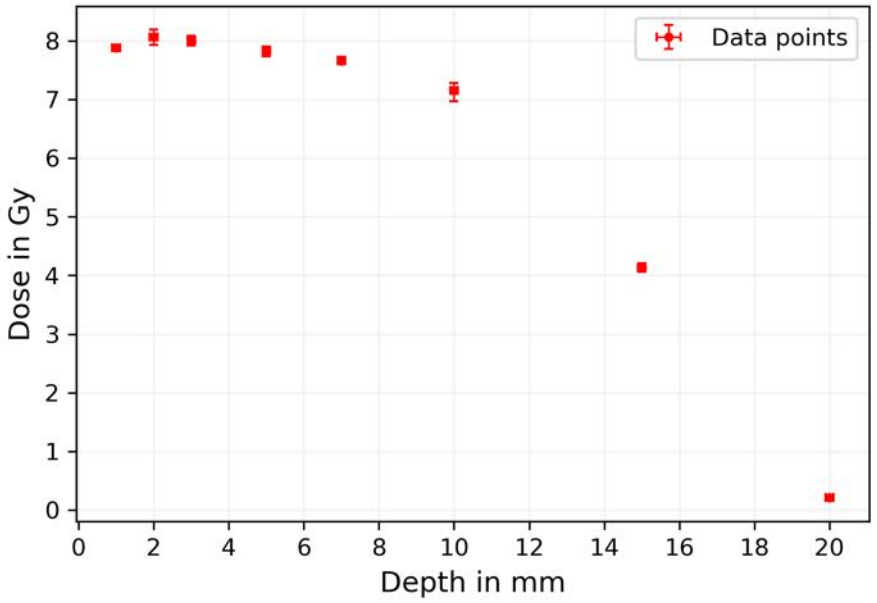

Figure 4.5.: Measured FLUTE electron depth dose curve. The setup includes RW3 material plates as a phantom and the Roos chamber from PTW as dose detector, an air vented parallel plate ionization chamber. An error of $\delta d = 0.1\,\mathrm{mm}$ for the detector depth due to the RW3 phantom data sheet of the manufacturer PTW is assumed. The asymmetric absorbed dose error as maximal and minimal deviation of the absorbed dose mean value out of the four measurements is shown. Initial total electron energy $E \approx 5\,\mathrm{MeV}$. Accumulated average dose over 40 s.

reach the detector, the electrons have lost an energy of about $\Delta E = 0.4\,\mathrm{MeV}$ according to Equation (2.5) and the stopping power taken from the NIST data base [36]. With an kinetic energy of approximately 4.1 MeV, they cover a distance of around 2 mm through the detector. One electron will deposit an energy of

$$\Delta E \approx \frac{\mathrm{d}E}{\mathrm{d}x} \cdot x = 1.935 \cdot 0.2\,\mathrm{MeV} = 0.387\,\mathrm{MeV}. \tag{4.10}$$

The generated absorbed dose D_n in the Roos Chamber due to one electron ($n = 1$, where n denotes the numbers of electrons) is then given by

$$D_1 = \frac{\Delta E}{\Delta m} = \frac{0.387}{0.382}\,\frac{\mathrm{MeV}}{\mathrm{g}} = 1.623 \cdot 10^{-10}\,\mathrm{Gy}. \tag{4.11}$$

The absorbed dose produced by an electron beam containing n electrons of single charge $q = e = 1.602 \cdot 10^{-19}\,\mathrm{C}$, corresponding to a total charge $Q = n \cdot e$ can be determined by the formula

$$D_\mathrm{n} = D_1 \cdot n = \frac{D_1}{e} \cdot n \cdot e = \frac{D_1}{e} \cdot Q \tag{4.12}$$

$$= 1.013 \cdot 10^{-3}\,\frac{\mathrm{Gy}}{\mathrm{pC}} \cdot Q\,[\mathrm{pC}] = \tilde{D}_1 \cdot Q = D_{\mathrm{Q[pC]}}. \tag{4.13}$$

With the assumption of a bunch current of $Q = 350\,\mathrm{pC}$ analogous to the measurement carried out, the dose per bunch is calculated accordingly

$$D_{\mathrm{Q=350\,pC}} = \tilde{D}_1 \cdot Q \approx 0.355\,\mathrm{Gy}. \tag{4.14}$$

With a repetition rate of 5 Hz which corresponds to five bunches per second, the averaged estimated dose rate for the Roos Chamber is

$$\dot{D} \approx 1.775 \, \frac{\mathrm{Gy}}{\mathrm{s}}. \tag{4.15}$$

It should be noted that in this estimation, as in all other estimations, only the bunch charge is taken into account. There is also a so-called dark current corresponding to electrons that are not generated by the laser pulses, but actually also deposit energy in the detector. The Roos Chamber should therefore detect an average dose from about at least 1.8 Gy during an irradiation time of $t = 1\,\mathrm{s}$. That corresponds to an average dose of $D_{\mathrm{est}} = 71\,\mathrm{Gy}$ for an irradiation time of 40 s analogous to the measurement.
Compared to the measured average dose ($\overline{D}_{\mathrm{meas,\,2\,mm}} \approx 8\,\mathrm{Gy}$), this deviates by a factor nine from the estimated result.
A possible reason for the rather large deviation from estimation to measurement could be the detector used for dose measurement. The calibration of an ionization chamber, in this case the Roos Chamber, is usually performed with a continuous source. In the case of FLUTE, it is a pulsed source which can affect the accuracy of the detector. The detector could be saturated since the ions are generated by very short, high-charge electron pulses, i.e. in a very short time, and this might overload the detector. Another reason could be the stainless steel window that may lead to an energy loss that is not negligible, but since the stopping power changes only slightly in the range of 3.5 MeV to 5 MeV [36], the dose differences should be very small. The scattering and fanning out of the electron beam because of the stainless steel window will probably have a serious impact on the dose and lead to a reduction. However, almost all electrons of the beam with a beam diameter of $\varnothing_{\mathrm{beam,\,air}} \approx 4.7\,\mathrm{mm}$ should still pass the detector with the larger diameter of $\varnothing_{\mathrm{RC}} = 15.6\,\mathrm{mm}$. By this consideration, the large difference between measured and estimated dose of a factor nine cannot be explained by the stainless steel window, which leads to the assumption that the large discrepancy is largely due to the detector. Overall, it is a sensitive and complex system with mutually influencing components. Because of this, it is not yet possible to say for sure what causes the large difference. As a result, further investigations into the suitability of the detector and the window used are necessary.
For example, the measurements of a depth dose curve could start with a low bunch current ($\approx 10\,\mathrm{pC}$) and this could then be slowly increased over the period of the measurement series. In the case of saturation, the curves should eventually converge.

Another influence could be the very short electron pulses, which have not been considered so far. So far, only the average dose rate has been considered. The deposited dose of an electron bunch is deposited in a period of t_{b}, which corresponds to the electron bunch length. In the following example the bunch length (FWHM) of FLUTE, see Table 4.1, with $t_{\mathrm{b}} = 2.4\,\mathrm{ps}$ is used. The peak dose rate of one single bunch is then given by

$$\dot{D}_{\mathrm{peak}} = \frac{D_{\mathrm{Q}}}{t_{\mathrm{b}}}. \tag{4.16}$$

In the case of the previous example, this results in an estimated peak dose rate of approximately

$$\dot{D}_{\mathrm{peak}} = \frac{D_{\mathrm{Q=350\,pC}}}{t_{\mathrm{b}}} \approx \frac{0.355\,\mathrm{Gy}}{2.4\,\mathrm{ps}} \approx 1.5 \cdot 10^{11} \, \frac{\mathrm{Gy}}{\mathrm{s}}. \tag{4.17}$$

To study the FLASH effect, dose rates above 40 Gy/s are needed as mentioned in Section 2.3.1. If the assumed electron bunch delivers an absorbed dose of 0.355 Gy in the sensitive volume V_0 within a time range of $t_{\mathrm{b}} \approx 2.4\,\mathrm{ps}$, i.e. the bunch length, then 113 bunches are needed to obtain 40 Gy. This would correspond to a continuous irradiation time of 271 ps, less than 0.3 ns. Accordingly, an average dose rate that should enable the FLASH effect could be achieved with a repetition rate and the previously mentioned

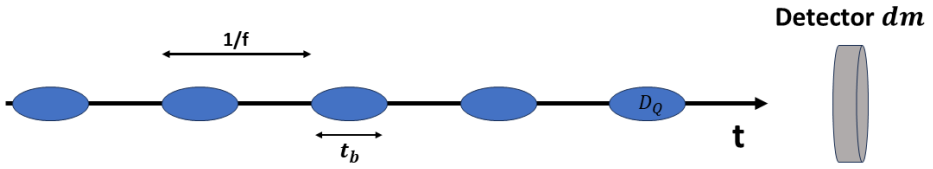

Figure 4.6.: Temporal electron bunch profile. Electron bunches are marked in blue. Time interval between bunches is regulated by the repetition rate f.

settings of not quite 120 Hz. An illustration of the temporally distributed electron bunches can be seen in Figure 4.6. Here, the question arises to what extent the detectors used are capable of registering high doses in this short time intervals since the specific dead times of ionization chambers must be taken into account. Due to these reasons, other detectors with shorter death times might be more suitable.

To validate the estimate and further check the measurement, the depth dose curve measurement is then simulated in a simplified manner using FLUKA. All necessary particle-matter interactions are implemented in the code and can thus provide a more accurate prediction of the expected dose. At the same time, the influence of the window thickness and the window material on the maximum achievable dose in relation to the depth is investigated. In the following, the peak dose rates are not considered further.

4.4. FLUKA Simulations

Below, various FLUKA simulations are carried out for dose determination at the FLUTE linear electron accelerator. First, a comparison is made between a simulated depth dose curve and the measured one. The setup is designed to resemble the setup used in the measurement performed together with the DKFZ as shown in Figure 4.4a. In the next step, different beam exit windows are simulated and considered mainly with respect to the influence on absorbed dose by material and thickness. The setup remains the same for all simulations. It should be noted that the simulations with different windows were performed with a beam width of $\sigma = 0.5\,\text{mm}$ in vacuum instead of $\sigma = 0.8\,\text{mm}$ as noted in Table 4.4. For the comparison of the simulation with the measurement, the same beam parameters are chosen, except for the beam width which was set to $\sigma = 0.8\,\text{mm}$. In general, the effect of the window and the phantom on the beam is much larger and therefore the influence of the different beam widths on the simulated dose in the phantom should be negligible, see Figure E.2.

4.4.1. Simulation Setup and Procedure

As in the measurement, there is an air gap between the exit window and the water phantom which is approximately 10 mm in the simulation (taking into account the window thickness). The water phantom is modeled after the dimensions of the RW3 plates and is integrated into the simulation as a compact water block measuring $30\,\text{cm} \times 30\,\text{cm} \times 30\,\text{cm}$. To represent the Roos Chamber, a simplified cylinder with a radius of 0.78 cm and a height of 0.2 cm was assumed, corresponding to the sensitive volume of the real detector. Since the dose conversion factor provided by PTW already determines the water-equivalent dose, water was chosen as material for the cylinder body instead of air actually present in the detector. To characterize the Gaussian shaped electron beam, the parameters selected in Table 4.4 are applied in the simulations. The chosen parameters are also adjusted to match the conditions present during the measurement. Each simulation is performed with 1 million

[3] Total energy $E = \sqrt{E_0^2 + (pc)^2} \approx 5.03\,\text{MeV}$

Table 4.4.: Electron beam parameters used for FLUKA simulations. A beam with Gaussian shape and energy spread is assumed here. These values correspond to the full width at half maximum (FWHM).

Parameter	Value
Beam momentum[3]	5 MeV/c
Beam momentum spread	0.011 77 MeV/c
Beam divergence	0.7809 mrad
Beam width in x-direction	0.1177 cm
Beam width in y-direction	0.1177 cm

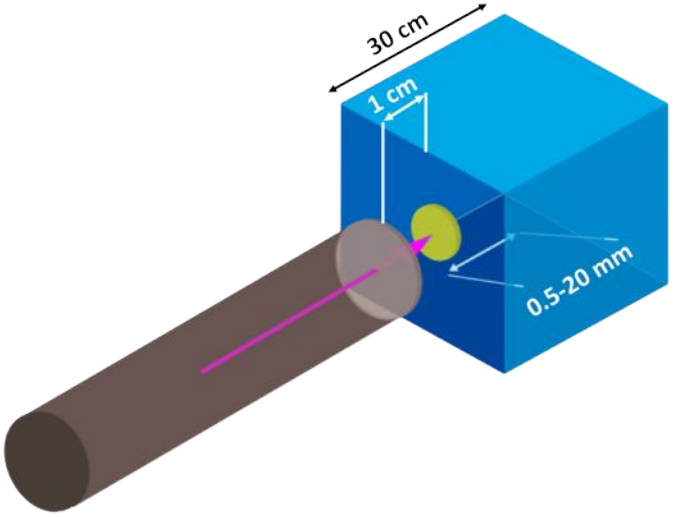

Figure 4.7.: FLUKA electron beam simulation setup. The electron beam (pink) first penetrates the beam-exit window (bright beige) and hits the detecting volume (yellow) after traveling through the water phantom and an air gap of around 10 mm. The water phantom is represented by a blue square, the vacuum beam pipe by a brown cylinder.

primaries ($N = 10^6$) to reduce uncertainty. In total, each simulation is carried out for each window material, window thickness and various depths of the sensitive volume. An overview of the simulation setup is shown in Figure 4.7. For this purpose, a standard template was created for each material, including the respective geometry, materials and beam parameters. Subsequently, using a custom Python program, derivative templates were generated. The derivative templates with adjusted window thickness and detector distance are then simulated with the FLUKA code. In post-processing, the relevant data is extracted from the simulation results as a txt-file.

In addition to the dose deposition in the detection volume, which is relevant for creating the depth-dose curves later, the dose deposition in the room and particle fluence are also considered. The generated result files list the respective information like the dose or fluence per bin. The number of bins must be defined before the actual simulation, with a higher number of bins resulting in a finer analysis grid. Cylindrical symmetry is assumed in the simulations for the virtual detectors due to the setup symmetry. The files are then processed and graphically displayed using Python. A more detailed procedure will be described in the corresponding sections.

4.4.2. Dose Calculation

To obtain a comparable depth-dose curve to the measurement, the average absorbed dose D_{sim} in the separately defined detection volume has to be determined. For this purpose,

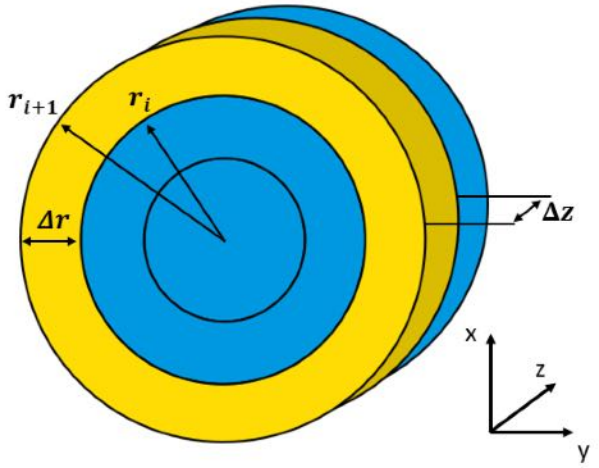

Figure 4.8.: Sketch of the FLUKA bin scaling for the dose detection volume. If there is only one bin chosen for 360°, the bin volume corresponds to a kind of ring (single bin marked in yellow) with radial bin width Δr and bin depth Δz.

the absolute dose per bin

$$D_i = D_{\text{stat}} \cdot Q \cdot f \cdot t \tag{4.18}$$

has to be calculated through the statistical distribution generated by the FLUKA Monte Carlo code with 1 million primaries and multiplied by the desired bunch charge Q, repetition rate f and irradiation time t. The received absorbed dose per bin has to be scaled by its bin mass $m_i = \rho_i \cdot V_i$ and summed up before being divided by the entire bin mass $M = \sum_i \rho_i \cdot V_i$. This yields the formula

$$D_{\text{sim}} = \frac{\sum_i D_i \cdot m_i}{M} = \frac{\sum_i D_i \cdot \rho_i \cdot V_i}{\sum_i \rho_i \cdot V_i} = \frac{\sum_i D_i \cdot V_i}{\sum_i V_i}. \tag{4.19}$$

This calculation provides the average absorbed dose in the detection volume with bin independent density $\rho_i = \rho$. Equation (4.19) can be rewritten for the case of the chosen cylindrical symmetry in case of a cylinder volume. The individual bins correspond to rings with area $\pi \cdot (r'^2 - r^2)$ whereby $r' = r + \Delta r$ and Δr correspond to the constant radial bin wide while Δz is equivalent to the constant bin depth. Due to the radial symmetry in contrast to cubic symmetry, the bins contribute differently to the mean dose due to their different sizes. Because of this, the bin volumes are not constant and the scaling has to be taken into account, see Figure 4.8. The simulated absorbed dose in the detector volume can thus be calculated using the formula

$$D_{\text{sim}} = \frac{\sum_i (D_i \cdot (2 r_i \Delta r + \Delta r^2))}{\sum_i (2 r_i \Delta r + \Delta r^2)} = \frac{\sum_i (D_i \cdot (2i+1))}{\sum_i (2i+1)}, \tag{4.20}$$

with $r_i = i \cdot \Delta r$. For the generation of the corresponding depth dose curves, Equation (4.19) is applied to each single simulation in a simulation series with constant window material and window thickness, but changing detector distance to the exit-window. An averaged energy dose value is determined for each detector depth. The relative uncertainties on the dose distribution given by FLUKA and the absolute uncertainties δD_i per bin derived from them with the identical prefactors (Q, f, t) give the mean uncertainty on the simulated absorbed dose δD_{sim} using again Equation (4.20) for the correct weighting of each uncertainty.

4.4.3. Comparison of Simulation Results with Measurement

The simulated depth dose curve based on the experiment with the DKFZ is shown in Figure 4.9. The expected course of an electron depth dose curve with the build-up effect

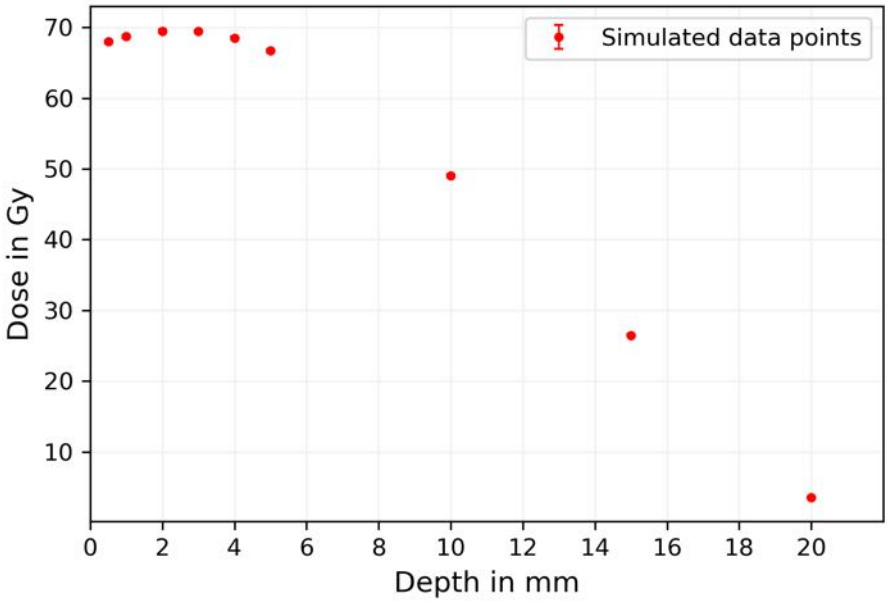

Figure 4.9.: Measurement based simulated electron depth dose curve for a 150 µm stainless steel window. The phantom depth is plotted on the abscissa while the accumulated average dose over $t = 40\,\mathrm{s}$ is plotted on the ordinate. Assuming five bunches per second and a bunch charge of 348 pC in comparison to the measurement at FLUTE. While the position of the detector is assumed to be exact, the uncertainty on the mean absorbed dose is in the order of 10^{-1} and thus not visible in the figure.

occurring at the entry into the water phantom and subsequent drop can be seen. In contrast to the measured depth dose curve, the simulated one shows a strong drop already at 5 mm and not only at 10 mm depth. Furthermore, the mean absorbed dose at a depth of 2 mm differs by a factor of almost nine, as did the estimation. Simulation and estimation, on the other hand, show a deviation of only about 1 %. However, the slightly reduced simulated dose ($D_{\mathrm{sim}} \approx 70\,\mathrm{Gy} < 71\,\mathrm{Gy} = D_{\mathrm{est}}$) can probably be explained by the exit window considered in the simulation, but not in the estimation. The delayed decrease of the measured depth dose curve possibly indicates a saturation of the detector. This can also be assumed with the maximum pulse dose of about 1 mGy in the data sheet of the Ross Chamber (Table C.1), since the maximum pulse dose during the measurement was 40 mGy and thus already higher by a factor of 40. After consultation with PTW, it became clear that the Ross Chamber is less suitable for pulsed and strong radiation sources and that other detectors such as the Advanced Markus Chamber could provide more reliable values, however, this has to be tested.

As with the measured depth dose curve (Figure 4.9), Equation (2.34) and Equation (4.4) can again be used to estimate the approximate entry energy of the electrons at the water phantom. The mean range can be approximately estimated to $\overline{R} = 13\,\mathrm{mm}$ which results in a kinetic entry energy of $E_0(\overline{R} = 1.3\,\mathrm{cm}, \delta\overline{R}) = 0.05\,\mathrm{mm}) = (3.00 \pm 0.12)\,\mathrm{MeV}$. As before, the kinetic entry energy calculated in this way is too low by almost 1 MeV, which is evident from the energy distribution generated by FLUKA as it enters the water phantom, Figure 4.10. The energy distribution generated by FLUKA shows a maximum at about 4.3 MeV with a steep decay towards 4 MeV. The few low-energy electrons seen in the energy distribution of the electrons entering the water phantom could probably have been produced by the interaction of the electron beam with the stainless steel window. On average, an electron thus loses an energy of $\Delta E = 0.2\,\mathrm{MeV}$ when passing the window. This is in

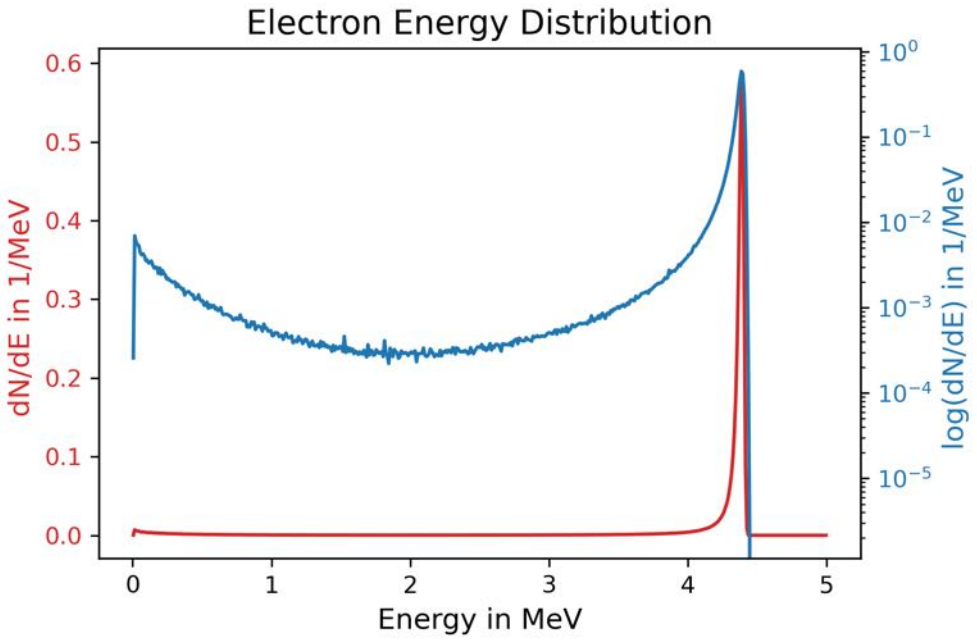

Figure 4.10.: Energy distribution of electrons entering the water phantom after a 150 µm stainless steel window based on the measurement ($\sigma = 0.8\,\text{mm}$). The plot features a logarithmic scale on the y-axis (blue) and a linear scale on the x-axis and y-axis (red). Statistical uncertainties given by FLUKA, which are in the order of 10^{-4}, are not shown.

agreement with the analytically estimated energy loss of electrons (Equation (2.5)) with the stopping power of stainless steel obtained from [36] of about $\Delta E = 0.2\,\text{MeV}$ passing through a 150 µm thick stainless steel window. Therefore, the estimate (Equation (2.34)) can only be used as a very rough size estimate.

For further analysis, not only the average detector absorbed dose is determined, but also the dose distribution in the entire space is considered. This provides an insight into how the dose is deposited in space. In Figure 4.11, the dose distribution in space, obtained from the simulation of the experiment with a 150 µm thick stainless steel window, is shown in a logarithmic color scale. As expected, no dose deposition occurs within the beam pipe, as it is under ultra-high vacuum conditions, and thus no interaction and energy deposition should take place. Once the beam reaches the exit window, the spatial dose distribution shows the broadening of the beam, deflection of primary particles, generation of secondary particles and particle backscattering. Within the water phantom, the beam is stopped and the electrons deposit their energy into the surrounding matter. Once again, beam spreading can be observed which is attributed to the entry of the beam into the water volume and leads to scattering and generation of lower-energy electrons ($\rightarrow$ build-up effect).
The deposited energy per bin is represented in Gy/pC. Due to the lower density of air ($\rho_{\text{air}} = 0.0012\,\text{g/cm}^3$) compared to the density of water ($\rho_{\text{H}_2\text{O}} = 1\,\text{g/cm}^3$) and thus the lower mass per bin, high doses are already reached in the air gap although the energy deposition is lower. In general, dose is approximately continuous between materials with different densities. Differences only arise due to the slightly different mass stopping powers.

4.4.4. Exit Window Studies with FLUKA

In this section, the results of considering the exit window properties with respect to the achievable dose, which should be maximized, are presented. In addition to the 150 µm stainless steel window, various materials (aluminum (Al), diamond (C), copper (Cu),

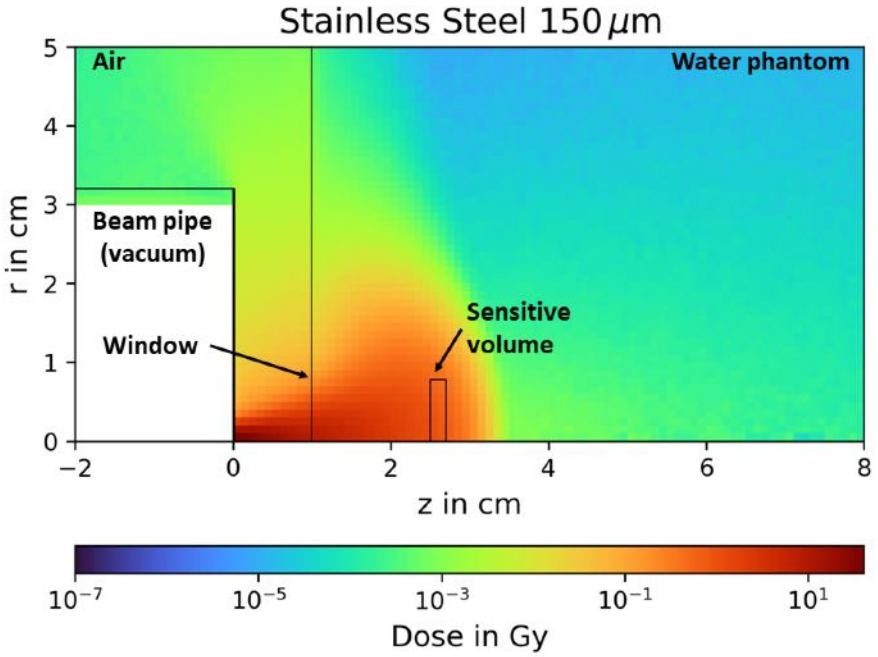

Figure 4.11.: 2D absorbed dose plot (side view) in logarithmic scale assuming rotational symmetry around the z-axis. Accumulated absorbed dose over 1 s, assuming five bunches per second and a bunch charge of 348 pC. Accelerator beam pipe, water phantom, and imitated Roos Chamber are marked separately. No dose deposition takes place inside the beam pipe under vacuum conditions as shown in white.

titanium (Ti), stainless steel, Kapton, Mylar, Havar) and window thicknesses in the range of 10 µm to 200 µm are simulated with a reduced beam wide $\sigma = 0.5$ mm.

Depth Dose Curves

The average energy doses per phantom depth are calculated based on the simulated data as already mentioned. Figure 4.12 shows the simulated depth dose curves with an accumulated mean absorbed dose over one second for eight different window materials with a constant window thickness of 150 µm. The curves represent typical electron depth dose curves and exhibit the typical slight increase in dose near the surface due to the build-up effect (see Chapter 2). As the density of the materials increases, the curves show a slightly flattened profile, and the dose maximum shifts towards the phantom surface. This development would coincide with the occurring energy loss of the electrons when crossing the window due to the higher stopping powers corresponding to their higher density and the lager angular spread. The simulated absorbed dose value at a depth of 2 mm varies between 1.68 Gy (Mylar) and 1.85 Gy (Cu) depending on the material for a 150 µm window. Thus, the simulation deviates by about 3.9 % to 5.6 % from the analytical estimate with about 1.78 Gy in which the window and the build-up effect was neglected. In the case of a stainless steel window with a window thickness of 25 µm to 200 µm, the dose values at a depth of 2 mm vary between 1.66 Gy and 1.85 Gy.This corresponds to a deviation of 3.9 % to 6.7 % from the analytical estimation. The achievable average maximum energy doses in one second differ by about 0.37 Gy in the case of different materials (Figure 4.12) and by about 0.33 Gy for stainless steel and 0.35 Gy for Havar in the case of different window thickness from 25 µm to 200 µm (Figure 4.13). Thus, it can be seen that the dose can be maximized by using a thin window with a material of a low density since Havar has a slightly higher density than stainless steel, cf. Table 4.5. As already expected, the influence of the window material and the window thickness regarding the progression of the curves and the maximal

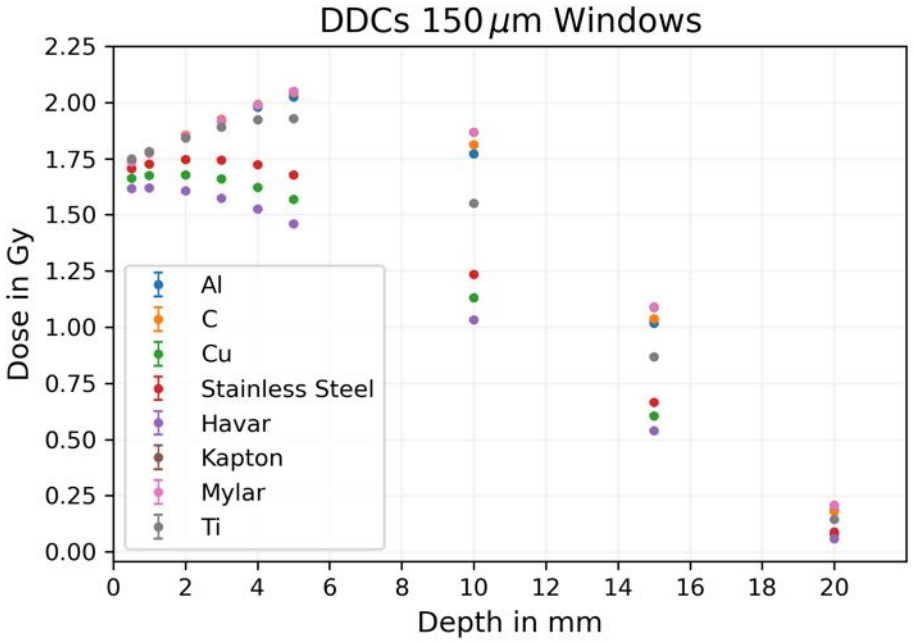

Figure 4.12.: Simulated electron depth dose curves for various window materials and a constant window thickness of 150 µm. The phantom depth is plotted on the abscissa, while the accumulated average dose over $t = 1\,\mathrm{s}$ is plotted on the ordinate. Assuming five bunches per second with a bunch charge of 348 pC. Assuming position of the sensitive volume as exact. The statistical uncertainty calculated by FLUKA on the dose value per bin is less than 2 %, so the absolute error is of the order 10^{-3} and therefore not visible in the plot.

average dose is likely to cause the discrepancy between simulation and simple estimation. Moreover, the influence of the air gap was not considered in the estimation and should be noted. While the simulations and analytical estimation are mutually consistent, there is still a difference of approximately a factor nine between the calculated values and the measurement.

Electron Fluence

The beam expansion caused by the interaction of the beam with the exit window could already be extracted from Figure 4.11 by the energy deposition in space. Additionally, the particle fluence which represents the number of particles N per unit area A can be analyzed. Using fluence, we can further examine the influence of the exit window on the beam geometry. Figure 4.14 shows a beam broadening when the thickness and density of the windows increase. In the case of stainless steel, the beam experiences a strong spreading effect whereas for materials with lower density like diamond, the beam is less scattered. Both the energy loss and the angular scattering are reduced. For a high electron density with high energies at the beginning of the water phantom, it is preferable to use a window material with low stopping power. This requires a low density or a very thin window, but it should still withstand the pressure difference of one bar. Therefore a high tensile strength, describing the maximum mechanical stress a material can withstand before breaking, is needed. A thin window with low density but high tensile strength allows the particle beam to be minimally influenced by the exit window. In that case, the beam can be guided towards the samples with approximately maximum electron number and starting energy. To investigate for example the FLASH effect, it is worthwhile to optimize the window in order to increase the average dose rate. Therefore, due to the significant impact of the exit

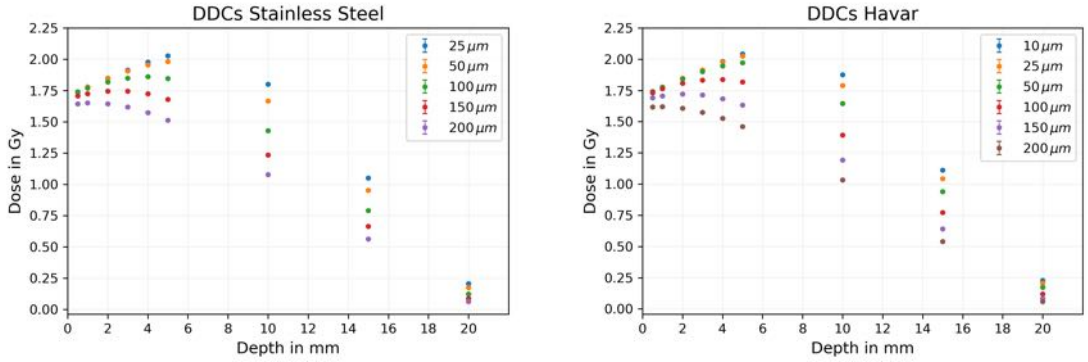

Figure 4.13.: Simulated electron depth dose curves for stainless steel (left) and Havar (right) windows for various window thicknesses. Assuming five bunches per second over one second with a bunch charge of 348 pC. Assuming position of the sensitive volume as exact. The statistical uncertainty calculated by FLUKA on the dose value per bin is less than 2 %, so the absolute error is of the order 10^{-3} and therefore not visible in the plot.

window regarding the achievable maximal average absorbed dose as seen before, particularly its material and thickness, separate window pressure tests with different windows will be conducted. For this purpose, several estimations are made.

4.5. Exit Window Estimations

Closely linked to the window stability and thickness is the window area. It plays a crucial role in the stability of the window. From a radiological perspective, having a relatively large window is advantageous as it makes the irradiation of a larger area possible. However, this would require a thicker window in order to prevent it from breaking under the prevailing pressure difference.
The minimum required thickness of a round window installed as in Figure 4.15 can be estimated using [43], namely

$$\sigma_{\mathrm{m}} > 0.75 \cdot p \cdot \frac{R^2}{h^2} \quad \Rightarrow \quad h > \sqrt{\frac{0.75 \cdot p}{\sigma_{\mathrm{m}}}} \cdot R. \tag{4.21}$$

This window should withstand the pressure difference and ensure its stability during operation. In the above formula,

- h is the minimum thickness of the window,
- p is the pressure difference across the window[4],
- R is the diameter of the window, and
- σ_{m} is the tensile strength of the material.

Therefore, considering the window thickness h, it is preferable to choose a window with a smaller radius R and a high tensile strength σ_{m}.

To choose an appropriate window, maximizing the dose for radiation experiments, stopping powers and tensile strengths of some materials should be considered. Table 4.5 shows that the mass stopping powers of the different materials (first column) vary by about 17 %, where the densities show a difference up to a factor of six (second column). Therefore, the stopping power (third column) mainly depends on the density of the material. With knowledge of

[4] $p = p_{\mathrm{atm}} = 1\,\mathrm{bar} = 1 \cdot 10^5\,\mathrm{Pa} = 0.1\,\frac{\mathrm{N}}{\mathrm{mm}^2}$

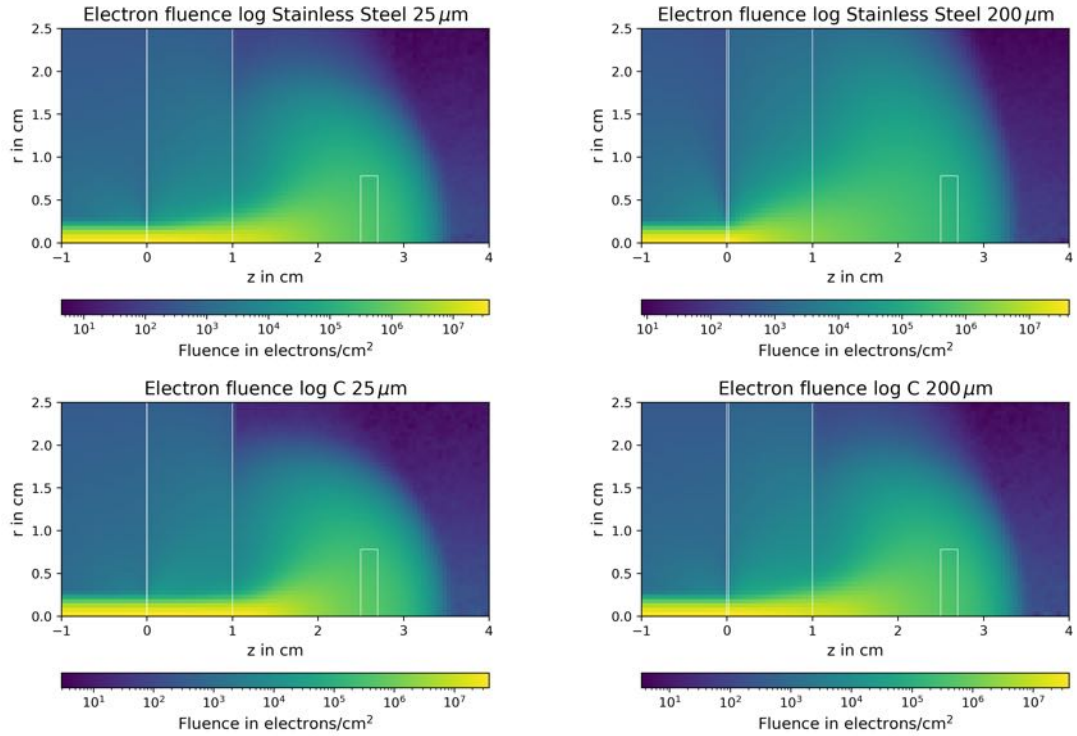

Figure 4.14.: Electron fluence plots (side view) for each 25 µm and 200 µm stainless steel and diamond exit window in logarithmic scale assuming rotational symmetry around the z-axis. Beam pipe, window, water phantom and sensitive volume are represented by white lines identical to Figure 4.11.

the tensile strength of a specific material, it is possible to estimate the minimum thickness $h_{\min}$ and energy loss ΔE of the beam using Equation (4.21) and (2.5). The calculations for some materials can be looked up in Table 4.6. All subsequent calculations are based on a window diameter of $R = 16\,\text{mm}$ as this size allows for irradiation of a well in a 24-well plate and has a manageable dimension. With a diameter of 16 mm, it is theoretically possible to use relatively thin windows, even referring to them as foils. A design for the foil holder, i.e. the exit window, is shown in Figure 4.16. Pressure load tests are planned to test the construction and materials, specifically stainless steel and Havar, as they allow for achieving thin window thicknesses and are readily available and cost-effective.

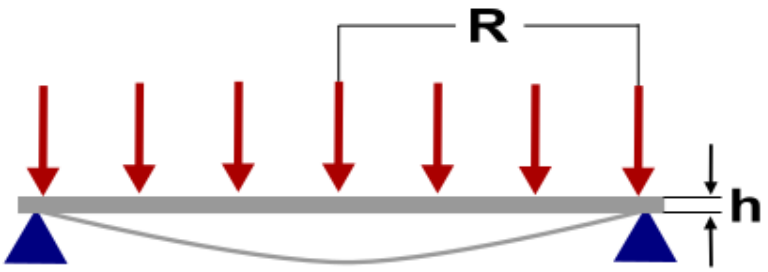

Figure 4.15.: Sketch showing round plate with clamped edge. Uniform pressure load represented by the red arrows leads to deformation of the window (thin gray line) with radius R and thickness h.

Table 4.5.: Various material properties for possible FLUTE windows. The corresponding stopping powers are taken from [36] for electrons with a kinetic energy of 4.5 MeV. Densities and tensile strengths are taken from [44], the tensile strength of Al from [45] and diamond from [46].

Material	Mass Stopping Power in MeV cm^2/g	Density ρ in g/cm^3	Stopping Power S in MeV/cm	Approx. Tensile Strength σ_m in MPa
Be	1.545	1.85	2.86	370
Ti	1.593	4.54	7.23	220
Mg	1.721	1.74	2.99	20
Al	1.664	2.70	4.49	84
Stainless Steel	1.599	8.00	12.79	560
Kapton	1.780	1.42	2.53	70
Diamond	1.684	3.51	5.91	2800
Havar	1.588	8.30	13.18	1860
Mylar	2.351	1.40	3.29	200

Further Experiments

As already mentioned, the windows will be tested for their load capacity on a separate setup. After successful modification and commissioning of FLUTE, further dose measurements are planned. In addition to the Roos Chamber, the Advanced Markus Chamber by PTW will also be tested. The spectrometer arm allows for a precise selection of the electron energy and the influences of dark current will be minimized with the new cathode after the upgrade.
For comparison purposes, the simulations will also be expanded and optimized accordingly. The goal is to characterize the dose profile of FLUTE which provides an opportunity for irradiating biological samples such as H460 lung cancer cells. Since horizontal irradiation is not possible due to the beam path, the samples need to be mounted vertically. One possible implementation is using hydrogels, the method which is described in Chapter 6. Due to the wide parameter range of FLUTE, various irradiation methods within the scope of cancer research could be tested on a long-term goal.

Table 4.6.: Calculated minimal window thicknesses and energy losses for a 16 mm diameter window, assuming a pressure difference of $p = p_{\mathrm{atm}}$.

Material	Min. Window Thickness h_{min} in µm	Energy Loss ΔE in keV
Be	114	33
Ti	148	107
Mg	490	147
Al	240	107
Stainless Steel	93	118
Kapton	262	66
C	42	24
Havar	51	67
Mylar	155	51

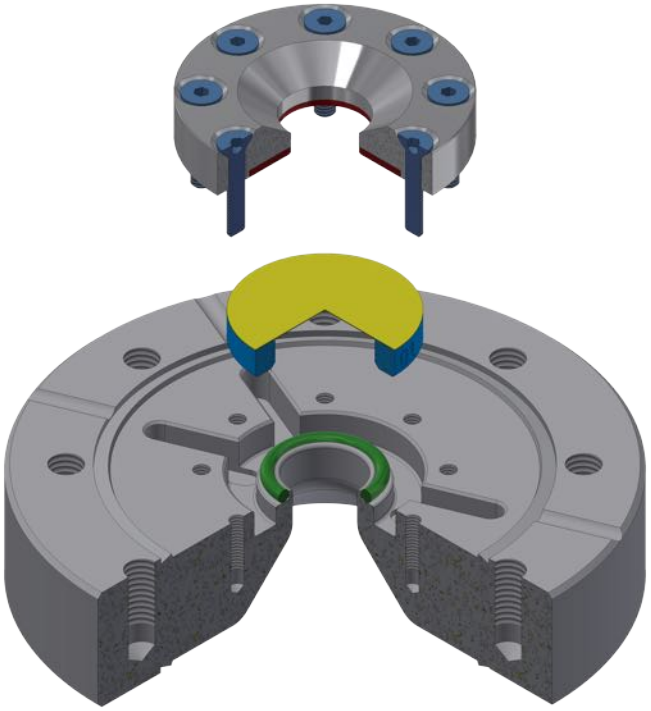

Figure 4.16.: FLUTE window test with a 16 mm diameter window, marked in yellow, and a 40 mm flange. The used o-ring is marked in green. Design by Steffen Schott (IBPT).

5. Photon Irradiation Studies at KARA

At the beginning, this chapter shall give a brief overview of the electron synchrotron KARA and the beamlines relevant for the thesis, LIGA I and IMAGE. In this context, first proof-of-principle experiments with radiochromic films at both beamlines as well as the subsequent evaluation procedure are presented. Finally, a verification with corresponding FLUKA simulations will be discussed.

5.1. The Electron Synchrotron KARA

KARA (Karlsruhe Research Accelerator) is a 2.5 GeV synchrotron storage ring and is used as a test facility in the field of accelerator physics and as a synchrotron light source. In general, synchrotron radiation is characterized by high brilliance and high photon flux densities [47]. In total, there are 23 beamlines tangential to the electron trajectory (Figure 5.1) at KARA. Every beamline uses different parts of the synchrotron spectrum depending on the experiments carried out there, such as lithography, tomography, experiments for the investigation of biological structures or irradiation studies for the investigation of different radiotherapy methods in cancer research. Other applications can be looked up in [14].

The synchrotron KARA provides a final electron beam energy of 0.5 GeV to 2.5 GeV. Before the electrons are accelerated to their final energy in the storage ring, they first pass a number of pre-acceleration sections. At the beginning, the electrons are generated by a thermionic E-Gun, which already accelerates the electrons to an energy of 90 keV. The electrons then pass through a racetrack microtron, where they are accelerated to an energy in the range of 53 MeV, until they are finally accelerated within one second in several turns to 0.5 GeV in the following booster. The booster is a small synchrotron with a circumference of 26.4 m. In a last step the electron bunches are injected into the storage ring where the energy can be ramped up to 2.5 GeV [48]. Typical modes of operation are either 2.5 GeV or 1.3 GeV. The produced synchrotron spectrum is then used by the beamlines. Two of them, LIGA I and IMAGE, are shortly described in the following sections, in connection with the first proof-of-principle experiments for radiation therapy in cancer research.

5.2. LIGA I Irradiation Test-Experiment with EBT-XD Films

The LIGA (acronym for “Lithographie, Galvanik und Abformung”) beamlines are operated and utilized by the Institute for Microstructure Technology (IMT). LIGA I (Litho 1), with a photon beam in the energy range of 2.2 keV to 3.3 keV, also called pink beam, is one of the three LIGA beamlines in the LIGA process, which was developed at IMT in the 1980s. All laboratories are located in a cleanroom environment, ensuring optimal environmental conditions and preventing sample contamination. For more information regarding the LIGA process, refer to [50, 51].

First irradiation tests are being conducted at LIGA I to test the reaction of radiochromic EBT-XD films from the company Gafchromic. The EBT-XD films used are sourced from

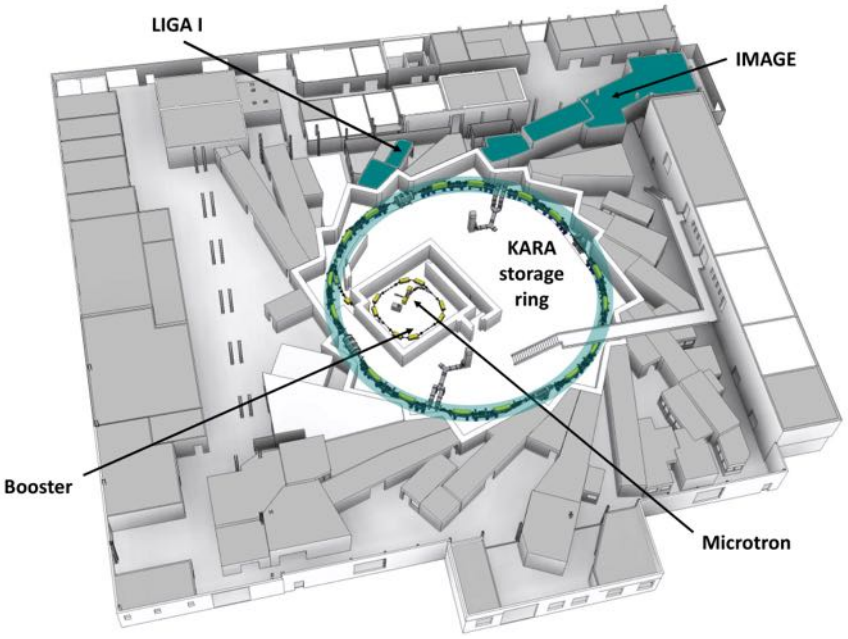

Figure 5.1.: KARA hall top view with the accelerator components and the beamlines tangential to KARA. LIGA 1, IMAGE and the storage ring itself are highlighted. Bending magnets are marked in yellow [49].

DKFZ, where they are routinely used alongside EBT3 films for various MiniBeam irradiation experiments because of their high spatial resolution. The advantage of EBT-XD films is that their optimal dose range is significantly higher than that of EBT3 films (0.4 Gy to 40 Gy versus 0.1 Gy to 10 Gy), meaning that film saturation is reached after very long irradiation times or in a short time, but with extremely strong sources. Testing the EBT-XD films is therefore a valid choice.

For this purpose, the EBT-XD film sheet was cut into three rectangles to fit behind an available mask for X-ray lithography at the Litho 1 setup. The mask ensures that the synchrotron radiation is blocked at the gold-coated areas and does not reach the film. The film-mask combination is then attached to the scanning station of Litho 1, which consists of a vertically movable scanning table. The next step is the evacuation and subsequent helium flooding of the exposure chamber to 100 mbar. Due to the evacuation of the experimental chamber prior to the experiments, the LIGA beamlines are unfortunately not suitable for cell experiments, but they are suitable for initial dosimetry tests and gaining experience with the dosimetry films. By opening the shutter, the pink beam enters the beamline and irradiates the EBT-XD film. How often the mask with the film is passed through the beam via the scanning station is related to the current in the storage ring and calculated out of it. Therefore the exposure value in mA min/cm is set in advance via the control rack. The LIGA 1 layout can be seen in Figure 5.2. In total, three irradiation samples are irradiated, with the exposure intensity reduced by a factor of 10 for each sample. The results are shown in Figure 5.3. In the case of the first irradiation with 265 mA min/cm, the used mask can only be roughly guessed. The EBT-XD film shows a significant blackness instead of a bluing, indicating possible saturation (Figure 5.3a). For the subsequent two irradiations (Figure 5.3b and 5.3c), the exposure time was significantly reduced. For the last irradiation with 3 mA min/cm, the film was scanned once by the beam using the scanner. Here, the pattern is most contrasting and the characteristic blue coloration of the radiochromic films is clearly visible (Figure 5.3c). However, it is also evident that a certain amount of radiation passes through the mask. In areas without a mask, all films have already turned black, indicating saturation. Therefore, the analysis of the film absorbed dose should not

Figure 5.2.: Picture of the LIGA I beamline [51]. Sample and mask inside the exposure chamber on the right, control rack to set irradiation values on the left.

be considered as a valid result. On the other hand, it cannot be excluded that the films behave differently under vacuum conditions and that this also leads to a modification of the polymer reaction in the films. For evaluation, the films need to be stored light-protected for approximately 24 hours before they can be scanned and further analyzed. In the case of the LIGA I irradiation, the analysis was performed by the DKFZ using their self-developed Matlab script. It converts the red color channel values of the EBT-XD film images into the corresponding absorbed dose at each reference location. Prior to the conversion, several calibration measurements were conducted using the MultiRad225 device available at the DKFZ. A more detailed description of the general evaluation process can be found in the following sections.

The determined film dose from about 10 kGy is thousand times higher than the maximum operational range of the film due to the EBT-XD data sheet. However, the experiment clearly demonstrates the high spatial resolution of the films and the presumably very high dose rate of the synchrotron radiation. In general, the films are not directly irradiated but are placed, for example in a water phantom, similar to the ionization chamber described in Chapter 4 for measuring the electron depth dose curve. This allows the determination of the corresponding medium height for later cell experiments, ensuring that the cells receive the desired dose. Therefore, similar irradiation experiments with EBT-XD films will be repeated while using the IMAGE beamline as the next step. Irradiation experiments at IMAGE can be performed in air under cell-friendly conditions. Because of this and already other biological experiments at IMAGE, the beamline proves to be suitable for the desired experiments.

5.3. IMAGE Beamline

The IMAGE beamline is another beamline of the KIT light source. Its main application is in the field of hard X-ray imaging in materials and biological sciences, with a focus on radiographic and tomographic imaging. The irradiation of samples can take place under ambient air. For a more detailed description of the possible applications of the IMAGE beamline, refer to [16].
Figure 5.4 shows the schematic layout of IMAGE. The irradiation of the EBT-XD films from Gafchromic takes place in EH2 (Experimental Hutch 2) at the position marked in the image. Unlike LIGA I, the IMAGE beamline does not utilize the dipole synchrotron radiation produced by electrons in the storage ring. Instead, it uses particularly intense synchrotron

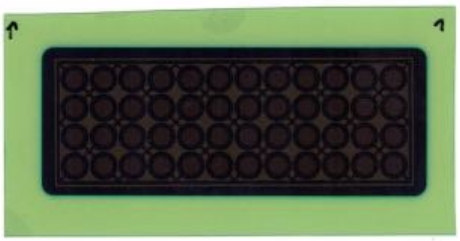

(a) EBT-XD film 1 after a radiation with 265 mA min/cm.

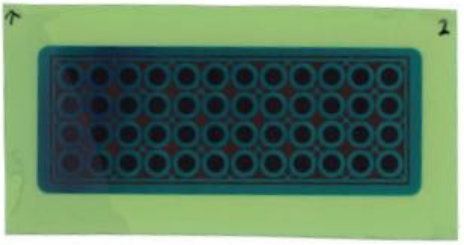

(b) EBT-XD film 2 after a radiation with 27 mA min/cm.

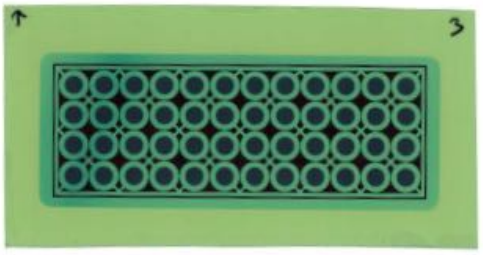

(c) EBT-XD film 3 after a radiation with 3 mA min/cm.

Figure 5.3.: Results of the EBT-XD film irradiation at LIGA I using a mask for X-ray lithography in front of the films. A blue to black discoloration shows the reaction of the film with ionizing radiation. The color intensity scales with the dose received. The black color indicates saturation. The original film color without irradiation corresponds to a yellow-greenish color tone.

radiation produced by a superconducting wiggler named "CLIC". A wiggler, closely related to an undulator, belongs to the class of insertion devices. These are special magnet structures that are installed in straight sections (insertions), leading to the corresponding nomenclature. Such insertion devices are used to generate a particularly strong synchrotron radiation. A typically schematic layout of this kind of insertion devices consisting of dipole magnets is shown in Figure 5.5. A distinction can be made between undulators and wigglers. The transition between these insertion devices can be mathematically described by the dimensionless undulator parameter

$$K = \frac{eB_0\lambda_\mathrm{u}}{2\pi m_\mathrm{e}c}. \tag{5.1}$$

The peak magnetic field on the undulator axis is denoted by B_0 and λ_u represents the undulator period which corresponds to the length of one period of the insertion device. After one undulator period, the magnetic field returns to its original value. The undulator parameter K is a measure of the strength of electron deflection, which is why, in general, a device is referred to as a wiggler when $K > 1$ and as an undulator when $K \leq 1$.
Due to the periodic alternating magnetic field, electrons passing through the insertion devices move along approximately sinusoidal paths. This multiple deflection leads to the emission of electromagnetic radiation known as synchrotron radiation, with an intensity or amplitude multiplication. In the case of an undulator, which has a weakly modulated field, a line spectrum is generated through partial coherent superposition and constructive interference of specific wavelengths. In contrast, a wiggler mainly results in an incoherent addition of the fields radiated at each pole. A wiggler is selected to have a strongly modulated field, leading to the generation of a continuous and broad synchrotron spectrum. The intensity I is proportional to the number N of undulator periods [52, 47, 53].

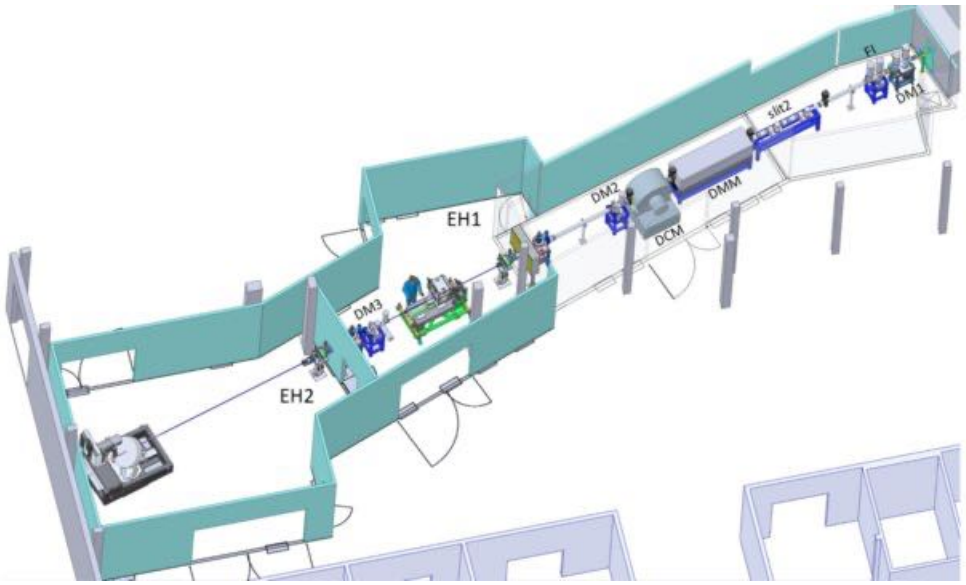

Figure 5.4.: Layout of IMAGE. Both experimental hutches, EH1 and EH2, are outlined. In addition, the positions of the DCM (Double Crystal Monochromator) and the DMM (Double Multilayer Monochromator) together with the diagnostic modules (DM 1, DM 2 and DM 3) including fluorescence screen, intensity monitor and profile monitor [16].

From the broad synchrotron spectrum generated, a desired photon energy is selected using a monochromator. For the IMAGE beamline, energies between 8 keV and 40 keV can be selected, when the beamline is operated in monochromatic mode (DCM or DMM). In the case of the EBT-XD film irradiation experiment, the monochromator was set to an energy of 16 keV. This choice is made to accommodate the slightly larger approximate rectangular irradiation area of 35 mm × 5 mm, compared to the 40 mm × 2 mm in the case of the 40 keV photon beam. Therefore, all experiments conducted below refer to the 16 keV photon beam of the IMAGE beamline.

Dose Estimation

To get an idea of the possible dose rate of IMAGE, a simple dose estimation is performed, similar to the case of the FLUTE electron linear accelerator in Chapter 3. The calculated values from Chapter 3 can be reused since the corresponding photon fluence rates of the IMAGE beamline were already used to validate the FLUKA settings for photon simulations. Using Equation (3.11) and assuming again a water target, the approximate surface dose rate in the case of the 16 keV photons is obtained as previously calculated

$$\dot{D} = 3 \cdot 10^{10} \, \frac{1}{\mathrm{s} \cdot \mathrm{cm}^2} \cdot 1.21 \, \frac{\mathrm{cm}^2}{\mathrm{g}} \cdot 16 \, \mathrm{keV} \approx 0.093 \, \frac{\mathrm{Gy}}{\mathrm{s}}. \tag{5.2}$$

For the 40 keV beam, a similar approach can be applied using the corresponding values for the selected energy. It yields an approximate surface dose rate $\dot{D} \approx 0.667 \, \mathrm{Gy/s}$.

In the next step, EBT-XD films will be irradiated at IMAGE using three slightly different setups, with time intervals ranging from 0 s to 60 s. By determining the color value of the films after irradiation, a calibration curve obtained from a previously calibrated source is needed. The corresponding dose for each irradiated film can be determined via that curve. This will enable the determination of the dose rate at IMAGE for the specific settings. The experimental procedure will be described in more detail in the next section.

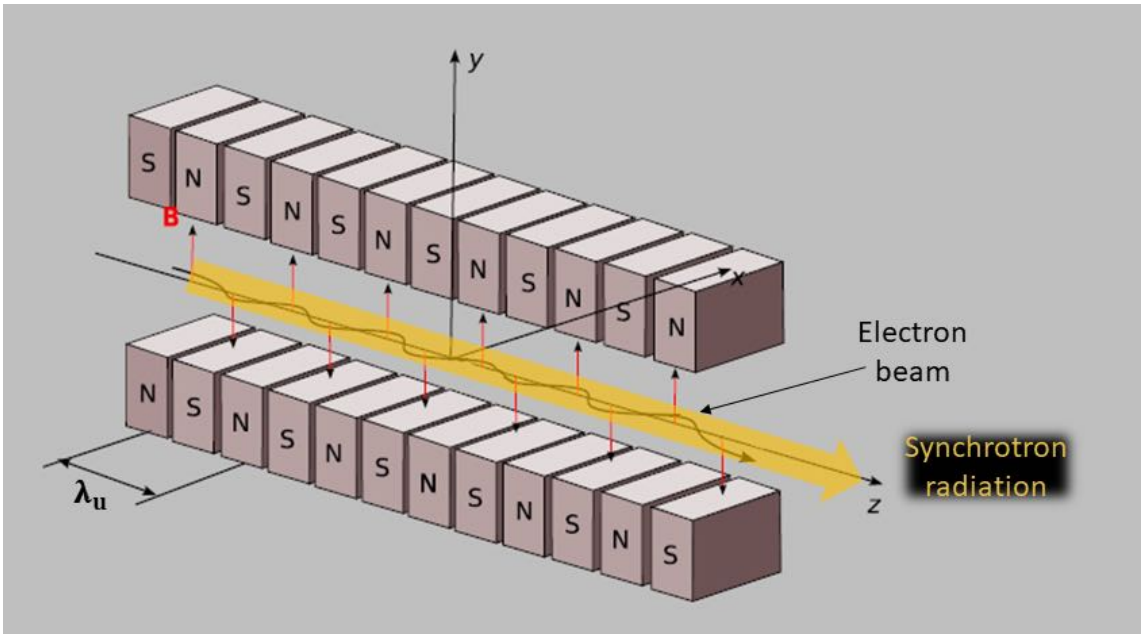

Figure 5.5.: General setup of an undulator or wiggler. Electrons are generated and accelerated by a proper source. After moving on a sine-like trajectory through the alternating magnetic field B (red) generated by dipole magnets, the electron beam is dumped. The synchrotron radiation (yellow) generated by the deflections is finally guided to the experiment. The undulator period is represented by λ_u. Edited figure taken from [52].

5.3.1. IMAGE Dosimetry Experiment with EBT-XD Films

To characterize the dose rate of IMAGE, initial measurements of the absorbed dose are performed using radiochromic films, specifically EBT-XD films from Gafchromic. These measurements aim to establish the foundation for further dose studies with the goal of characterizing the dose rate of IMAGE for applications in the medical field such as cancer research in radiology.
In the previous section, the general setup of the beamline was discussed. The photon beam passes through a 500 µm thick beryllium window, which closes the last vacuum section of the beamline. Afterward, the beam travels through a chamber flushed with helium (He). This protects the beryllium window from oxidation. Finally, the beam exits the helium chamber through a 80 µm thick Kapton window. In this way, the beam is extracted for the experiment in the experimental hutch 2.
Before the main experiment, the photon beam of the IMAGE beamline is centered. Figure 5.6a and 5.6b show parts of this centering process. After centering the beam, three different setups consisting of PMMA[1] plates and the EBT-XD films are installed in EH2 as illustrated in Figure 5.7. The following three setups were used:

- **Setup** $S_{\mathbf{5\,PMMA}}$: The phantom consists of 5 mm PMMA in front of the film and 10 mm PMMA behind the film.
- **Setup** $S_{\mathbf{10\,PMMA}}$: The phantom consists of 10 mm PMMA in front of the film and 10 mm PMMA behind the film.
- **Setup** $S_{\mathbf{0\,PMMA}}$: A blank EBT-XD film without a PMMA plate was used.

The photons will reach the sample holder with one phantom after the Kapton window and approximately 4 cm air. For the first two series of measurements (Figure 5.7b and 5.7c),

[1] Poly(methyl methacrylate), also known as acrylic glass or Plexiglas.

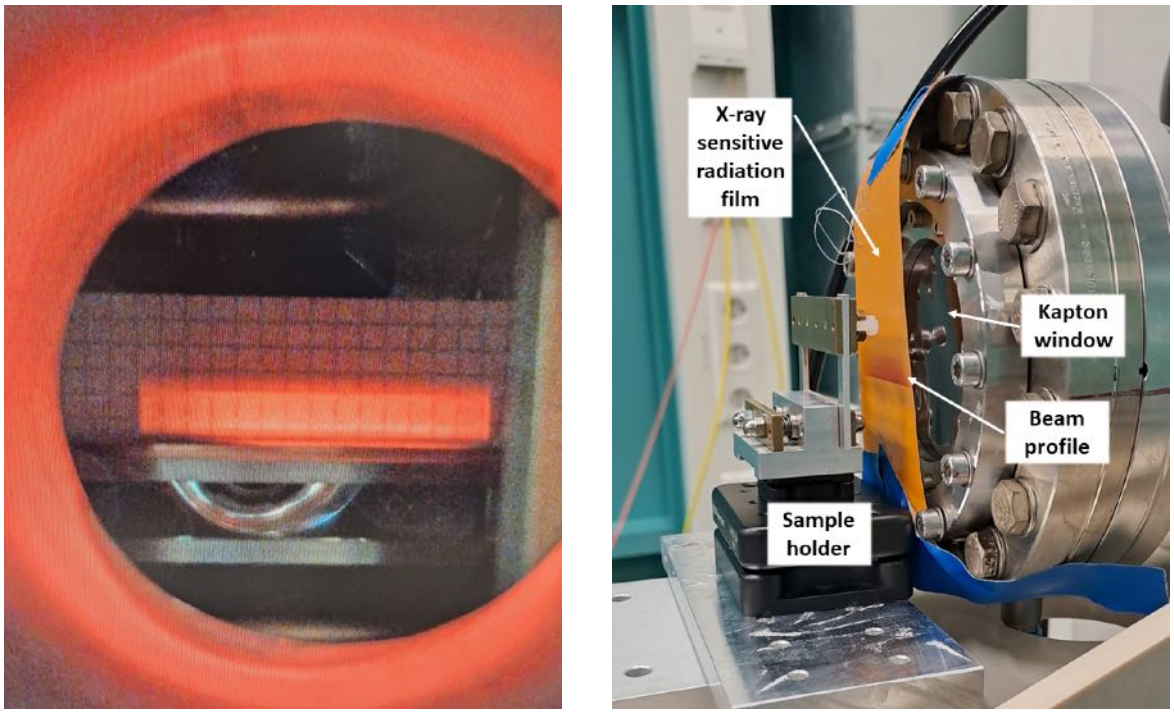

(a) Beam centering of the 16 keV photon beam in the beam pipe before the irradiation experiments, using the fluorescence screen on DM2.

(b) Beam positioning after the Kapton window. Photon beam position is made visible by an X-ray sensitive radiation film from GEX Corporation.

Figure 5.6.: Beam positioning process at IMAGE using a fluorescent screen (a) in the beam pipe and X-ray sensitive radiation paper (b) after the beam is extracted in EH2 at the approximate experiment position.

the EBT-XD films are placed between PMMA plates, which serve as a water phantom substitute. Here, the dosimetric relationship

$$z_{\mathrm{a}} \cdot \rho_{\mathrm{a}} \cdot \left(\frac{Z^n}{A}\right)_{\mathrm{eff,m1}} = z_{\mathrm{b}} \cdot \rho_{\mathrm{b}} \cdot \left(\frac{Z^n}{A}\right)_{\mathrm{eff,m2}} \tag{5.3}$$

between the two materials m1 and m2 is used, while Z defines the nuclear charge number and A corresponds to the atomic mass number [54]. In the case of a desired 4 mm water thickness in front of the films, Equation (5.3) yields, after some rearranging, a PMMA plate thickness of

$$z_{\mathrm{PMMA}} = z_{\mathrm{H_2O}} \cdot \frac{\rho_{\mathrm{H_2O}}}{\rho_{\mathrm{PMMA}}} \cdot \frac{\left(\frac{Z^n}{A}\right)_{\mathrm{eff,H_2O}}}{\left(\frac{Z^n}{A}\right)_{\mathrm{eff,PMMA}}} = 4\,\mathrm{mm} \cdot \frac{1}{1.18} \cdot \frac{227}{147} \approx 5.235\,\mathrm{mm}. \tag{5.4}$$

The corresponding values are taken from [54]. The exponent n can assume values between $1-4$ depending on the energy of the photon radiation. Since 16 keV photons belong to soft photon radiation, $n = 4$ is chosen. For the first irradiation experiments at IMAGE, three PMMA plates with the size of 3 mm × 5 cm were manufactured by the IBPT workshop: two plates with a thickness of 5 mm and one plate with a thickness of 10 mm. These plates represent a water phantom, due to Equation (5.3), and are designed to mimic the calibration setup at the DKFZ, allowing for the adjustment of the medium height to achieve the desired dose in subsequent cell measurements. Putting 10 mm PMMA behind the film sample, backscattering of ionizing particles is enabled in accordance with the irradiation of tissue.

In the first measurement series (Figure 5.7a and Figure 5.7b), the films are placed between a 5 mm plate (front plate) and a 10 mm plate (background plate). In the second measurement

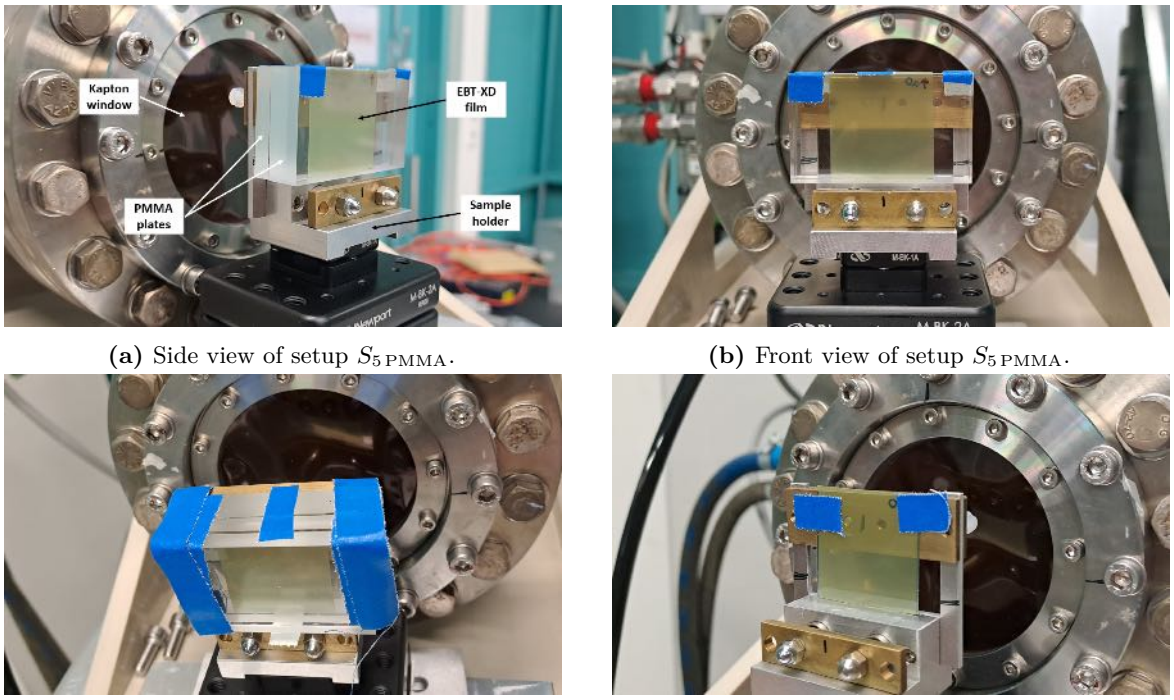

(a) Side view of setup $S_{5\,\mathrm{PMMA}}$.

(b) Front view of setup $S_{5\,\mathrm{PMMA}}$.

(c) Top view of setup $S_{10\,\mathrm{PMMA}}$.

(d) Setup $S_{0\,\mathrm{PMMA}}$.

Figure 5.7.: EBT-XD irradiation setups $S_{0\,\mathrm{PMMA}}$, $S_{5\,\mathrm{PMMA}}$ and $S_{10\,\mathrm{PMMA}}$ at IMAGE in EH2. Films placed between PMMA plates as a water phantom substitute. Fixed on the sample holder with adhesive tape.

series (Figure 5.7c), the films are sandwiched between 10 mm PMMA, in front of and behind the films, which should result in a corresponding reduction of the dose. In contrast, the last measurement series (Figure 5.7d) involves irradiating the bare films. This measurement series should provide the highest dose rate as the surface dose and photon depth dose curves should have their maximum dose at the phantom surface. The Gafchromic films are nearly tissue equivalent [10] and can be treated as a cell equivalent in this experiment.
All films used are cut into 3 cm × 3 cm squares (Figure 5.8). It should be noted that the film material is very brittle and can easily crack when cut, so precautions should be taken to avoid this. Additionally, it is important to consider the marked direction (arrow) as the response measurements are orientation-dependent [55] and to note this direction for each film (reproduce arrow direction), see Figure 5.8. In each measurement series, nine measurements are performed, gradually increasing the irradiation time of the films from 0 s to 60 s. The irradiation of the first film corresponds to opening and immediately closing the shutter. The timing is done using a stopwatch, starting from the sound of the shutter opening and ending with the sound of the shutter closing.

The measured times, the beam current at the time of the measurement in the storage ring and the received average doses can extracted from Table 5.1. To determine the respective average absorbed doses of the films (Table 5.1), the films are stored in a dark environment for approximately 24 hours. The films used for the calibration measurements were also stored for 24 hours so that the time-after-exposure for both is the same. With a long and equal time-after-exposure, the solid-state polymerization in the crystals of the active component decreases with time, so that the resulting dose error will be small [55]. The optical density of the films could be assumed as nearly stable. Afterwards, the films are scanned using an EPSON EXPRESSION 10000 XL scanner at 300 dpi. The scanning area is adjusted according to the film size and the arrow reference direction should also be considered during the scanning process.

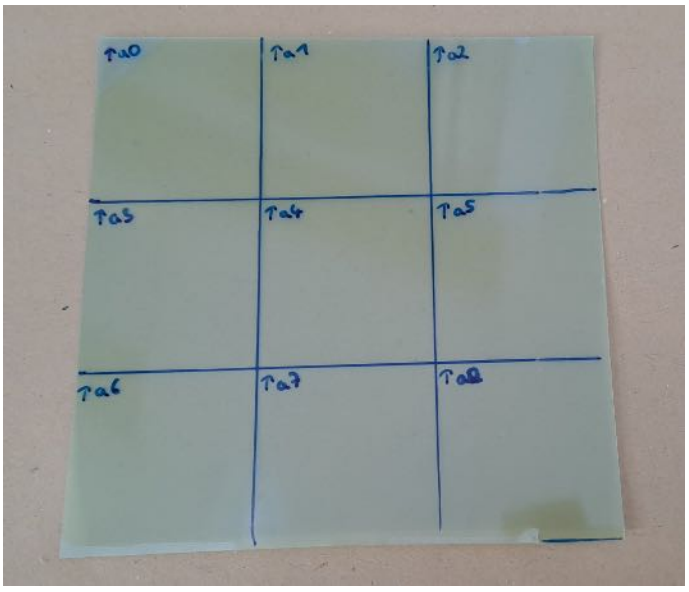

Figure 5.8.: EBT-XD sheet with film cutting pattern. Arrow markings for orientation reconstruction. Cut with sharp scissors. Since the film material is very sensitive, it should be protected from light exposure.

For image post-processing and analysis, a custom Python script is used, which is based on the analysis program written in MATLAB for the MiniBeam analysis at DKFZ.

In the first step, the calibration curve is determined. Calibration measurements were performed at DKFZ using a calibrated X-ray tube, the MultiRad225. EBT-XD films are irradiated in the MultiRad225 during the calibration measurement for durations ranging 0 s to 900 s. The calibration measurements were carried out twice. The obtained doses, cross-validated with an ionization chamber such as the Ross Chamber, is recorded for the respective irradiation times. A similar setup with 3D printed water-equivalent plates is used (4 mm plate in front and 12 mm plate behind the film or ionization chamber).

The calibration films are scanned in the same manner as the films in the measurement series. The Python program crops the scan to film size and there is also an option to remove damaged edges, as the dose cannot be accurately read from those regions. After the cropping using OpenCV-Python, a library of Python bindings, the RGB color values of the film scans can be read off. At this stage, only the red color channel is evaluated. For the calibration films, the optical density OD is averaged over the central film region of 140×140 pixels, which is calculated for each pixel based on Equation (2.38). In this case, I_0 represents the average red color channel value of a blank scan and serves as the reference value for determining the OD of all film image pixels.
With the knowledge of the optical density value OD of the calibration films, the corresponding dose calibration curve $D(OD)$ can be determined. For this purpose, the two OD data points obtained for a measured dose value using the Ross chamber were averaged, whereby the deviation from the OD value, which is in the order of 10^{-4}, is no longer taken into account. A fourth-order polynomial is used to fit the obtained data points from the calibration measurements. The obtained calibration curve (Figure 5.9) is given by:

$$D(OD) = a + b \cdot OD + c \cdot OD^2 + d \cdot OD^3 + e \cdot OD^4 \tag{5.5}$$

$$= (-1.3 - 3.7 \cdot OD + 103.2 \cdot OD^2 - 128.2 \cdot OD^3 + 141.6 \cdot OD^4)\,\text{Gy}. \tag{5.6}$$

Using the calibration curve, it is possible to assign the OD value of a film scan pixel to the corresponding dose value. With this knowledge, 2D dose plots as shown in Figure 5.10 can be generated.

Table 5.1.: Determined mean absorbed doses D_{meas} of the EBT-XD films for setup $S_{5\,\text{PMMA}}$, $S_{10\,\text{PMMA}}$ and $S_{0\,\text{PMMA}}$, measured irradiation times with an assumed uncertainty of $\delta t = 1\,\text{s}$ and measured beam current at the time of irradiation with the use of the calibration data received from the DKFZ. The reported mean absorbed dose is obtained by calculating the mean value of each film over a 140×140 pixel area of the scanned film. The standard deviation over this area is assumed as the uncertainty of the mean absorbed dose Section B. Measurement done on March 13, 2023 at IMAGE.

Setup	Film	Time in s	Beam current in mA	D_{meas} in Gy
	a0	*	114.5	0.09 ± 0.05
	a1	3	114.5	2.4 ± 0.6
	a2	5	114.3	3.6 ± 0.9
	a3	8	114.3	5.5 ± 1.3
$S_{5\,\text{PMMA}}$	a4	10.45	114.12	7.5 ± 1.7
	a5	15	113.94	13.0 ± 3.0
	a6	21.12	113.78	14.5 ± 3.3
	a7	30.36	113.66	21.2 ± 4.7
	a8	61.11	113.49	44.8 ± 10.1
	b0	*	110.61	0.96 ± 0.23
	b1	5.21	110.33	1.45 ± 0.32
	b2	7.34	110.17	2.3 ± 0.5
	b3	8.86	110.02	3.6 ± 0.8
$S_{10\,\text{PMMA}}$	b4	11.16	109.88	4.3 ± 0.9
	b5	15.94	109.73	6.3 ± 1.3
	b6	20.92	109.60	7.8 ± 1.7
	b7	32.30	109.45	12.4 ± 2.6
	b8	60.89	109.29	26.1 ± 5.5
	c0	*	112.99	0.05 ± 0.05
	c1	4.35	112.87	4.7 ± 1.3
	c2	6.52	112.73	8.6 ± 2.3
	c3	8.93	112.59	12.6 ± 3.3
$S_{0\,\text{PMMA}}$	c4	11.06	112.36	19.0 ± 5.0
	c5	15	112.22	28.0 ± 7.3
	c6	20.94	112.13	35.6 ± 9.2
	c7	30.71	112.01	52.9 ± 13.2
	c8	60.87	111.75	107.8 ± 24.6

By averaging the dose within the rectangular marked in Figure 5.10a-5.10e, an approximate average absorbed dose value $D(t)$ can be assigned to each film irradiation time, see Table 5.1. Plotting the averaged absorbed dose values as a function of irradiation time t (Figure 5.11) reveals a linear trend $D(t) = D_0 + m \cdot t$ with slope m and intercept D_0. The slope m in Gy/s obtained from the linear fit of the individual data points (Figure 5.11) provides the dose rates of the respective measurement series. The determined dose rates for all three setups are listed in Table 5.2. The obtained dose rates are significantly higher than the previously estimated rates. This can have various causes. On the one hand, the manual determination of the irradiation time introduces a considerable source of error. On the other hand, the calibration measurements were conducted with significantly higher-energy photons, so it is necessary to investigate how the photon energies affect the calibration measurements. New calibration measurements with lower photon energies would be needed. Additionally, different films should be tested, as the EBT-XD films used here may not be designed for the energy range used in the experiment and therefore may cause a large error

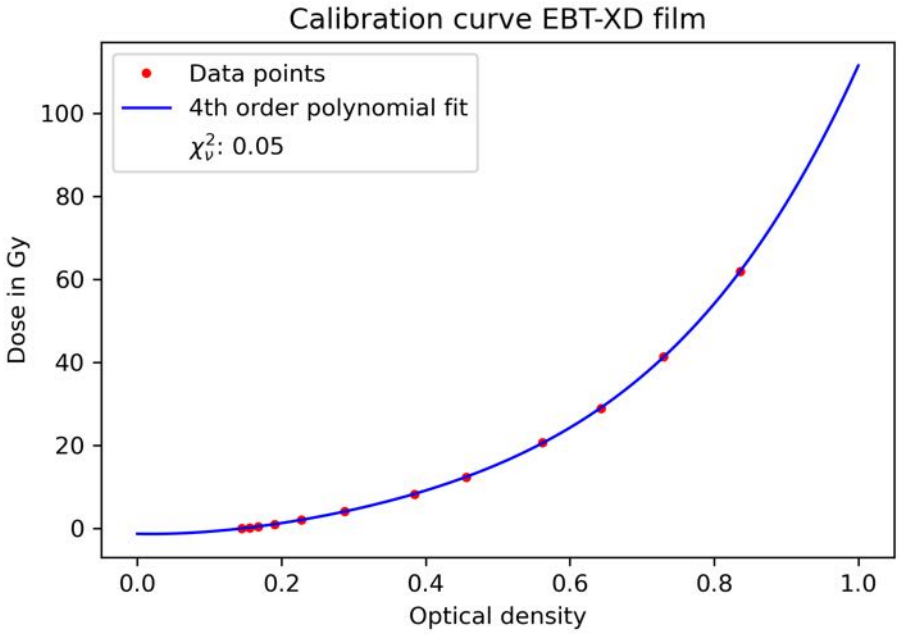

Figure 5.9.: EBT-XD film optical density to absorbed dose calibration curve calculated with given averaged calibration data from the MultiRad225 at DKFZ, using a fourth-order polynomial fit function.

Table 5.2.: Average dose rates of IMAGE for the 16 keV photon beam depending on setups $S_{5\,\mathrm{PMMA}}$, $S_{10\,\mathrm{PMMA}}$ and $S_{0\,\mathrm{PMMA}}$.

Setup	Average Dose Rate in Gy/s
$S_{5\,\mathrm{PMMA}}$	0.72 ± 0.02
$S_{10\,\mathrm{PMMA}}$	0.35 ± 0.04
$S_{0\,\mathrm{PMMA}}$	1.7 ± 0.1

[10]. Other films such as LD-V1 film, suitable for photons in the energy range of 20 keV to 200 keV, could be examined and compared in further measurement series.
Another optimization point is probably the beam position at the film sample. The beam hits the EBT-XD films in the lower half instead of the center. At the same time, an inhomogenity of the beam and a sharp lower edge can be observed. This could either possibly be due to the sample holder causing a truncation of the beam or the lower half of the beam being blocked by the beryllium window if the beam orbit was slightly lower than usual. Further improvements in the results may be achieved by readjusting the beam position to hit the center of the films. An optimization of the sample holder should be done as well. Additionally, incorporating the blue and green color channels into the analysis process for a more precise assignment of the OD value to a specific absorbed dose could provide a more accurate result.

Overall, a detailed response of the film to the received radiation can be observed, which provides motivation for further follow-up experiments. In the following, the measurement results will be compared with FLUKA simulations.

5.3.2. FLUKA Simulations

To further compare and gain insights into the measurement results, equivalent FLUKA simulations are performed for all three setups ($S_{5\,\mathrm{PMMA}}$, $S_{10\,\mathrm{PMMA}}$, $S_{0\,\mathrm{PMMA}}$) in accordance

(a) Film a4. Irradiation time $t \approx 10.45\,\mathrm{s}$.

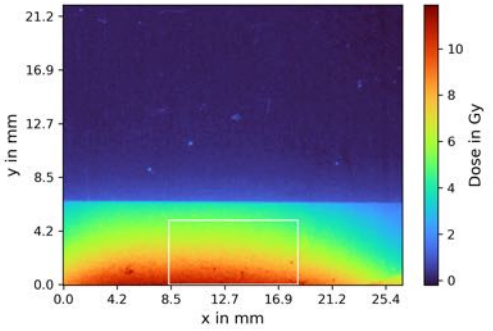

(b) Generated 2D dose plot of film a4.

(c) Film b4. Irradiation time $t \approx 11.16\,\mathrm{s}$.

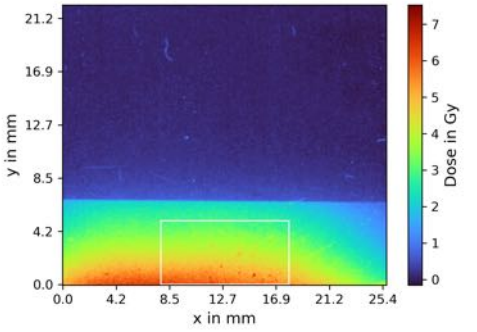

(d) Generated 2D dose plot of film b4.

(e) Film c4. Irradiation time $t \approx 11.06\,\mathrm{s}$.

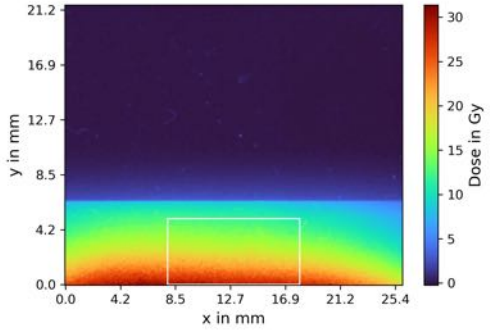

(f) Generated 2D dose plot of film c4.

Figure 5.10.: Irradiated EXT-XD films after an irradiation time $t \approx 11\,\mathrm{s}$ and 2D absorbed dose profiles after $t = 11\,\mathrm{s}$ for the setups $S_{5\,\mathrm{PMMA}}$, $S_{10\,\mathrm{PMMA}}$ and $S_{0\,\mathrm{PMMA}}$. The region used determine the average dose per film is marked with a white rectangle inside the dose profiles.

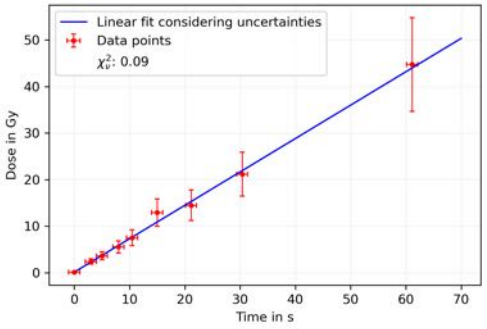

(a) Measurement series setup $S_{5\,\mathrm{PMMA}}$.

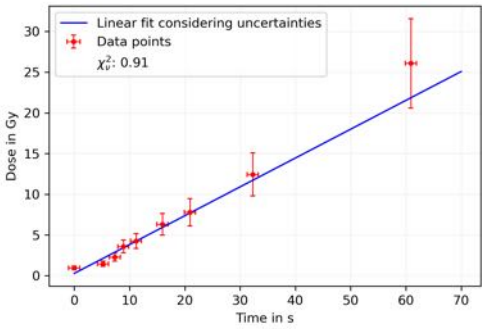

(b) Measurement series setup $S_{10\,\mathrm{PMMA}}$.

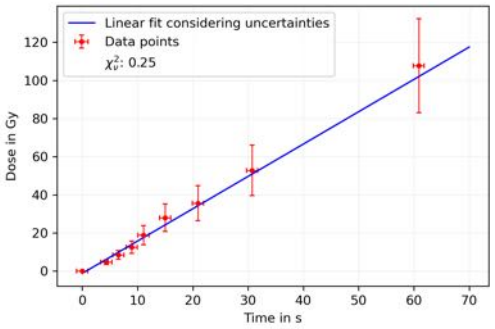

(c) Measurement series setup $S_{0\,\mathrm{PMMA}}$.

Figure 5.11.: Setup-dependent dose evolution over time at IMAGE. On the ordinate, the average dose D per EBT-XD film is plotted against the corresponding film irradiation time t on the abscissa. A linear progression can be seen in all three measurement series for the setups $S_{5\,\mathrm{PMMA}}$, $S_{10\,\mathrm{PMMA}}$ and $S_{0\,\mathrm{PMMA}}$. Assuming an uncertainty on the time of $\delta t = \pm 1\,\mathrm{s}$. The uncertainty of the mean absorbed dose is given through the standard deviation. Linear regression to obtain the specific dose rate $\dot{D}_{\mathrm{meas}}$ which is given by the slope m of the fit.

with the experimental setup (Figure 5.12a, 5.12b and 5.12c). In addition to the 16 keV beam used in the experiment, identical simulations for the same three setups with 40 keV photons and corresponding beam parameters are conducted. For the film dose comparison, the active layer of the Gafchromic films is simulated using a tissue-equivalent material (A-150). In this layer, the dose is determined and a 2D dose plot to compare with the experiment is generated. The beam simulation settings are summarized in Table 5.3. Figure 5.13 shows the simulated dose profiles for an assumed irradiation time of approximately 11 s for the 16 keV photon beam in all three setups. Additionally, the dose profiles after an irradiation time of 11 s for the 40 keV photon beam are shown in Figure 5.14. In contrast to the experiment, direct edges are not visible here, but the appearance of the upper half of the dose profile closely resembles that of the irradiated films, which supports the hypothesis that the photon beam may have only partially hit the film samples and was cut off.

Similar to the experiment, averaging was performed with the simulated absorbed energy accumulated over $t = 11\,\mathrm{s}$ per pixel in the white rectangle, marked in both figures, using Equation (3.12) and the measured and simulated photon flux density Φ and photon fluence Φ_{sim} from Chapter 3. Assuming a linear absorbed dose behavior in time, the respective mean dose rates were determined using Equation (3.12) without accumulating over a irradiation time t and calculating the mean of the marked rectangle. The standard deviation of the considered area is again chosen as uncertainty on the calculated mean dose rate. The statistical uncertainty on the dose per bin provided by FLUKA is not considered here,

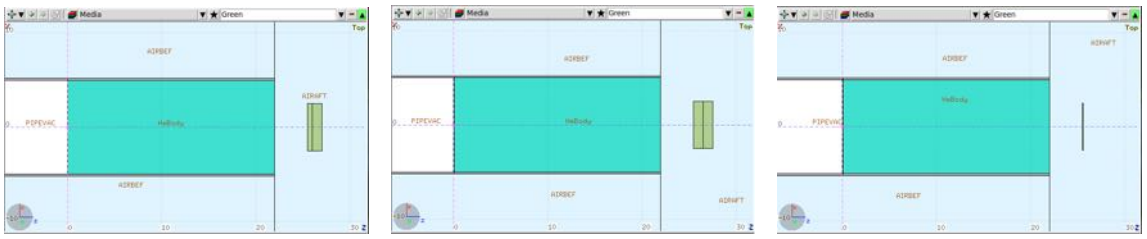

(a) FLUKA simulation geometry $S_{5\,\mathrm{PMMA}}$.

(b) FLUKA simulation geometry $S_{10\,\mathrm{PMMA}}$.

(c) FLUKA simulation geometry $S_{0\,\mathrm{PMMA}}$.

Figure 5.12.: Simulated IMAGE geometries with FLUKA, shown in the FLAIR geometry viewer. Constructed according to the three irradiation setups $S_{5\,\mathrm{PMMA}}$, $S_{10\,\mathrm{PMMA}}$ and $S_{0\,\mathrm{PMMA}}$ used for the irradiation of the EBT-XD films at the IMAGE beamline. Vacuum colored in white, air in light blue, helium in turquoise, PMMA in a green-yellow color and the rebuilt of the 25 µm thick EBT-XD active layer in pink using the material A-150, a tissue-equivalent plastic.

Table 5.3.: Photon beam settings (IMAGE) used for FLUKA simulations. Beam with Gaussian shape and no energy spread is assumed here. These values correspond to the full width at half maximum (FWHM). The primary number was set to $N = 10^9$ for all simulations.

Parameter	16 keV Photons	40 keV Photons
Beam momentum	16 keV/c	40 keV/c
Beam momentum spread	0 keV/c	0 keV/c
Beam divergence	0 mrad	0 mrad
Beam width in x-direction	35 mm	40 mm
Beam width in y-direction	5 mm	2 mm

since the relative uncertainty is less than 10 % in the relevant area. The simulated mean dose rates $\dot{D}_{\mathrm{sim}}$ and the maximum resulting dose rates $\dot{D}_{\mathrm{sim,\,max}}$ per bin are summarized in Table 5.4. For ease of reference, Table 5.5 lists the estimated, averaged simulated and averaged measured dose rates as well as the ratio $F = \dot{D}_{\mathrm{meas}}/\dot{D}_{\mathrm{sim}}$ between average simulated and measured dose rates for the 16 keV photon beam. The estimation of dose rates at the location of the EBT-XD film for setups $S_{5\,\mathrm{PMMA}}$ and $S_{10\,\mathrm{PMMA}}$ is carried out analogously to the setup $S_{0\,\mathrm{PMMA}}$ via Equation (3.11). For the first two cases, the reduced photon flux densities calculated via the Beer–Lambert law (Equation (2.15)) are used here. The absorption coefficient for PMMA at a photon energy of 16 keV with approximately $\mu_{\mathrm{PMMA}} = 1.174/\mathrm{cm}$ is chosen according to the NIST data base [37]. Likewise, the mass-

Table 5.4.: Simulated FLUKA mean dose rates $\dot{D}_{\mathrm{sim}}$ for the 16 keV and 40 keV photon beam and the three setups $S_{5\,\mathrm{PMMA}}$, $S_{10\,\mathrm{PMMA}}$ and $S_{0\,\mathrm{PMMA}}$. Assuming the standard deviation as the uncertainty on the average dose rates in the marked area.

	16 keV Photons		40 keV Photons	
Setup	$\dot{D}_{\mathrm{sim}}$ in Gy/s	$\dot{D}_{\mathrm{sim,\,max}}$ in Gy/s	$\dot{D}_{\mathrm{sim}}$ in Gy/s	$\dot{D}_{\mathrm{sim,\,max}}$ in Gy/s
$S_{5\,\mathrm{PMMA}}$	0.026 ± 0.015	0.050	0.330 ± 0.184	0.643
$S_{10\,\mathrm{PMMA}}$	0.016 ± 0.009	0.031	0.293 ± 0.160	0.575
$S_{0\,\mathrm{PMMA}}$	0.038 ± 0.023	0.076	0.341 ± 0.208	0.697

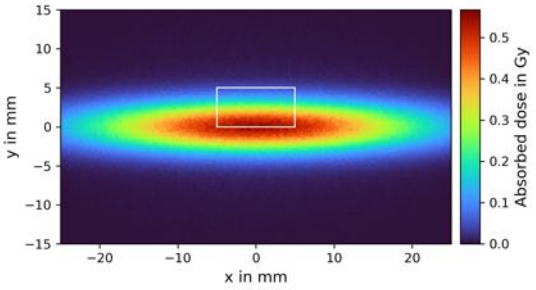

(a) Setup $S_{5\,\mathrm{PMMA}}$.

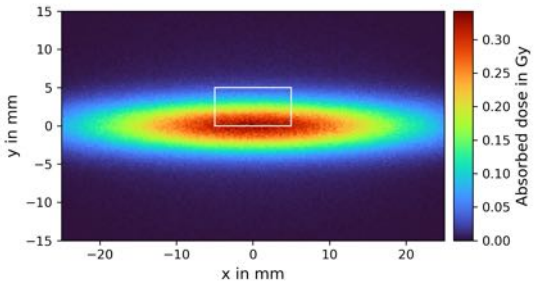

(b) Setup $S_{10\,\mathrm{PMMA}}$.

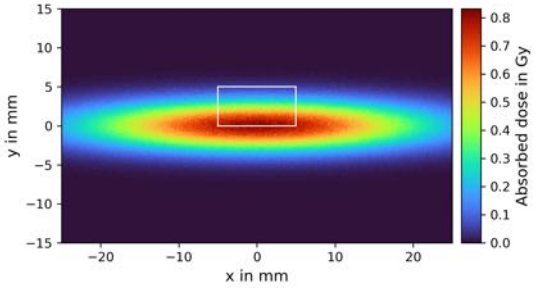

(c) Setup $S_{0\,\mathrm{PMMA}}$.

Figure 5.13.: Simulated 2D averaged absorbed dose profiles for a chosen irradiation time of $t = 11\,\mathrm{s}$ in relation to the shown measured profiles Figure 5.10 and the three introduced setups $S_{5\,\mathrm{PMMA}}$, $S_{10\,\mathrm{PMMA}}$ and $S_{0\,\mathrm{PMMA}}$. A linear behavior of the simulated dose is assumed here. Concerning a photon beam with Gaussian shape and an energy of 16 keV.

energy absorption coefficient $\mu_{\mathrm{en,\ A\text{-}150}} = 0.98\,\mathrm{g/cm^2}$ of the A-150 tissue-equivalent plastic material used for the EBT-XD films in the simulation was used to estimate again the expected dose rate at the position of the EBT-XD films. The mass-energy absorption coefficient of the material A-150 is therefore slightly smaller than that of water and will thus reduce the expected dose rate according to Equation (3.11). The maximal simulated dose rates differ from the analytically estimated ones by approximately 1.3 % to 34.8 %. It must be noted that Beer–Lambert law applies only to a point-like homogeneous photon beam which is no longer guaranteed after the interaction with the PMMA plates, which could possibly explain the larger deviation in contrast to the 1.3 % deviation in the case without PMMA plates. The high ratio F of the averaged simulated and measured dose rates values for each setup differs by an order of magnitude. This cannot be explained by statistical variations and must have other reasons, probably in the measurement procedure and analysis. To achieve more accurate results, it is necessary to optimize both the simulation and the experimental setup as well as the corresponding analysis. In addition to the red color channel, the green and blue channels could be integrated into the film dose analysis. Furthermore, as mentioned earlier, similar measurements could be conducted using films that are potentially better suited for the photon energy range of the IMAGE beamline, like the LD-V1 with a sensitive photon energy range of 20 keV to 200 keV. At the same time, the time measurement process and the sample holder would need to be optimized to enable a centered alignment of the films. Due to time constraints, the experiments could not be repeated.

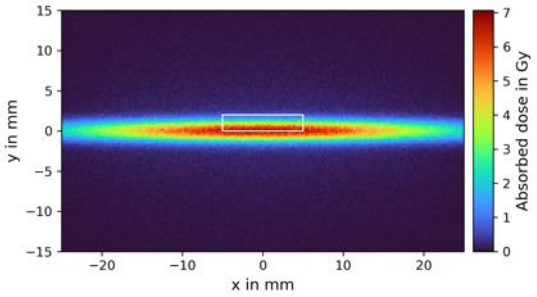

(a) Setup $S_{5\,\mathrm{PMMA}}$.

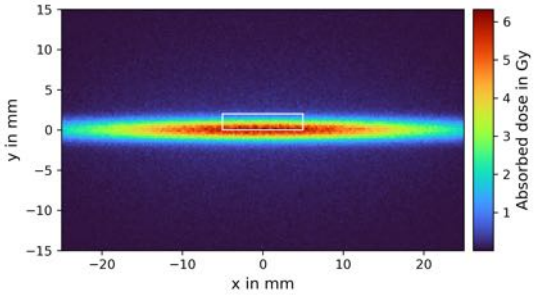

(b) Setup $S_{10\,\mathrm{PMMA}}$.

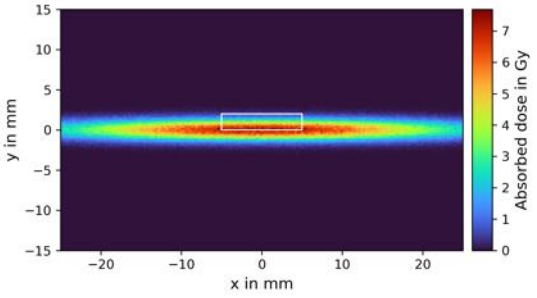

(c) Setup $S_{0\,\mathrm{PMMA}}$.

Figure 5.14.: Simulated 2D averaged absorbed dose profiles for a chosen irradiation time of $t = 11\,\mathrm{s}$ in relation to the shown measured profiles Figure 5.10 and the three introduced setups $S_{5\,\mathrm{PMMA}}$, $S_{10\,\mathrm{PMMA}}$ and $S_{0\,\mathrm{PMMA}}$. A linear behavior of the simulated dose is assumed here. Concerning a photon beam with Gaussian shape and an energy of 40 keV.

Table 5.5.: Comparison of the dose rates measurement $\dot{D}_{\mathrm{meas}}$ results, dose rates simulation $\dot{D}_{\mathrm{sim}}$ results, simulated maximal dose rate $\dot{D}_{\mathrm{sim,\,max}}$ and dose rates estimates $\dot{D}_{\mathrm{est}}$. In addition, the approximate ratio of measured to simulated dose rate $F = \dot{D}_{\mathrm{meas}}/\dot{D}_{\mathrm{sim}}$ is given.

Setup	$\dot{D}_{\mathrm{est}}$ in Gy/s	$\dot{D}_{\mathrm{sim,\,max}}$ in Gy/s	$\dot{D}_{\mathrm{sim}}$ in Gy/s	$\dot{D}_{\mathrm{meas}}$ in Gy/s	F
$S_{5\,\mathrm{PMMA}}$	0.042	0.050	0.03 ± 0.02	0.72 ± 0.02	24
$S_{10\,\mathrm{PMMA}}$	0.023	0.031	0.016 ± 0.009	0.35 ± 0.04	22
$S_{0\,\mathrm{PMMA}}$	0.075	0.076	0.04 ± 0.02	1.7 ± 0.1	43

6. Biological Methods and Pre-Tests

After characterizing the dose profiles of the IBPT accelerators FLUTE and KARA through simulations and dosimetry experiments using phantoms, irradiation experiments are planned to be conducted in the field of cancer research regarding radiation therapy.
Unlike medical accelerators, horizontal irradiation is currently not possible at the IMAGE beamline of KARA and at FLUTE. To solve this, the following biological cell routines for cell preparation will be explained and a possible method for a vertical mounting of biological samples, specifically cancer cells, will be presented.

6.1. Cell Culture

As part of the collaboration with the DKFZ, the following cell experiments were conducted using the H460 cell line. H460 cells are cancer cells of a cell line consisting of immortalized adherent human lung cancer cells. DKFZ already possesses various irradiation data for this cell line and has extensive knowledge about these cancer cells. A comparison of irradiation efficiency with future irradiation experiments at KIT is therefore suitable. Because of this, the H460 cell line was imported to KIT from DKFZ.
To familiarize with the biological methods, some experiments were conducted using the HepG2 cell line, which is also an immortalized human cancer cell line, specifically liver cancer cells. This cell line is commonly used at the IFG at KIT for various research purposes. Identical experiments are carried out later with the H460 cell line.

For cultivation, $75\,\mathrm{mm}^2$ flasks are used and stored in a standard cell culture incubator at $37\,^{\circ}\mathrm{C}$ with $5\,\%$ CO_2 content. A medium change, which also involves cell splitting (Section A.1), is performed twice a week. For this purpose, DPBS (Dulbecco's Phosphate Buffered Saline) is used for washing the cells, and Trypsin-EDTA is used to detach the adherent cells from the flask surface. A combination of DMEM (Dulbecco's Modified Eagle Medium), FCS (Fetal Calf Serum) and PIS (Penicillin-Streptomycin) is used as the culturing medium for both cell lines. Cell splitting and medium change ensure the nutrient supply to the cancer cells and reduce the accumulation of harmful metabolic waste products. Additionally, dead cells which are not required for the experiments and could affect the results are removed.

6.1.1. Cell Counting

For cell experiments, it is important to have a rough overview over the cell numbers. Depending on the experiment, different cell numbers are more suitable for the respective purpose.
To determine the cell concentration c_S of a flask before performing the actual experiments, a so-called Bürker or Neubauer counting chamber is used, see Figure 6.1. To determine the cell concentration, $10\,\mu\mathrm{l}$ of the cell suspension, for example during the splitting process, are placed on the counting chamber at the sample position (Figure 6.1, top left). Under the

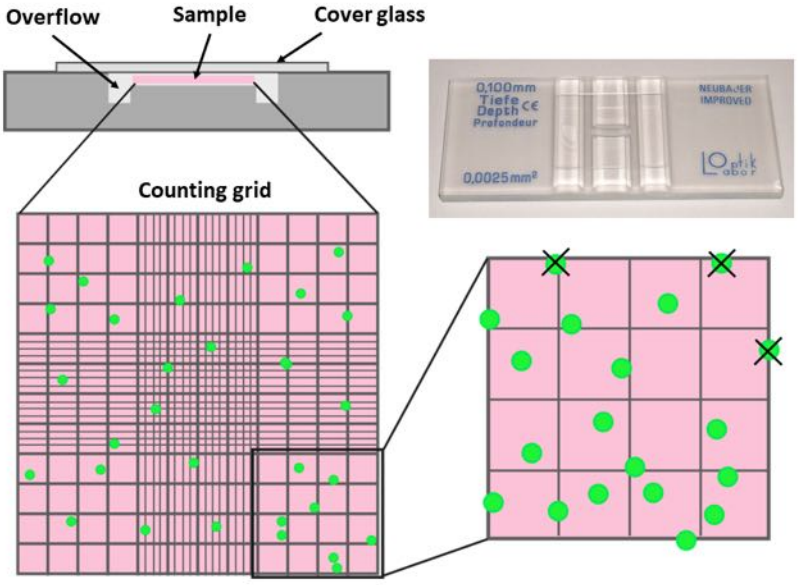

Figure 6.1.: Counting chamber: example layout (Neubauer Improved). Schematic side view and counting grid with counting example. Cells are represented through green dots. Crossed out cells are not counted.

microscope, the respective cell numbers N_i are determined for several ($n \approx 4$) independent 4×4 squares, and then the mean cell number $\overline{N}$ is calculated according to

$$\overline{N} = \frac{1}{n} \sum_{i=0}^{n} N_i. \tag{6.1}$$

The stock solution cell suspension concentration c_S is then given by

$$c_S = \overline{N} \cdot (V_{\text{chamber}})^{-1} = \overline{N} \cdot 10^4 \, \frac{\text{cells}}{\text{ml}}, \tag{6.2}$$

since each square of the counting chamber has a volume of $V_{\text{chamber}} = 0.1\,\text{mm} = 0.1\,\mu\text{l} = 10^{-4}\,\text{ml}$. After determining the cell count, the desired cell dilutions can be prepared with the concentration c_V. To calculate the volume of the stock cell suspension V_S which is required for the dilution to achieve the concentration c_V in the final volume V_V, the relationship

$$c_S \cdot V_S = c_V \cdot V_V \tag{6.3}$$

is used. In this case, it is utilized that the amount of substance n_S in the stock solution, which corresponds to the cell count, is equal to the amount of substance n_V in the dilution. By using the general definition of amount of substance $n = c \cdot V$, we can derive Equation (6.3). The volume of cell suspension required for the dilution can be calculated after a small rearrangement of Equation (6.3), corresponding to

$$V_S = \frac{c_V \cdot V_V}{c_S}. \tag{6.4}$$

The required volume of medium V_M to achieve the desired dilution concentration is at last given by the volume difference $V_M = \Delta V = V_V - V_S$. As already mentioned, the dilution concentration and the desired dilution volume should be chosen based on the specific experiment. Some buffer volume, usually 10 % to 20 % of the required solution, has been included to compensate losses during pipetting. In certain experiments such as the investigation of spheroid formation (Section 6.3) whole dilution series are used.

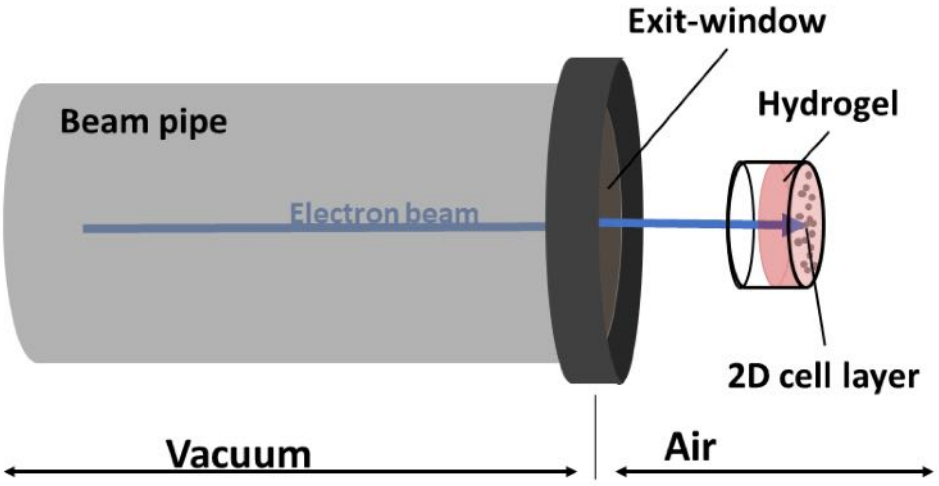

Figure 6.2.: Schematic cell irradiation setup (side view) with vertical mounting of a 2D cell sample using hydrogels, marked in pink. The electron beam is represented as a blue arrow coming from left without a beam expansion.

6.2. Hydrogel

To enable vertical irradiation of cancer cells, there is the possibility to use so-called hydrogels. Hydrogels are originally developed for 3D bioprinting as a bioink. They are hydrophilic polymeric materials which can store a large amount of water due to their polymer structure. The resulting gel resembles the extracellular matrix (ECM) due to stability and water content and can therefore be used as a kind of artificial ECM. Their porous structure ensures a sufficient supply of cells in and under hydrogels [20].
In addition to the commonly used semi-synthetic gelatin-based hydrogel polymer GelMA (gelatin methacryloyl), the hydrogel polymers GelN and GelS developed at IFG could be used as well [56]. The gel-like consistency of the hydrogels allows the vertical mounting of the cell samples, see a schematic representation in Figure 6.2. They can protect the cells and prevent them from drying out during the vertical irradiation. Using the normal cell medium during the irradiation as usual would be very difficult due to the water-like consistency and gravity. A general compatibility of hydrogel has already been proven, see [56]. In the context of this thesis, additional hydrogel compatibility tests for the H460 cell line are carried out. As part of the compatibility tests conducted in this work, GelMA hydrogel was typically used. To assess the bio-compatibility of the hydrogel with the H460 cell line, the cells are coated with the hydrogel followed by a live-dead staining. The compatibility tests for the H460 cell line will be explained in more detail in the next section.

(a) H460 coated with hydrogel, after gel hardening. Control group coated with culture medium.

(b) Hydrogels are coated with culture medium (color indicator shows nutrient content: pink color = good nutrient content, yellow like color = less nutrients, medium change is required).

Figure 6.3.: Ibidi Slide with GelMA and HepG2 during a compatibility test. Left to right: GelMA high, GelMA medium, GelMA low, control group.

6.2.1. H460-Hydrogel Bio-Compatibility Tests

For the hydrogel biocompatibility test, the following materials are required in addition to the cultured H460 cells:

- Culture medium (DMEM)
- DPBS
- Trypsin-EDTA
- Flask, Eppendorf Tubes
- Ibidi Slide (Figure 6.3)
- Hydrogel base (GelMA, GelN, GelS)
- LAP (10 %)
- Omnicure S2000
- Live-dead staining kit; calcein AM + propidium iodide (PI)
- Microscope

During the regular splitting process, the cell concentration is determined using a Neubauer counting chamber. In the case of adherent H460 cells, a dilution with a concentration of $c_V = 10^5$ cells/ml is prepared from the cell suspension. Subsequently, 200 µl of the diluted cell suspension is added to each of the eight wells of an Ibidi slide and incubated for one day in the incubator. The cells will attach and grow in the well. The next day, the hydrogels are prepared. For this purpose, appropriate amounts of hydrogel polymer (high, medium or low), photoinitiator (LAP), and DPBS are mixed together. For two wells of the Ibidi slide, prepare 500 µl of hydrogel, consisting of 250 µl of GelMA (10 %), 15 µl of LAP (10 %), and 235 µl of DPBS. The medium is removed from the wells apart from the two control groups wells, and then 200 µl of the mixed hydrogel is added to each well of the Ibidi slide containing the cells (Figure 6.3a). The still liquid gels are hardened for 30 s at 500 mW under the Omnicure S2000. The UV light emitted by the photoinitiator triggers the polymerization process, resulting in gel hardening. For further nutrient supply, each well is then topped up with 200 µl of culture medium (Figure 6.3b). A medium change is performed every two days during the culturing period. For the H460 compatibility test, an Ibidi slide consisting of eight wells is prepared, with two wells for each of the following groups: H460 under hydrogel high, hydrogel medium, hydrogel low and the control group (no hydrogel), see Figure 6.3a. After the gels have hardened, the next step could involve irradiating the cells (day zero).
For the biocompatibility test, a live-dead assay is performed without irradiation. Therefore the rows of the Ibidi slide are stained with calcein AM and PI. The first row of the Ibidi

slide is tested for cell viability on the following day, day one of the experiment, and the second row is tested on day seven.

For the live-dead staining, the old medium in the wells to be stained is removed carefully to avoid disturbing the hydrogel. Next, for cell staining, 249 µl of medium is mixed with 1 µl of calcein AM and 2.5 µl of PI. Then, 200 µl of the staining solution is added to each well and incubated for 20 to 30 minutes until a subsequent medium change is performed. Within the control group, the medium change takes place after approximately five minutes since there is no diffusion through the hydrogel, and a 20 to 30 minutes exposure to PI proves to be toxic to the H460 cells Section D.

Both the control group and the cells under different strength hydrogels are stained with calcein AM and PI. The condition of the cells can be observed using a fluorescence microscope. Living cells will appear green due to calcein AM staining, while dead cells will exhibit red fluorescence from PI. The corresponding results after one day under the hydrogel are shown in Figure 6.4a to 6.4d. Overall, there is no significant difference in the survival rate of H460 cells observed between the different images. The hydrogels appear to have no toxic effects and demonstrate bio-compatibility for at least one day.

The second row on the seventh day of the experiment also shows no increased cell death compared to the control group (Figure 6.4e to 6.4h), indicating that the hydrogels are suitable in terms of utility and bio-compatibility. A clear cell reproduction from day one to day seven can be seen. Due to the fact that the hydrogels retain nutrients and humidity, they ensure that the cancer cells are in an environment that is well suited to them. Hydrogels can thus enable that during an irradiation process, the cells will be not damaged or even die due to unfavorable environmental influences. This allows a vertical montage for a possible cell irradiation for example at the research accelerators FLUTE and KARA. At the same time the hydrogels are nearly water equivalent and therefore form a good basis for comparison to the irradiation experiments at the DKFZ.

It should be noted that GelMA low and GelMA medium show significant degradation on the seventh day. While GelMA low already exhibited degradation on the first day, GelMA high is really stable in consistency. Therefore, considering the generally more stable structure of GelMA high, GelMA high is likely the most suitable for subsequent vertical irradiation tests.

6.3. Spheroids

With the help of hydrogels, it is possible to achieve vertical cell irradiation at KIT's accelerators as already mentioned. In addition to the 2D cell structure irradiation described in the previous section where the cells cover the bottom of the respective slide and are protected from drying out by the hydrogel, another test was conducted to generate specific 3D cell structures for the H460 cell line, called spheroids. Spheroids are spherical cell aggregates that form spontaneously on agarose-coated surfaces due to the non-adhesive properties of agarose. The ability of H460 cells to form spheroids is investigated in the following.

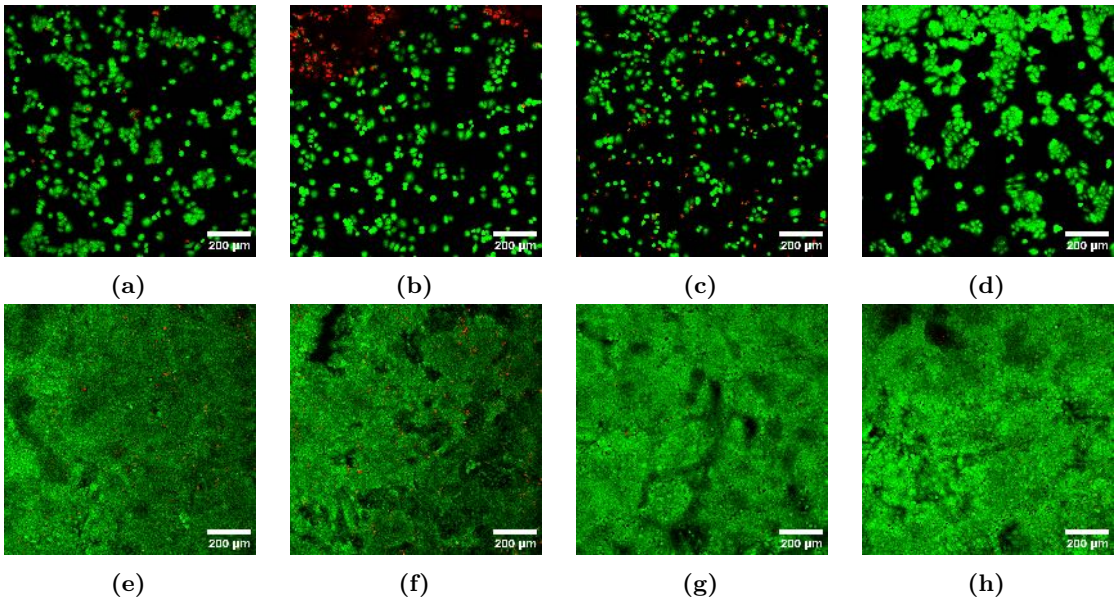

Figure 6.4.: Live-dead staining of H460 (10^5 cells/ml) with calcein AM (green) and PI (red) in GelMA at day one ((a)-(d)) and day seven ((e)-(h)) in the sequence GelMA high, medium, low and control group. Evaluation with covocal fluorescence microscopy (Leica Stellaris 5, green: excitation 494 nm, emission 499 nm to 544 nm; red: 549 nm, emission 591 nm to 725 nm). Contrast adjustment, merging of red and green color channels and scale bar generation with ImageJ. Scale 200 nm.

6.3.1. H460 Spheroid Formation Test

To generate the spheroids, the following materials are required in addition to the cultured H460 cells:

- Culture medium (DMEM)
- DPBS
- Trypsin-EDTA
- Flask, Eppendorf Tubes
- Agarose
- Glass bottle and steril plastic dish
- Microwave
- 96-well plate
- Multichannel pipette

In the first step, a 1.5 % agarose solution is prepared. In order to prepare the solution, 1.5 g of agarose is weighed in a sterile 250 ml glass bottle and then filled with 100 ml of sterile DPBS under the sterile hood. The agarose in DPBS is then dissolved by heating it in the microwave for approximately 1.5 minutes with the lid slightly opened.
The prepared agarose solution is then used to fill a 96-well plate for spheroid cultivation. For this purpose, a portion of the agarose solution is poured into a sterile plastic dish. Then, using a multichannel pipette, each well of the 96-well plate is filled with 50 ml of the agarose solution. The 96-well plate needs to cool down for approximately 15 min until the agarose solidifies. After the preparation of the agarose plate, the generation of spheroids in the 96-well plate can begin.
To begin with, the cultured H460 cells are washed with DPBS, trypsinized, and brought into

Table 6.1.: Dilution series for spheroids with cell counts of 1000 to 5000.

cell count per spheroid (in 40 ml)	cell concentration per ml	total volume in ml	dilution from	volume cell suspension in ml	volume medium in ml
5000	125 000	4	stock solution		
4000	100 000	2.5	5000-solution	2	0.5
3000	75 000	1	5000-solution	0.6	0.4
2000	50 000	3	4000-solution	1.5	1.5
1000	25 000	3	2000-solution	1.5	1.5

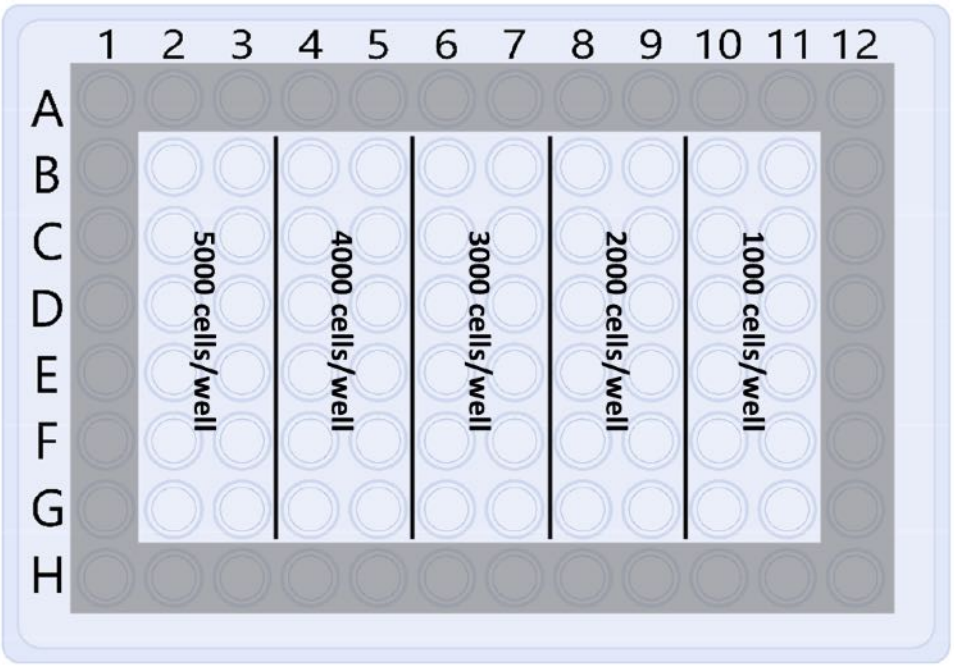

Figure 6.5.: Template with example cell concentrations of a 96-well plate for spheroid generation on agarose. Edited template taken from [57].

suspension. Subsequently, the cell count is determined using a Neubauer counting chamber as explained before. A 4 ml stock solution with a cell concentration of $c_S = 125 \cdot 10^3$ cells/ml is prepared, from which a dilution series is set up, calculated using Equation (6.3). The calculation of the dilution series is presented in Table 6.1. After preparing the dilution series, the outer wells of the 96-well plate are filled with DPBS to prevent evaporation of the medium. From the remaining 60 wells, 12 of them are always filled with the same cell solution. A volume of 40 ml of the solution is added to each well. After seeding all the cell solutions, the plate is incubated at 37 °C with 5 % CO_2. The medium is refreshed every second and third day by adding 10 ml to 15 ml of fresh medium. The layout of a corresponding agarose plate is shown in Figure 6.5.

After two days, the first spheroids with different sizes, scaling with the initial cell number per well, can be observed under the microscope, cf. Figure 6.6a to 6.6c. After approximately six days, the spheroids have grown again and are much darker than before, cf. Figure 6.6d to 6.6f. This indicates a grater depth. The results of the H460 spheroids formation test are shown in Figure 6.6.

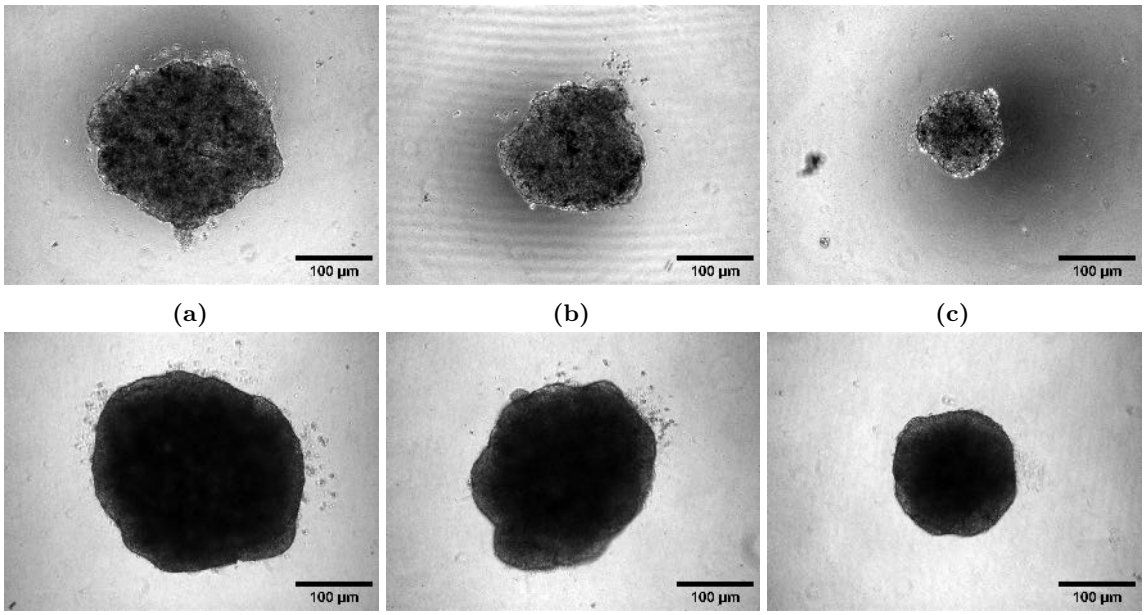

Figure 6.6.: H460 spheroids. Spheroids after one day (upper row (a)-(c)) and after six days (lower row (d)-(f)). Images taken using a Leica DMIL LED wide-field microscope. Contrast adjustment and scale bar generation with ImageJ. Scale 100 µm.

The H460 cell line is capable of forming spheroids using the standard agarose procedure for spheroid generation. These spheroids can be further utilized for future 3D cell irradiation experiments and compared with equivalent 2D cell irradiation experiments. This comparison may provide insights into the success of radiation therapy based on cell or tumor geometry.

After the irradiation, various analysis techniques are applied to quantify the effects of radiation on cancer cells. These techniques may include a clonogenic cell survival assay [58] to determine the growth rate of the irradiated cells or a FACS (Fluorescence Activated Cell Sorting) analysis [59] to determine the cell cycle phase of the cells. These and other methods provide important data and insights into the response of cancer cells to the specific irradiation treatment, allowing predictions of the success of such radiation therapies.

7. Summary and Outlook

Establishing medical physics at the Institute for Beam Physics and Technology (IBPT) opens up a very broad and important field of research for scientists and engineers of various disciplines whereby the success in this field depends significantly on collaborating.
In the context of the cooperation between DKFZ and KIT, first proof-of-principle radiological and biological experiments concerning the integration of radiotherapeutic cancer research at the IBPT accelerators FLUTE and KARA were presented in this work. To validate and optimize the experiments, FLUKA simulations have been carried out and various Python programs for the evaluation of the simulation data were implemented.

First electron dose measurements were done at the low-energy section of FLUTE, reaching electron energies up to 7 MeV. A water phantom consisting of water-equivalent RW3 material and the Roos Chamber from PTW, as a dose detector, were used to perform depth dose curve measurements at FLUTE. A maximum dose rate of about 0.2 Gy/s was measured at a depth of about 2 mm with a bunch charge of about 348 pC and an average total electron energy of 4.87 MeV. To verify the first results, additional analytical estimations as well as dose simulations carried out with FLUKA were performed in accordance with the measurement. Here, maximum dose rates up to 2 Gy/s at a depth of 2 mm for a 150 µm carbon or Mylar window are obtained for the corresponding measurement setup. In the case of a 150 µm stainless steel exit window in the same depth, experiment and simulation ($\approx$ 1.75 Gy/s) thus differ by almost a factor of nine, where simulation and analytical estimation differ by only 1.7 %, which is due to the neglect of the window in the estimation. A possible explanation for the strong discrepancy between simulation and measurement could be the used detector, since it was not developed for short pulsed electron radiation as a consultation with the manufacturer has shown. It must be assumed that the detector is saturated due to the high maximum dose rates per pulse ($\approx$ 40 mGy/s), which is a factor of 40 higher than the maximal dose per pulse specified in the detector data sheet. Further dose measurements, for example with film dosimeters like radiochromic films, can be carried out in addition and used as a comparison. At the same time, it is possible to correct the measured dose by different dose correction factors with respect to pulsed radiation and conditions prevailing away from the standard dosimetric conditions [11] in order to obtain a more accurate result. Further systematic investigations are necessary for this purpose.
Another challenge of dose measurements is the transition between the accelerator vacuum and the ambient air where the irradiation sample is located. The exit window used for separation needs to be as thin as possible to mitigate its influence on the beam, but as robust as possible to withstand the pressure difference. Different materials such as stainless steel, carbon, titanium, Kapton and Havar were studied and systematically compared with respect to the resulting depth dose curves and the energy loss occurring during the passing of the window. The maximum achievable dose depends on the thickness and material of the window. The different energy loss of the electrons is mainly caused by the density of the window materials since the respective mass stopping powers are almost identical in the

present electron energy range. A systematic comparison shows that regarding mechanical stability, the materials Havar and stainless steel are the most promising candidates according to mechanical analysis. In general, the electron beam is scattered by the exit window which greatly reduces the dose rate. For an optimized dose rate on the other hand, diamond seems to be the most promising as a window material. Here, the lowest scattering of the electron beam occurs due to its low density. The high tensile strength of diamond would allow a very thin window.

For the determination of the photon dose rate in the X-ray range at the electron synchrotron KARA, first measurements with the radiochromic films of the company Gafchromic were done. A first test measurement of the reaction of the EBT-XD films to the synchrotron radiation was carried out under vacuum conditions in the LIGA I beamline. This showed a clear response of the films to the photon radiation and the structure of the used mask was clearly visible. Since the LIGA beamline is not suitable for subsequent cell experiments due to the vacuum conditions, follow-up irradiations of the EBT-XD films took place in the IMAGE beamline. Here, experiments could be performed at ambient air, suitable for future experiments with cells. Three irradiation setups were tested to characterize the dose rate, based on irradiation experiments with the MultiRad225 carried out at DKFZ. The dose rate for the synchrotron radiation produced by the CLIC Wiggler and filtered at 16 keV by a monochromator was measured to be 0.72 Gy/s for an irradiation of the films in case of setup $S_{5\,\mathrm{PMMA}}$ and 0.35 Gy/s in the case of setup $S_{10\,\mathrm{PMMA}}$. Both setups consist of films between PMMA plates as a water phantom substitute. For setup $S_{0\,\mathrm{PMMA}}$, the dose rate was measured to be 1.7 Gy/s in the case of film irradiation without PMMA plates. The analysis of the film measurements was performed using Python and the available image processing libraries.
Analogous simulations with the FLUKA code yield dose rates of 0.026 Gy/s, 0.016 Gy/s and 0.038 Gy/s for the respective setups. Here, experiment and simulation deviate by about a factor of 22 to 43. Reasons for this could be the used EBT-XD films. According to the manufacturer, they are not suitable for a photon energy of 16 keV (photon energies over 100 keV are required). They propose the usage of the laminated LD-V1 films, which are supposed to be suitable for photons in the energy interval 20 keV to 200 keV. However, due to time constraints, it was decided to use the EBT-XD films and acquired calibration data provided by DKFZ for the first irradiation tests and in order to test the experimental procedure on the beamlines. Analytical estimates again agree with the simulation values. At the same time, the error could lie in the vague time measurement procedure, which could be optimized, and the evaluation process just taking the red color channel of the film scans into account. An optimization can be done by using all three (red, green, blue) color channels and performing new calibration measurements. For example, the calibration data at DKFZ were recorded with photon energies up to 225 keV, so new calibration measurements with lowered photon energy for the EBT-XD and the LD-V1 would be necessary for better comparability and error minimization. In the future, this can lead to an optimized dose determination procedure.

The last part of the work takes a look at the biology, testing the possibility of how to solve the vertical assembly challenge of the cells for irradiation. The biocompatibility of hydrogels, especially GelMA, was tested with respect to the H460 cell line. Live-dead staining using Calcein AM and PI was used to demonstrate that H460 cell line is biocompatible with the hydrogel. Vertical sample mounting through the use of the gels is therefore possible. In addition, the formation of spheroids of cell line H460 was tested. These can be grown without problems by means of an agarose plate and used, for example, for 3D irradiation studies. These studies can then be compared to 2D irradiation studies carried out by the lab group E041 at DKFZ in order to investigate the influence of 3D cell arrangement on the irradiation success.

Outlook

The large discrepancy between the simulation and the measurement results of both accelerators could not be explained within this thesis due to limited time. Therefore, more measurements as well as more optimized simulations, regarding setup and material details, are needed. At the same time, it is necessary to test the used detectors and to improve the implemented evaluation programs.
In the case of FLUTE, the first step is to integrate a suitable exit window into the system. For this purpose, a design by Steffen Schott has already been prepared and Havar as well as stainless steel foils in various thicknesses have been ordered. As soon as all parts are made, these foils can be tested independent of FLUTE to pressure loads of 1 bar in an external setup. Once a suitable window has been determined and the upgrade of FLUTE has been completed, new depth dose curves can be recorded and compared to simulations. For this purpose, both the Ross Chamber as well as the Advanced Markus Chamber from PTW can be used as detectors to compare. Additionally, measurements could also be done with a new ionization chamber by PTW that was especially developed for pulsed high-energy radiation. A charge scan could reveal a possible saturation of the chambers and should be compared with simulations. Furthermore, radiochromic films like EBT-XD and HD-V2 from Gafchromic could be tested. They will simultaneously provide the dose as well as a spatial profile of the dose providing complementary information.
Before the FLUTE upgrade, the old photoinjector generated a high dark current in addition to the laser-induced bunch charge. This dark current will be very small after the upgrade due to the new cathode. The then generated dose will be purely due to the bunch charge. In total, after the upgrade, bunch charges of up to 1 nC at a repetition rate of 10 Hz are planned. Thus, according to the estimation carried out in Section 4.3, an average dose rate of about 10 Gy/s could theoretically be possible. At a later upgrade, it might even be possible to increase the repetition rate of FLUTE to 50 Hz so that a dose rate of 50 Gy/s in the low energy section could be achievable. This could provide the opportunity to explore the FLASH effect, which requires dose rates of more than 40 Gy/s.
Once the LINAC and bunch compressor are connected in later phases of the project, appropriate film detector calibration and depth dose curve measurements should be performed for subsequent dose measurements as in the low-energy section. The enlarged parameter range with energies up to 90 MeV provides further potential for testing new irradiation methods.
In the case of KARA, to verify the measurement results of the 16 keV beam of the IMAGE beamline, dose measurements could be performed again with an improved setup (precise sample holder, water-equivalent plates etc.) using LD-V1 films from Gafchromic. These unlaminated radiochromic films, according to the manufacturer, should be better suited for the photon energy range provided by IMAGE. Dose measurements with other dose detectors like ionization chambers, e.g. the Ross Chamber from PTW, which is already used by the DKFZ for photon dose measurements, should as well be done as a validation to the film dose measurements. At the same time, identical measurements can be performed for the 40 keV photon beam. All measurements should again be cross-checked with FLUKA simulations. The python evaluation program could be optimized by implementing all three color channels into the evaluation process to obtain a more precise calibration curve and final film dose result.
Subsequently, possible MicroBeam/MiniBeam setups with corresponding collimators and masks for pattern generation could be tested and compared with existing studies of the DKFZ. For this purpose, it would be possible to generate and test different spatial irradiation patterns according to the masks of the LIGA 1 beamline.

After the complete dose characterization of both accelerators with corresponding phantom irradiation, systematic irradiation studies with cancer cells can be performed in later project

phases to investigate and improve cancer radiotherapy. These can initially take place with the H460 cells, as they have been well studied by the DKFZ, and can later be transferred to other cell lines with a possibly slightly different setup depending on the cell type. Possible feasible studies could therefore be FLASH studies as well as MicroBeam and MiniBeam studies or other irradiation methods, first based on the usual 2D cell structure and later, for example, on 3D structures such as spheroids. In a further step, cell 3D printing offers the possibility to specifically place cancer cells next to healthy cells which would allow a direct comparison of radiation damage to healthy tissue and tumor control to be tested. There would also be the possibility to test different irradiation configurations in combination with chemical additives. At the same time, studies related to the high peak dose rates of research accelerators could be conducted to test and explore dose detectors with respect to this use, as well as to investigate the possible biological impact of high peak dose rates.

In conclusion, a wide range of possibilities to investigate and improve radiation therapy methods are available at the FLUTE and KARA research accelerators due to a very flexible choice of beam parameters. With the help of future systematic radiation experiments and studies performed in the context of cancer research, important information can be obtained about the effectiveness of the radiation therapy used. In this way, new radiation methods can be developed and researched to further optimize the existing cancer treatment methods and reduce cancer mortality.

Appendix

A. Protocols

A.1. Cell Splitting - Adherent Cells (here H460)

Materials:

- Phosphate-buffered saline (PBS) → washing the cells
- Tripsin (enzyme) → cells dissociate from the flask surface
- Cell culture media
- 2 new flasks (labeling: initials|cell line|passage|date)
- Pipettes (5×10 ml, 2×5 ml)
- 3 centrifuge tubes (Falcons)
- Waste container

Protocol:

1. Warm up media, PBS, Trypsin
2. Start the biological safety cabinet
3. Clean the cabinet and all utilities with ethanol before placing them under the biological safety cabinet
4. Remove the old media (10 ml)
5. Wash the adherent cells with PBS (10 ml) - on the side without cells, not directly on the cells, carefully!
6. Remove PBS, use it as a counterpoise later
7. Add 3 ml Trypsin
8. Put the flask in an incubator for ≈ 5 min
9. Add 7 ml cell culture media (total 10 ml)
10. Transfer cell suspension in an empty centrifuge tube (Falcon)
11. Centrifuge the cell suspension for 4 min at 1200 rpm, at 20 °C
    → cells $\widehat{=}$ precipitate (pallet), milky white
12. Decantation of the supernatant (remaining liquid)
13. Add 10 ml media to the empty new flask
14. Mix the pallet with 10 ml media
15. Put 1 ml to 1.5 ml of the cell suspension in the new flask
16. Incubate in a 37 °C and 5 % CO_2 incubator

B. Uncertainty Consideration

The uncertainty considerations in the following section are based on [60].

Every measurement of a physical quantity is affected by an unavoidable measurement uncertainty. These can be of statistical nature and can be minimized by repeating the measurement. Uncertainties of a systematic nature, which are due to the inaccuracies of the measuring instruments used, cannot be minimized by repetitions, in contrast to statistical uncertainties, but can be minimized, for example, by more accurate measuring instruments. To estimate the reliability of a measured quantity, some uncertainty considerations are performed as described below. For the representation of the measurement results x the following form is used in this work:

$$(\text{value of } x) = x_{\text{best}} \pm \delta x, \tag{B.1}$$

where $x_{\text{best}} = (\text{best estimate for } x)$ and $\delta x = (\text{uncertainty in the measurement})$.

When a measurement is repeated several times N, the mean $\overline{x}$ of all measured values x_i normally turns out to be the best estimate x_{best} of the sought quantity x. The mean $\overline{x}$ is calculated as follows:

$$x_{\text{best}} = \overline{x} = \frac{1}{N}\sum_{i=1}^{N} x_i. \tag{B.2}$$

One measure of the average uncertainty of the measured value is the standard deviation σ_x, defined as

$$\sigma_x = \sqrt{\frac{1}{N}\sum_{i=1}^{N}(x_i - \overline{x})} = \delta x. \tag{B.3}$$

This corresponds to the default standard deviation of the `numpy.std()` function [61] that is used in this work.

For the determination of further quantities $q(x_k)$ dependent on the measured quantities x_k with uncertainties δx_k, it is assumed in the simplest case that the measured input quantities x_k are uncorrelated, i.e. have no statistical dependence. If this is true, the uncertainty in q can be calculated according to

$$\delta q = \sqrt{\sum_{k=1}^{n}\left(\frac{\partial q}{\partial x_k}\cdot \delta x_k\right)^2}. \tag{B.4}$$

C. Roos Chamber Parameters

Table C.1.: Ion collection efficiency at nominal voltage and sensitive volume parameters of the Ross Chamber from PTW used in the depth dose measurement with the DKFZ. Further parameters can be looked up in the in the catalog of PTW.

Parameter	Value
Ion collection time	125 µs
Max. dose rate for $\geq 99.0\,\%$ saturation	10.4 Gy/s
Max. dose per pulse for $\geq 99.0\,\%$ saturation	0.93 mGy
Sensitive volume radius	7.8 mm
Sensitive volume depth	2 mm

D. H460-Hydrogel Bio-Compatibility Tests - PI Exposure Time of 20 to 30 Minutes

Figure D.1 shows the live-dead staining of H460 cells after a 20 min to 30 min exposure time to the fluorescent markers PI and calcein AM. While no cell survived in the control group, no increased mortality rate is shown in the hydrogel-coated cells. Consequently, the hydrogel has no harmful effect on the cells and seems to additionally protect them from the toxic properties of PI in this case.

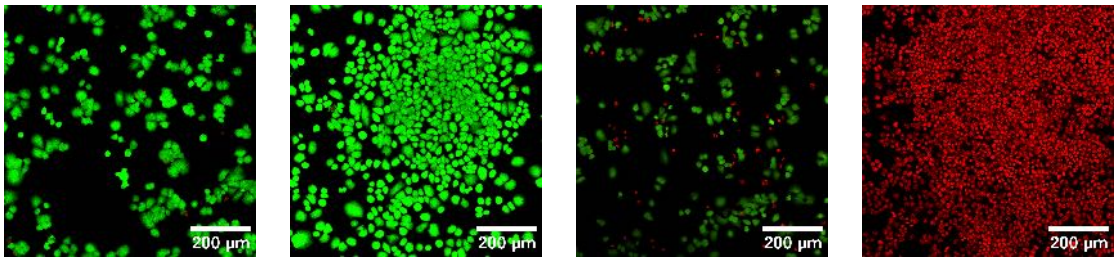

(a) **(b)** **(c)** **(d)**

Figure D.1.: Live-dead staining of H460 (10^5 cells/ml) with calcein AM (green) and PI (red) in GelMA at day one ((a)-(d)) in the sequence GelMA high, medium, low and control group. Evaluation with covocal fluorescence microscopy (Leica Stellaris 5, green: excitation 494 nm, emission 499 nm to 544 nm; red: 549 nm, emission 591 nm to 725 nm). Contrast adjustment, merging of red and green color channels and scale bar generation with ImageJ. Scale 200 nm. PI exposure time of 20 min to 30 min.

E. FLUKA - Depth Dose Curves and Room Dose Profiles

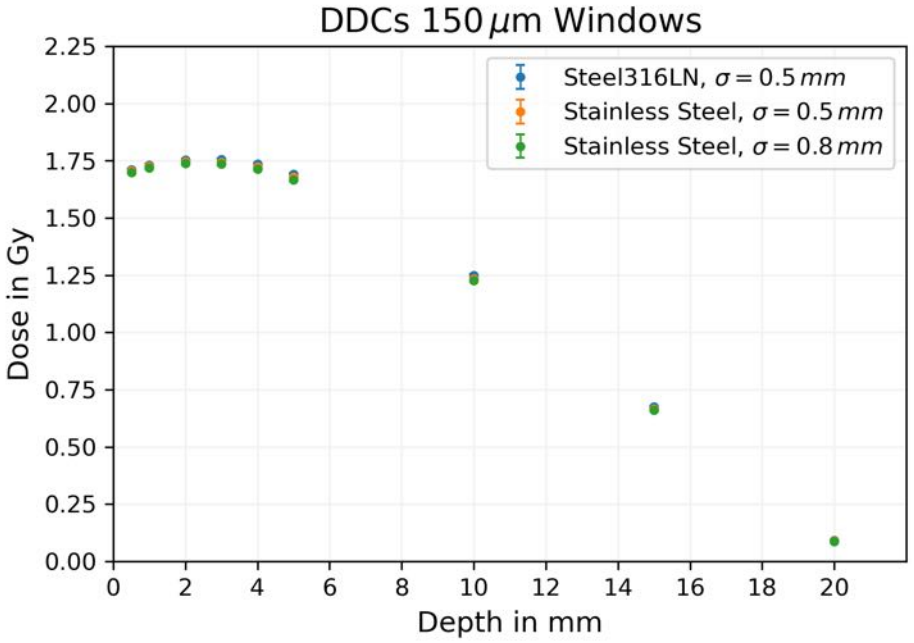

Figure E.2.: Simulated electron depth dose curves of two types of 150 µm stainless steel windows with an density difference of $\Delta\rho = 0.2\,\mathrm{g/cm^3}$ and two different σ beam sizes. Assuming five bunches per second over one second with a bunch charge of 348 pC.

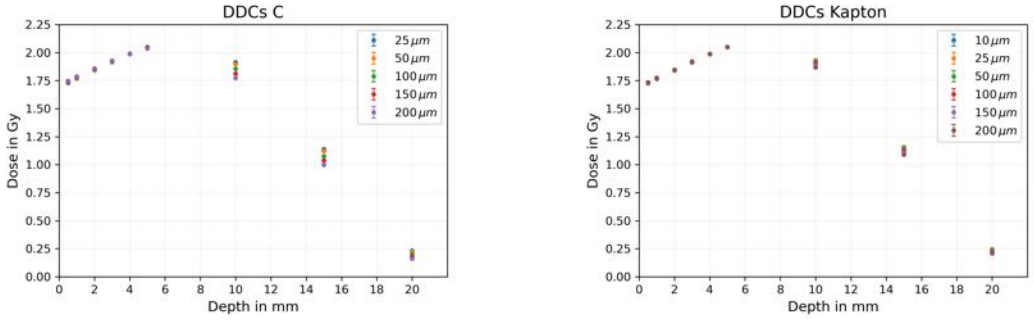

Figure E.3.: Simulated electron depth dose curves for diamond (left) and Kapton (right) windows for various window thicknesses. Assuming 5 bunches per second over one second with a bunch charge of 348 pC. Assuming position of the sensitive volume as exact. The statistical uncertainty calculated by FLUKA on the dose value per bin is less than 2%, so the absolute error is of the order of 10^{-3} and therefore not visible in the plot.

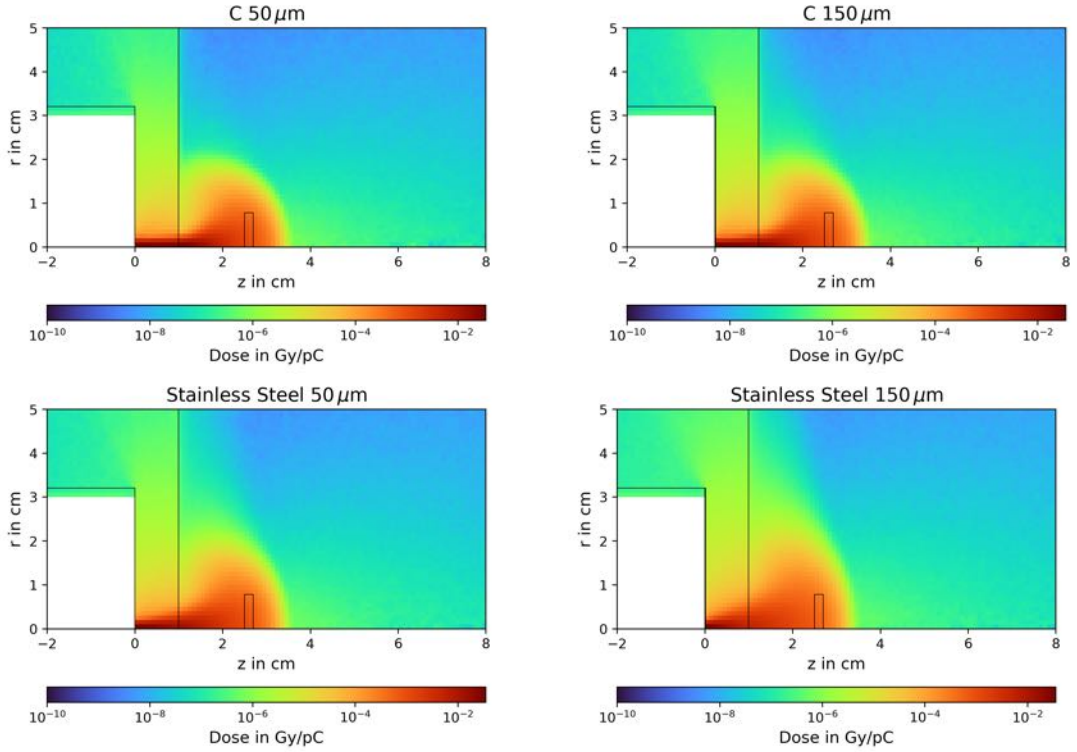

Figure E.4.: 2D absorbed dose plot per charge (side view) in logarithmic scale assuming rotational symmetry around the z-axis for diamond and stainless steel of wide 50 µm and 200 µm. Accelerator beam pipe, water phantom, and imitated Roos Chamber are marked separately. No dose deposition takes place inside the beam pipe under vacuum conditions as shown in white.

Bibliography

[1] Deutsche Krebsgesellschaft. *ONKO INTERNETPORTAL - Therapieformen bei Krebs*. 2023. URL: https://www.krebsgesellschaft.de/basis-informationen-krebs/therapieformen.html (visited on 04/26/2023).

[2] International Agency for Research on Cancer. *Estimated number of new cases from 2020 to 2040, Males and Females, age 0 to 85+, World*. 2023. URL: https://gco.iarc.fr/ (visited on 05/25/2023).

[3] Rolf Sauer. *Strahlentherapie und Onkologie*. 4th ed. MTAR-Ausbildung. Mit 270 Abbildungen und 58 Tabellen. München: Urban & Fischer, 2003. ISBN: 3437475002. URL: http://www.gbv.de/dms/hbz/toc/ht013630256.pdf.

[4] Krebsinformationsdienst. *Krebsinformationsdienst - Wie entsteht Krebs*. 2023. URL: https://www.krebsinformationsdienst.de/tumorarten/grundlagen/krebsentstehung.php (visited on 04/26/2023).

[5] Deutsches Krebsforschungszentrum. *DKFZ - Was ist Krebs?* 2023. URL: https://www.dkfz.de/de/aktuelles/was-ist-krebs.html (visited on 04/26/2023).

[6] World Health Organization. *The Top 10 Causes of Death*. 2023. URL: https://www.who.int/news-room/fact-sheets/detail/the-top-10-causes-of-death (visited on 06/02/2023).

[7] Binwei Lin et al. "FLASH Radiotherapy: History and Future". In: *Frontiers in Oncology* 11 (2021). ISSN: 2234-943X. DOI: 10.3389/fonc.2021.644400.

[8] Frank Stephan. *New eFLASH Radiation Therapy R&D Options at the Photo Injector Test Facility at DESY in Zeuthen (PITZ)*. 2021. DOI: 10.3204/PUBDB-2021-05225.

[9] Pierrick Regnard et al. "Irradiation of Intracerebral 9L Gliosarcoma by a Single Array of Microplanar X-Ray Beams from a Synchrotron: Balance between Curing and Sparing". In: *Physics in medicine and biology* 53 (Mar. 2008), pp. 861–78. DOI: 10.1088/0031-9155/53/4/003.

[10] Gafchromic. *Gafchromic Dosimetry Media, Type Ebt-Xd*. 2023. URL: http://www.gafchromic.com/documents/EBTXD_Specifications_Final.pdf (visited on 04/24/2023).

[11] Michael Wannenmacher. *Strahlentherapie: mit 298 Tabellen*. Ed. by Michael Wannenmacher, Frederik Wenz, and Jürgen Debus. 2nd ed. Berlin: Springer, 2013. ISBN: 9783540883043.

[12] Hanno Krieger. *Strahlungsmessung und Dosimetrie*. 3rd ed. Springer eBook Collection. Wiesbaden: Springer Spektrum, 2021. ISBN: 9783658333898.

[13] Michael Nasse et al. *The Split Ring Resonator Experiment at FLUTE*. Talk at 8th MT ARD ST3 Meeting 2020. 54.01.01; LK 01. 2020.

[14] Institute for Beam Physics and Technolog. *KARA*. 2023. URL: https://www.ibpt.kit.edu/kara.php (visited on 05/05/2023).

[15] Institute for Beam Physics and Technolog. *FLUTE: Ferninfrarot Linac- und Test-Experiment - Far-infrared linac and test experiment.* 2023. URL: https://www.ibpt.kit.edu/flute.php (visited on 05/05/2023).

[16] Institute for Photon Science and Synchrotron Radiation. *IMAGE Beamline.* 2023. URL: https://www.ips.kit.edu/5926.php (visited on 05/16/2023).

[17] Alfredo Ferrari et al. *FLUKA: A Multi-Particle Transport Code.* 2005. URL: http://www.fluka.org/fluka.php (visited on 04/26/2023).

[18] T.T. Böhlen et al. "The FLUKA Code: Developments and Challenges for High Energy and Medical Applications". In: *Nuclear Data Sheets* 120 (2014), pp. 211–214. ISSN: 0090-3752. DOI: https://doi.org/10.1016/j.nds.2014.07.049.

[19] C. Ahdida et al. "New Capabilities of the FLUKA Multi-Purpose Code". In: *Frontiers in Physics* 9 (2022). ISSN: 2296-424X. DOI: 10.3389/fphy.2021.788253.

[20] Xenia Kempter. "Gelatine-basierte Hydrogele für den 3D Biodruck von Gewebemodellen". Karlsruhe, Karlsruher Instituts für Technologie (KIT), 2021. PhD thesis. 2021.

[21] Paul Allen Tipler. *Physik für Wissenschaftler und Ingenieure.* Ed. by Gene Mosca and Jennifer Wagner. 7th ed. SpringerLink. Berlin, Heidelberg: Springer Spektrum, 2015. ISBN: 9783642541667.

[22] B. Nilsson and A. Brahme. "Interaction of Ionizing Radiation with Matter". In: *Comprehensive Biomedical Physics.* Ed. by Anders Brahme. Oxford: Elsevier, 2014, pp. 1–36. ISBN: 978-0-444-53633-4. DOI: https://doi.org/10.1016/B978-0-444-53632-7.00920-5.

[23] Wolfgang Demtröder. *Experimentalphysik 4 - Kern-, Teilchen- Und Astrophysik.* 5th ed. Berlin: Springer DE, 2017. ISBN: 978-3-662-52884-6.

[24] William R. Leo. *Techniques for Nuclear and Particle Physics Experiments: A How-To Approach.* 2nd ed. Berlin: Springer, 1994. ISBN: 9783540572800.

[25] Ron L. Workman. "Review of Particle Physics". In: *PTEP* 2022 (2022), p. 083C01. DOI: 10.1093/ptep/ptac097.

[26] Glenn F. Knoll. *Radiation Detection and Measurement.* 4th ed. Hoboken, NJ: Wiley, 2010. ISBN: 9780470131480.

[27] M. Budde and F. Bärenfänger. *Medizinphysik Wiki.* 2023. URL: https://medizinphysik.wiki/grundlagen (visited on 04/20/2023).

[28] Jörg Wulff. "Clinical Dosimetry in Photon Radiotherapy – a Monte Carlo Based Investigation". Marburg, Philipps-Universität Marburg, Habil.-Schrift, 2010. PhD thesis. 2010.

[29] Kurt Baier. *Strahlenphysik für die Radioonkologie : 17 Tabellen.* Ed. by Jürger Richter. Stuttgart: Thieme, 1998. ISBN: 3131114819.

[30] Dawid Przystupski et al. "The Cytoprotective Role of Antioxidants in Mammalian Cells under Rapidly Varying Temperature, Pressure and Uv Conditions during Stratospheric Balloon Campaign". In: *bioRxiv* (2019). DOI: 10.1101/526376.

[31] Bundesamt für Strahlenschutz. *Was ist Strahlentherapie?* 2023. URL: https://www.bfs.de/DE/themen/ion/anwendung-medizin/strahlentherapie/einfuehrung/einfuehrung.html (visited on 04/26/2023).

[32] Muhammad Ramish Ashraf et al. "Dosimetry for FLASH Radiotherapy: A Review of Tools and the Role of Radioluminescence and Cherenkov Emission". In: *Frontiers in Physics* 8 (2020). ISSN: 2296-424X. DOI: 10.3389/fphy.2020.00328.

[33] Wenjian Yu. *Monte Carlo Methods for Partial Differential Equations With Applications to Electronic Design Automation*. Ed. by Michael Mascagni. 1st ed. Singapore: Springer Nature Singapore, 2023. ISBN: 9789811932502.

[34] Alex Bielajew. "Fundamentals of the Monte Carlo method for neutral and charged particle transport". In: (Oct. 2001).

[35] Vasilis Vlachoudis. "FLAIR: A Powerful but User Friendly Graphical Interface for Fluka". In: Apr. 2009.

[36] M.A. Zucker M.J. Berger J.S. Coursey and J. Chang. "Stopping-Power & Range Tables for Electrons, Protons, and Helium Ions". In: *NIST Standard Reference Database 124* (2017). URL: https://www.nist.gov/pml/stopping-power-range-tables-electrons-protons-and-helium-ions (visited on 04/30/2023).

[37] John Howard Hubbell and Stephen M. Seltzer. "X-Ray Mass Attenuation Coefficients". In: *NIST Standard Reference Database 126* (2004). URL: https://www.nist.gov/pml/x-ray-mass-attenuation-coefficients (visited on 04/30/2023).

[38] Matthias Nabinger et al. "Efficient Terahertz Generation by Tilted-Pulse-Front Pumping in Lithium Niobate for the Split-Ring Resonator Experiment at FLUTE". In: *PFroc. IPAC'21* (Campinas, SP, Brazil). International Particle Accelerator Conference 12. https://doi.org/10.18429/JACoW-IPAC2021-THPAB251. JACoW Publishing, Geneva, Switzerland, Aug. 2021, THPAB251, pp. 4299–4302. ISBN: 978-3-95450-214-1. DOI: 10.18429/JACoW-IPAC2021-THPAB251.

[39] Matthias Nabinger. "Aufbau der Laseroptik und Charakterisierung lasergenerierter THz-Strahlung für das Split-Ring-Resonator Experiment bei FLUTE". Karlsruhe, Karlsruher Instituts für Technologie (KIT), 2021. MA thesis. 2021.

[40] M. Yan et al. *Optimization of THz radiation pulses at FLUTE*. Poster präsentiert auf 7th International Particle Accelerator Conference (IPAC) : Busan, Korea, May 8-13, 2016. 54.01.01; LK 01. 2016.

[41] Thiemo Schmelzer et al. *Detailed analysis of transverse emittance of the FLUTE electron bunch*. Vortrag gehalten auf DPG-Frühjahrstagung : Physik der Hadronen und Kerne (HK), Plasmaphysik (P), Arbeitskreis Beschleunigerphysik (AKBP) (2022), Online, 28. März–1. April 2022. 54.11.11; LK 01. 2022.

[42] Jens Schäfer. *Internal communication*. 2023.

[43] Beate Bender, Dietmar Göhlich, and Heinrich Dubbel, eds. *Dubbel Taschenbuch für den Maschinenbau :1 Grundlagen und Tabellen*. 26th ed. Springer eBook Collection. Berlin: Springer Vieweg, 2020. ISBN: 9783662597118. URL: https://doi.org/10.1007/978-3-662-59711-8.

[44] MatWeb. *MatWeb*. 2023. URL: https://www.matweb.com (visited on 06/21/2023).

[45] A. Krishnaiah, U. Chakkingal, and H. S. Kim. "Mechanical Properties of Commercially Pure Aluminium Subjected to Repetitive Bending and Straightening Process". In: *Transactions of the Indian Institute of Metals* 61.2 (2008), pp. 165–167. URL: https://doi.org/10.1007/s12666-008-0032-3.

[46] Azo Materials. *Azo Materials*. 2023. URL: https://www.azom.com/properties.aspx?ArticleID=262 (visited on 06/21/2023).

[47] Albert Hofmann. *The Physics of Synchrotron Radiation*. Cambridge Monographs on Particle Physics, Nuclear Physics and Cosmology. Cambridge University Press, 2004. DOI: 10.1017/CBO9780511534973.

[48] Benjamin Kehrer. "Time-Resolved Studies of the Micro-Bunching Instability at KARA". 54.01.01; LK 01. PhD thesis. Karlsruher Institut für Technologie (KIT), 2019. 143 pp. DOI: 10.5445/IR/1000098584.

[49] Ursula Herberger. *Drawing of KIT Campus North Building 348 (KARA hall)*. 2020.

[50] Institute of Microstructure Technology. *LIGA Process*. 2023. URL: https://www.imt.kit.edu/liga.php (visited on 05/16/2023).

[51] Institute of Microstructure Technology. *X-Ray Lithography - XRL Exposure Stations*. 2023. URL: https://www.imt.kit.edu/2330.php (visited on 05/16/2023).

[52] Axel Bernhard. *Vorlesung: Synchrotron- und Undulatorstrahlung*. 2022.

[53] S. Schreiber. "X-Ray Free-Electron Lasers". In: *Comprehensive Biomedical Physics*. Ed. by Anders Brahme. Oxford: Elsevier, 2014, pp. 127–151. ISBN: 978-0-444-53633-4. DOI: https://doi.org/10.1016/B978-0-444-53632-7.00609-2.

[54] Hanno Krieger. "Dosimetrische Materialäquivalenz". In: *Strahlungsmessung und Dosimetrie, ISBN 978-3-658-00385-2. Springer Fachmedien Wiesbaden, 2013, p. 283* (Jan. 2013). DOI: 10.1007/978-3-8348-8128-1_13.

[55] Gafchromic. *Efficient Protocols for Accurate Radiochromic Film Calibration and Dosimetry*. 2023. URL: http://www.gafchromic.com/documents/Efficient%5C%20Protocols%5C%20for%5C%20Calibration%5C%20and%5C%20Dosimetry.pdf (visited on 04/20/2023).

[56] Tobias Göckler et al. "Tuning Superfast Curing Thiol-Norbornene-Functionalized Gelatin Hydrogels for 3D Bioprinting". In: *Advanced Healthcare Materials* 10.14 (2021), p. 2100206.

[57] Merck. 2023. URL: https://www.sigmaaldrich.com/DE/de/technical-documents/technical-article/cell-culture-and-cell-culture-analysis/cell-based-assays/96-well-plate-template (visited on 05/28/2023).

[58] Nicolaas Franken et al. "Clonogenic assay of cells in vitro". In: *Nature Protocols* 1 (2006), pp. 2315–2319. URL: https://doi.org/10.1038/nprot.2006.339.

[59] Deutsches Krebsforschungszentrum. *Flow Cytometry (FACS)*. 2023. URL: https://www.dkfz.de/en/facs/index.html (visited on 06/29/2023).

[60] John R. Taylor. *An Introduction to Error Analysis: The Study of Uncertainties in Physical Measurements*. 2 Sub. University Science Books, 1996. ISBN: 093570275X. URL: http://www.amazon.com/Introduction-Error-Analysis-Uncertainties-Measurements.

[61] Charles R. Harris et al. "Array programming with NumPy". In: *Nature* 585.7825 (Sept. 2020), pp. 357–362. DOI: 10.1038/s41586-020-2649-2.

Danksagung

An dieser Stelle möchte ich mich bei all jenen bedanken, die mich bei und während der Anfertigung dieser Masterarbeit unterstützt haben:

Frau Prof. Dr. Anke-Susanne Müller für die besondere Möglichkeit und Unterstützung diese Arbeit im Bereich der Medizinphysik am IBPT in Kooperation mit dem DKFZ und dem IFG anzufertigen.

Herr Prof. Dr. Joao Seco für die freundliche Übernahme des Zweitgutachtens und der Möglichkeit Erfahrung in der Medizinphysik am DKFZ zu sammeln.

Frau Prof. Dr. Ute Schepers für die freundliche und fachliche Unterstützung im biologischen Teil meiner Arbeit.

Prof. Dr.-Ing. John Jelonnek für den Hinweis auf das Thema dieser Masterarbeit.

Dr. Erik Bründermann, Dr. Markus Schwarz und Dr. Michael Nasse für freundliche Betreuung und thematisch hilfreiche Unterstützung während dieser Arbeit sowie interessante Gespräche. Vielen lieben Dank nochmals an Dr. Markus Schwarz und Dr. Michael Nasse für das Korrekturlesen und die hilfreichen Verbesserungsvorschläge bezüglich meiner Thesis. Vielen Dank an Dr. Alfredo Ferrari für die Unterstützung mit FLUKA und die interessanten Gespräche sowie das Korrekturlesen meiner Arbeit.

Vielen Dank an Christina Stengl und Sonja Leopold für die Betreuung in den mir damals unbekannten Biologielaboren und das geduldige Einarbeiten. Herzlichen Dank nochmals an Christina Stengl für das Korrekturlesen meiner Arbeit.

Danke an Dr. Nigel Smale und Thiemo Schmelzer für die Unterstützung bei FLUTE und dem geduldigen Fragenbeantworten, sowie interessanten und aufbauenden Gesprächen. Vielen Dank auch an Steffen Schott für die Konstruktion des FLUTE Strahlaustrittsfensters sowie der allgemeine Unterstützung seinerseits, Till Borkowski, der mechanischen Werkstatt und der Vakuumgruppe. Ebenso geht mein Dank vielmals an Dr. Angelica Cecilia und Dr. Martin Börner für die sofortige und liebevolle Unterstützung bei den Experimenten an KARA und das Korrekturlesen meiner Arbeit.

Danke an Dr. Wolfgang Mexner und Dr. Julian Genthmann für die Unterstützung mit allerlei IT-Angelegenheiten.

Ebenso danke ich Dr. Stephan-Robert Kötter, Marvin-Dennis Noll und Nicolas Pimenidis vielmals für das Korrekturlesen meiner Arbeit. Dank an Chenran Xu, Christian Goffing und Marvin-Dennis Noll bezüglich der Unterstützung hinsichtlich LaTeX.

Ingesamt geht mein Dank an die freundliche, liebevolle und humorvolle Arbeitsgruppe des IBPT. Danke für die schönen und lustigen Kaffepausen sowie privaten Unternehmungen, unterstützende und aufbauende Gespräche. Besonderen Dank in diesem Sinne an meinen Bürokollegen Jens Schäfer, es war mir eine Ehre. Danke auch für die eindrucksvolle und schöne Zeit zusammen auf der DPG in Dresden und die abwechslungsreichen Laufrunden am Campus Nord und der näheren Umgebung in und um Karlsruhe.

Danke an die Arbeitsgruppe E410 des DKFZ, welche mich direkt freundlich aufgenommen hat, besonderen Dank an Eric Arbes und Jan Thai für die Unterstützung bei Fragen aller Art.

Danke an die Arbeitsgruppe von Prof. Dr. Ute Schepers für die freundliche Aufnahme und Unterstützung sowie die interessanten Gespräche und Einblicke in die Welt der Biologie.

Danke auch an den Kater Spiros für die liebvolle vierwöchige Unterstützung während der Schreibphase und an Jelly und Alex für das Anvertrauen von Spiros und ihrer Wohnung.

Danke an den Hochschulsport für das vielfältige und spannende Sportangebot, danke an alle Menschen, die ich dort kennen lernen durfte!

Danke an alle Tiere, welche sich als Knuddelstressabbaukandidat zur Verfügung gestellt haben.

Danke an alle meine Freunde für die vielen schönen, spannenden und lustigen Momente, für die Unterstützung und Aufmunterung während des gesamten Studiums und besonders für die zahlreiche und liebvolle Unterstützung während schwierigen Abschlussphasen, vielen lieben Dank!

Vielen Dank an meine Familie, meine Eltern und meinen Bruder für die allgemeine bedingungslose Unterstüzung in jeder Art, besonders meiner Mutter für die liebevollen, aufbauenden und geduldigen Gespräche in fordernden Zeiten sowie unseren tierischen Familienmitgliedern, Strolchi, Amor und Rosi, für die liebevolle bedingungslose Unterstützung und aufbauende Zuwendung in jeder Stimmungsphase. Danke für alles!